PhD in Business // No. 87 - 2021

Climate Change and Economic Growth: An Empirical Study of Economic Impacts of Climate Change

Menghan Yuan

NORD UNIVERSITY BUSINESS SCHOOL

NORD
University

www.nord.no

Climate Change and Economic Growth: An Empirical Study of Economic Impacts of Climate Change

Menghan Yuan

PhD in Business
Nord University Business School

PhD in Business no. 87 (2021)

Climate Change and Economic Growth: An Empirical Study of Economic Impacts of Climate Change

Menghan Yuan

ISBN: 978-82-92893-77-7
ISSN: 2464-4331

Print: Trykkeriet NORD

Nord University
N-8049 Bodø
Tel: +47 75 51 72 00
www.nord.no

Acknowledgements

Standing before the finishing line and reflecting on the journey through out my PhD, I am grateful to so many wonderful people that have been extremely helpful and supportive to my PhD study. Undertaking the PhD has been a life-changing experience for me and it would not have been possible to do without the tremendous understanding and encouragement I received from many people in the past few years.

First and foremost, I would like to express my sincerest gratitude to my main supervisor, Thomas Leirvik. He always provides all assistance without reservation and he guides me to see how I could strive for the best of my future. I am deeply grateful for your encouraging supervision as PhD study has been challenging and even at the moments of stagnation and frustration, he never stops being positive and inspiring for me.

Many thanks also to Trude Storelvmo and Martin Wild who have been providing invaluable research insights from their expertise of climate science. Given that I am working on an interdisciplinary field of climate and economy, it is of critical importance to have contribution from researchers of various backgrounds. They provided extremely practical contributions to my research.

I greatly appreciate the support received from my co-supervisor Prof. Peter C.B. Phillips, who is really influential in shaping my empirical research methods and critiquing my results. I also thank him for inviting me to visit Yale University, as well as Prof Tony Smith who hosted me during the research stay. The experience provided me precious opportunities to enhance my research competence through Econometrics training and to develop research ideas that were conducted later during the course of PhD.

I am also very grateful to all those at Nord University Business School, especially Ellen Abelgård and Grete Knudsen. Not only has Ellen been so helpful with resolving all kinds of difficulties at work, she is also an attentive friend who makes efforts in helping me to better integrate into the local community and making me feel welcome in Norway. Special thanks to Grete for your a great amount of assistance throughout my research project.

My deep appreciation goes out to the local PhD students and faculty: Pamela Ogada, Yevheniia Antoniuk, Samuel Sarkodie, Kseniya Pak, Valeria Nyu, Vu Le Tran, Anastasiya Henk, Silje Aakre, and Beate Vading. Many thanks for their dedication in discussing research ideas with me and their friendship and warmth they extended to me.

And finally I would like to say a heartfelt thank you to my parents for always believing in me and encouraging me to follow my dreams. And to my dearest friend, Linqi Wang, for convincing me to pursue a doctoral degree. Without her, I could not have embarked this marvelous journey in the first place. And many thanks to Linqi Wang, Haomin Wang, and Xiaodi Guo for being such reliable allies whenever I need them, making it possible for me to finish what I started.

Bodø, May 2021
Menghan Yuan

Abstract

Researchers have made significant advancements in answering whether and how climatic conditions influence societies and the performance of economies for decades. However, large uncertainties exist that prevent us from providing consistent climate projections for a given future emission scenario, which has obvious consequences for society's ability to take necessary mitigation and adaptation action. Climate sensitivity, which measures how much global temperature will change after a doubling of greenhouse gases compared to preindustrial times, has been widely used in climate-economic models that translate climate change into economic damages, and therefore is of highly concern to policy makers to inform climate policies. The goal of this thesis is to constrain the uncertainty of climate sensitivity and to investigate the economic impacts of climate change.

This thesis consists of four papers. The first two papers aim to address the uncertainty of climate sensitivity. In our empirical estimation framework, we relate temperature to solar radiation and CO_2 in a cointegrating equilibrium relationship. However, there is no readily available solar radiation dataset that currently provides observations with global coverage. The first paper resolves the dataset problem by implementing a spatial interpolation method to an observation-based solar radiation dataset. Using a wide range of explanatory variables, we apply a machine learning method, Random Forest, to predict solar radiation at unsampled locations. The output from this paper is a global dataset with complete global land surface coverage during the period 1961-2019, which provides the input data for the climate sensitivity estimation conducted in the second paper.

The second paper empirically estimates Transient Climate Sensitivity (TCS) for 22 global climate models and significantly narrows the confidence interval of TCS compared to previous estimates. Using the constrained distribution of TCS, we further examine its implications to the social cost of carbon. In alignment with the warming target of $1.5°C$ under the Paris agreement goals, the revised TCS leads to a remaining carbon budget of around nine years of current CO_2 emissions. Compared to the unconstrained reported TCS values in the Coupled Model Intercomparison Project (CMIP6), our narrowed TCR confidence interval suggests a median reduction in the remaining carbon budget of approximately one year of allowable CO_2 emission.

The third and fourth paper use panel data analyses to examine how agriculture and aggregated economies are influenced by climate change. The third paper investigates regional heterogeneity in the effects of climate change on soybean yields. We find statistically significant difference in yield sensitivities to climate change among various regions. A global homogeneous model suggests predominantly negative effects of a warmer climate; however, a regional model of Southeast Asia indicates that local soybean yields could be enhanced in countries located on the northern, cooler fringes of this region. Moreover, we find soybean yields in developed countries, such as the US, Canada, Australia, and European countries, tend not to be significantly affected by climate change.

Following the empirical framework from the third paper, the fourth paper further examines realized impacts of historical climate change on aggregate economic outputs. We find that European and Central Asian countries have benefited both from temperature rising and precipitation fluctuations; on the other hand, a double whammy has been observed in Africa, the trends toward a warmer and dryer climate have both impeded local economic growth.

Contents

CHAPTER 1

Introduction

1.1 Theoretical Background

Climate Trends

A growing body of evidence indicates that Earth's climate is changing in general, and the temperature in particular. Weather patterns are changing, disrupting national economies and affecting lives. The global surface temperature has been progressively increased. During the past century (1900-2000), the global average temperature has increased by $0.74°C$; moreover, more than a half of the warming was observed in the last two decades of the period (a rise of $0.38°C$ happened in 1980-2000) (Scafetta and West, 2005). According to Duan et al. (2021), the warming rate in the second half of the 20th century is approximately twice as large as in the whole century. The Fifth Assessment Report (IPCC AR5) reported that 2010-2019 was the warmest decade ever recorded and the period of 1983-2012 was the warmest 30-year span over the last 800 years for the Northern Hemisphere.

Hydrological responses to global warming are complicated and vary spatially. It has been reported that global precipitation over land has increased by $\sim$3% over the last century (Gerten et al., 2008), which could indicate less drought on a global scale. However, regional precipitation trends vary considerably—dry areas tend to get dryer and wet areas tend to get wetter. This in fact indicates that areas that experienced droughts in the past, will most likely experience them more often in the future, and areas that rarely experienced droughts in the past will be increasingly less likely to experience droughts in the future. Drying trends are observed over most of Africa, southeast Asia, eastern Australia and southern Europe, and increased precipitation was found over the central US, Argentina and northern high-latitude areas during 1950-2010 (Dai, 2013). Summer drying has been reported in many parts of the northern subtropics and midlatitudes (Burke and Brown, 2008). Moreover, additional areas of land surface are predicted to be in drought by the end of the century (Burke et al., 2006). Rind et al. (1990) and Jones et al. (1996) projected that, severe drought conditions will increase dramatically, especially at low to midlatitudes, by the middle of the twenty-first century.

Solar radiation is a fundamental determinant of the Global Energy Balance, and a crucial driving force for temperature change and hydrological cycle variation (Budyko, 1969; Obryk et al., 2018). Solar radiation has been a key input for many climate studies that investigate climate sensitivity, its effect on agriculture and other economic sectors. Storelvmo et al. (2016) decomposed observed temperature development into components attributable to changes in greenhouse gas concentrations (CO_2) and surface radiation. The increase in greenhouse gas pulls the temperature up, while the reduction of downward solar radiation drags the temperature down. What we observe is the net effect—the temperature. Phillips et al. (2020) estimated transient climate sensitivity, which is the change in global mean surface temperature for a doubling of CO_2, using an econometric model that applies surface radiation as one of the inputs. Solar radiation is also of high importance for agricultural management that will need to control the amount of solar radiation in order to stimulate crop growth as well as other applications that deploy solar power energy (Lewis, 2016).

Despite of the importance of solar radiation, there are few available global datasets that provide reliable and representative data describing its evolution. Taking an unbalanced panel dataset of solar radiation, the first paper in this thesis constructs a global solar radiation dataset using a machine learning method, and based on which, global solar radiation trends are summarized. Using the constructed solar radiation dataset, the second paper estimates climate sensitivity, defined as the global average temperature change due to a doubling of atmospheric CO_2. Our empirical framework relates temperature to solar radiation and CO_2 in a cointegrating equilibrium relationship. Therefore the constructed dataset in the first paper provides the prerequisite input for the second paper.

Climate change has wide-ranging impacts on the world's economies, including human health, energy use, global food security, etc. I will review here some of the major findings of the social and economic impacts of climate.

Economic Impacts: Agricultural Yields

Agriculture is one of the most directly exposed sectors to the impacts of climate change. Variations in climate processes such as temperature, precipitation, and solar radiation directly affect crop growth and production significantly through photosynthesis, transpiration, respiration, and so on. In particular, variabilities in temperature and precipitation can explain a quarter of the crop yield's variability in non-irrigated plants (Kukal and Irmak, 2018). The importance of temperature, often dominating rainfall, in the production of staple crops (Schlenker et al., 2005; Lobell and Burke, 2008). Crops are sensitive to temperatures during specific stages of the growing cycle. The relationship between crop yields and growing season temperature and precipitation changes is extensively studied. Some regional studies indicate that yield responses differ largely from regions to regions, both in magnitude and signs of the impacts. For example, Indian rice yields have been reduced by 5.7% during 1966-2002 under historical trends in temperature, monsoon characteristics, and rainfall (Auffhammer et al., 2012). In the case of Sub-Saharan Africa, substantial losses for aggregate production are predicted—a reduction of -22 and -17% are estimated for maize and sorghum by 2050, respectively (Schlenker and Lobell, 2010). On the other hand, Kucharik and Serbin (2008) found that a trend towards warmer and drier conditions could support higher corn and soybean yields in northern Corn Belt locations that have a cooler climate in general.

In spite of the reported regional difference in crop yields responses to climate change, few studies have explicitly considered parameter heterogeneity in empirical models. Current studies primarily assume homogeneous sensitivities for all regions, and the difference in realized responses is because of the different initial temperatures for various regions (see e.g., Dell et al., 2012; Burke et al., 2015; Diffenbaugh and Burke, 2019). In the third paper of this thesis, by including regional dummies in our global empirical framework, we explicitly explore the regional heterogeneity in crop yield responses to changes in temperature and precipitation, and thereby obtain region-specific response functions for six regions comprising the world.

Economic Impacts: Aggregate Production

Rather than focusing on individual or sectoral responses to climate, an alternative "top-down" approach examines how the macro-economy as a whole responses to climate change. Studies in this category use gross domestic product per capita (GDPPC) as the variable of interest. Recent studies have shown that temperatures have a nonlinear effect on economic production, such that output is maximized at 13°C (see Figure 1.1, Burke et al., 2015). In other words, the parabolic relationship between temperature and economic growth indicates that countries with an annual average above 13°C will see a reduction in GDPPC with increased warming, whereas countries with an annual average below 13°C, such as Brazil and India, will experience an increase in economic production. For countries with an annual average below the optimum, for example, Germany and France, the economic output will increase until the optimum is reached.

There is of course a lot of heterogeneity between countries that have a hot annual average temperature, but many of those countries are located in Africa, close to the equator. These countries are already hot and poor, and many of them have a poorly developed infrastructure to mitigate even harsher climatic conditions. Australia, on the other hand, has also above the global optimum temperature, but with a very high GDPPC, highly developed infrastructure, and yet experiences a warming trend in temperature (Bureau of Meteorology, 2020). The implication is that there is plenty of heterogeneity in how countries with an annual average temperature above the global optimum are able to handle a further increase in temperature. Moreover, Diffenbaugh and Burke (2019) found that global warming has increased global economic inequality. Given that hot countries tend to be poor, with national income falling 8.5% per degree °C in the world cross section (Dell et al., 2009), it is very likely that poor countries are worse-off while rich countries are better-off under continued global warming. In particular, Diffenbaugh and Burke (2019) indicated that the ratio of GDP per capita between the top and bottom decile countries are 25% larger than in a world without global warming.

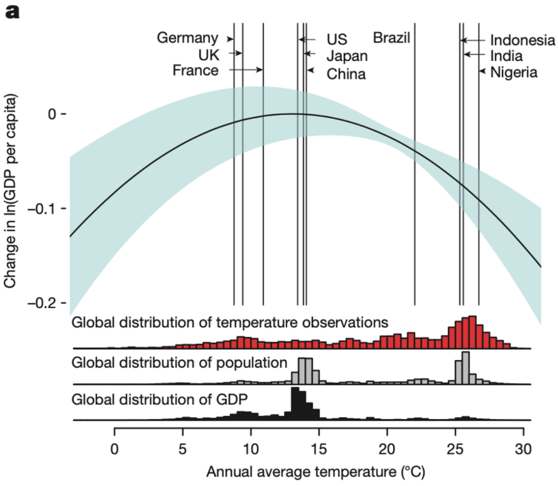

Fig. 1.1 Effects of annual average temperature on economic production. The figure is taken from Burke et al. (2015). Vertical lines indicate average temperature for selected countries. Histograms show global distribution of temperature exposure (red), population (grey), and income (black).

The scientific interest in the effects of rainfall on economic growth has grown significantly, however, only a limited number of studies deliver conclusive results. Berlemann and Wenzel (2018) found statistically significant negative impacts of rainfall shortages on economic growth, but the effects are only specific to developing countries where economies are largely dependent on rainfed agriculture. This indicates that the effects of precipitation on an economy are mainly realized through agriculture. Berlemann and Wenzel (2018) also reported that rainfall surpluses have no significant growth effects. Schlenker and Lobell (2010) further corroborated the effects of low precipitation by indicating that low precipitation has slowed GDP growth in Africa.

In the fourth paper, we examine realized impacts of observed temperature and precipitation evolution for countries worldwide. Our results show dominant effects of temperature as compared to precipitation, moreover, regions have responded considerably differently. Specifically, Europe and Central Asia have benefited from both historical temperature and precipitation trends, whereas a double whammy has been observed in Africa, resulting in economic growth being slowed down by both factors.

Health Impacts

Climate change is also found to have severe implications for human health, and even though I do not directly address this in my thesis, health and economic productivity is closely related (see e.g., Ivinson, 2002; Bhargava et al., 2001). Good health has a positive and statistically significant effect on aggregate output (Bloom et al., 2004). Healthier workers are physically and mentally more energetic and productive at work places, thereby boosting economic growth and development.

As individuals, each of us is constantly exposed to temperature, and our health could be compromised under extreme heat or cold, which could lead to severe cardiovascular, respirator, and cerebrovascular effects that can result in death (Deschenes, 2014a,b; Carleton and Hsiang, 2016). For example, in Delhi, deaths increase by 3.2% per $^{\circ}C$ above $20^{\circ}C$, and in the US, days above $32.2^{\circ}C$ and below $-6.7^{\circ}C$ increases male mortality rate by 2% and 1.4%, respectively (Barreca et al., 2016). In addition to these mortality damages, many injuries from temperature extremes are not lethal. During high and low daily temperatures, hospital admissions increase for respiratory and cardiovascular diseases. In particular, besides temperature, humidity was found to be an critical determinant of human influenza, which is a notable cause of hospitalization in temperate climates (Barreca and Shimshack, 2012).

Transmission and distribution of vector-borne disease are greatly influenced by environmental and climatic factors (see e.g., Gething et al., 2011; Craig et al., 1999). Accordingly, it has been suggested that the dynamics and distribution of a range of vector-borne diseases, including malaria, dengue fever, viral encephalitis, schistosomiasis, Lyme disease, could be impacted by climate change (see e.g., Paaijmans et al., 2012). Temperature regimes constrain the geographical extent of the disease and contribute to determining its intensity. Generally, transmission intensity is assumed to be higher under warmer conditions, where parasites and pathogens within vectors increase fast. For example, transmission intensity of malaria are largely influenced by mosquito and parasite life history traits (e.g., adult mosquito longevity, biting rate), which are strongly temperature sensitive (Carballar-Lejarazú et al., 2020; Scudellari, 2019). Shapiro et al. (2017) suggested a temperature optimum for transmission of 29°C, with minimum and maximum temperatures of 12 and 38°C, respectively. Anthropogenic climate change is likely to shift disease ranges and increase exposure globally, more research is need to quantify the link between changing temperatures, rainfall, and public health (Bhatt et al., 2013; Gething et al., 2010).

Temperature extremes also impact performance of workers, especially for factory or labor intensive manual work. Optimal temperature for worker performance is between 21 to 25°C, while beyond that range, too hot or too cold temperatures are harmful for productivity (Seppanen et al., 2003). When the temperature is above 25°C, Seppanen et al. indicated an average 2% decrement in work performance with an temperature increase of 1°C.

1.2 Fundamental Approaches and Data Availability

In this section, I will present some fundamental tools for economic analyses of climate change. These models constitute the prototypes of models applied in my thesis. I will first talk about *Spatial interpolation*, which is applied in the first paper to tackle the missing data problem in climatic datasets. Measuring climate change is an essential component of climate economic studies and is constantly discussed through out the thesis; therefore, I will then talk about *trend analysis* techniques frequently applied in climate science.

Panel data analysis is one of the most frequently used approaches in empirical studies of climate change. Paper 2 to 4 all applied panel approaches either to obtain estimates of critical parameters in climate models or to make inference of economic damages from climate change. Therefore, some elementary issues of panel data analysis are discussed briefly.

At last, I will introduce data availability related in the thesis, including weather datasets, climate model directories, and databases of economic indicators.

1.2.1 Spatial Interpolation

To study the trends and impacts of climate, it is of the utmost importance to have reliable data, which can be used for analyzing a wide range of global, and local, aspects of the environment. Global air temperature has become the primary metric for measuring global climate change. The overall increase of global temperature over the last century has been largely attributed to the increase of greehouse gases (Flato and Marotzke, 2013). Besides the effects of greenhouse gases, solar radiation has been a major driver of temperature variability (Wang and Dickinson, 2013). Storelvmo et al. (2016) show that observed temperature trends can be decomposed into components attributable to changes in greenhouse gas concentrations and surface radiation. The effects of solar radiation impacts on temperature are primarily explained through changes in atmospheric aerosol loading, such as SO_2, which has a cooling effect. In particular, Storelvmo et al. (2016) find that the solar radiation trends have caused a cooling that masked approximately one-third of global warming over the past half-century.

In order to measure global temperature dynamics and climate change, it is essential to have datasets that have complete spatial coverage and have climatic observations for a relative long term. Such datasets are readily available for temperature and CO_2, however, there are few, if any, complete datasets for solar radiation over a long time period for many locations. One such dataset is the Global Energy Balance Archive (GEBA, Wild et al., 2017). The GEBA dataset has a long time range, with the first observations from the early 1950's, continuing to the present day. However, many values are missing due to maintenance and operational failures of observation devices. Therefore, paper 1 addresses the missing value problem in the GEBA dataset, aiming to construct a solar radiation dataset with complete spatial coverage and containing data for a long period.

To fill missing values, many different techniques have been tested, with linear interpolation as one of the simplest. This, however, does not perform very well if there are several consecutive missing values, and in particular if the data is seasonal, which is certainly true for solar radiation. Other, more advanced, techniques used by researchers are, for example, Inverse Distance Weighting

(IDW), Kriging, splining, regression and etc. (see e.g., Collins, 1995; Scudiero et al., 2016; Erxleben et al., 2002). We applied advanced statistical methods, often called machine learning techniques, to fill any missing values in the solar radiation dataset.

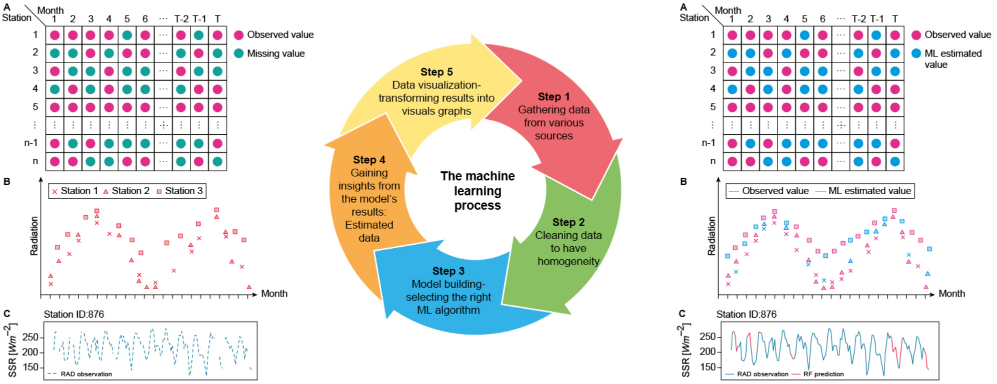

Fig. 1.2 A graphical illustration of the original and the output data, and how the machine learning method is implemented to implement the spatial interpolation. Figure is taken from Leirvik and Yuan (2021).

Figure 1.2 shows a diagram of how we implemented spatial interpolation in paper 1. Panel A in the left column of Figure 1.2 illustrates our initial dataset, where the y-axis is the station and the x-axis is time. Thus, each geographical station measures solar radiation at time t. An observation is illustrated with a red colored circle. However, some observations are missing, and are represented by the green colored circles. Our objective is to apply various quantitative methods to the values illustrated by the green circles. Estimates from machine learning techniques are represented by the blue circles in Panel A, in the right column of Figure 1.2. Panels B in the left and right column illustrate three hypothetical stations with solar radiation values, points in time where the solar radiation is missing (left column), and how the solar radiation time series would be after inserting the estimates of solar radiation (right column) for any missing values. Furthermore, Panel C in the left column takes a randomly selected station with actual observations and missing values, and plots the solar radiation of the time-period analyzed. Panel C in the right column illustrates a complete solar radiation time series with both estimated and observed values of the solar radiation. The middle column in Figure 1.2 illustrates the machine learning process applied in the paper and how it is used to achieve the results.

Frequently applied spatial interpolation methods are briefly explained at what follows. IDW is a deterministic estimation method where the value at a missing location is determined by weighted average of values at neighboring points, where the weights are assigned as inversely proportional to the distance from the target location. Although its simplicity makes it easy to implement, a drawback is that it will have a discontinuous slope of the estimation surface at each data point (Collins, 1995). The Kriging method is a method of interpolation where the interpolated values are modeled by a more sophisticated relationship between observed values with target missing values. The relationship is depicted by a variogram function, which calculates the semi-variance differences (spatial autocorrelation) between the neighboring values. The variogram can be exponential, spherical, logarithmic or any other functions. Spline models, a class of functions often called polynomial interpolation models, use mathematical functions to connect the sampled data points in order to produce a continuous elevation and grade surface while minimizing the curvature of the surface. These models are useful when the surface varies smoothly without sharp fluctuations. The models mentioned above are univariate, which means that they apply only information about the variable of interest, i.e., the variable with missing values that is desirable to estimate. Regression methods break the limit of using only the target variable for estimating missing values by characterizing the response's relationship with other potential explanatory variables, such as location (latitude, longitude) of measurement station, and other correlated atmospheric variables. Recently, so-called machine learning methods have been applied in spatial interpolation (see e.g., Jiang, 2008; Sun et al., 2016; Zhou et al., 2017). Machine learning consists of many different statistical models that computer systems use to effectively perform a specific task without using explicit instructions and strong assumptions, it relies mostly on pattern recognition and inference instead. One such method, the Artificial Neural Network (ANN), was implemented for the estimation of monthly mean solar radiation and showed superiority over polynomial fitting models (Jiang, 2008). Though with its high accuracy, the ANN method has the limitation of computational complexity and therefore cannot incorporate a large number of explanatory variables. Another alternative machine learning model, the Random Forest (RF) model, provides a solution for accommodating a high dimension of covariates, and has been applied in several recent studies. For example, Sun et al. (2016) presented a RF model to estimate solar radiation based on three types of input variables: sunshine hours, air temperature, and their derivative types. Surface albedo, emissivity and vegetation indices data were used as predictors by Zhou et al. (2017) in the RF model in order to generate an accurate prediction of solar radiation. Most of the research on spatial interpolation is on a regional scale and/or only considers a relatively short period of time for testing model quality, such as a one-year period. The main contribution of this paper is to propose an effective machine learning method in spatial interpolation of Surface Solar Radiation (solar radiation), that is applicable for the global scale and could make use of information from long term trends.

The first objective is to interpolate the solar radiation dataset in GEBA, therefore obtaining a complete dataset of solar radiation with no missing values. Two papers are constructed in this endeavour. Given a variety of interpolation methods available, my supervisor and I started with a performance evaluation of interpolation approaches, which developed into a published paper in *Earth and Space Science* (Leirvik and Yuan, 2021). This paper applies Random Forest (RF) and seven other conventional spatial interpolation models (Ordinary Kriging, Linear Regression, several types of Regression Kriging) to the GEBA dataset. Based on the trained models, we calculated error metrics of predicted values against observations and found that the RF model significantly outperforms all other models. In particular, we find that the mean absolute error (MAE) of the RF is reduced by 50+% compared to the average MAE of the conventional interpolation methods. This paper is not included in my PhD thesis because it is not applied directly in my climate-economic research.

Given that Leirvik and Yuan (2021) demonstrated the superiority of the Random Forest model, we then applied the model to unsampled areas or time points with no existing observations. In other words, we generated simulations that extend the original dataset both over space and time. The simulation output is a gridded dataset at 0.5° resolution that covers all land surface except

Antarctica and spans the period from 1961 to 2019. Its spatial completeness and the large time span make the constructed dataset a valuable alternative to existing solar radiation datasets. Based on the new dataset, we further analyzed historical solar radiation trends in a regional and global level. The results form this analysis is important and very useful in many areas regarding the climate-human-economic relationship, the results was condensed into a collaborative paper with Thomas Leirvik and Martin Wild, which is revise-resubmit in *Journal of Climate*. I decide not to include Leirvik and Yuan (2021) in this thesis because I deem it as a trial project for preparing the model selection criteria for selecting a spatial interpolation method that is most appropriate for the dataset construction conducted in the first paper of the thesis. The output dataset of the first paper is further applied in the second paper of the thesis for climate sensitivity estimation.

1.2.2 Trend Analysis

Linear Trend Estimation

Climate data is often a univariate time series, $\{y_t\}_{t=1}^{T}$, that is a sequence of random variables indexed by t. It is critical to understand the rates of change for climate variables, such as temperature, precipitation, and solar radiation. A commonly reported metric is the decadal trend, which measures the average change per decade. We use decadal trends to quantify the average evolution of climate during a long term, and they can be used to inform, for example, whether global warming is accelerating, decelerating, or no change; if there is a persistent trend in rainfall. Trend analysis is applied throughout the thesis, and the results are explicitly reported in the first two papers.

The various studies analyzing long-term trends of surface solar radiation suggests a widespread decrease in surface solar radiation between the 1950s and 1980s ("global dimming"), with a partial recovery more recently at many locations ("brightening") (see e.g., Wild, 2009; Sanchez-Lorenzo et al., 2015; Stjern et al., 2009). Several of these studies discuss the brightening in Europe in more detail. Norris and Wild (2007) determined a Pan European time series based on 75 stations from GEBA, and estimated a linear decline of 3.1 Wm^{-2}

decade^{-1} for the "dimming" period 1971-1986, but an increase of 1.4 Wm^{-2} decade^{-1} for the "brightening" period 1987–2002. Chiacchio and Wild (2010) pointed out that the brightening in Europe is particularly pronounced in the spring and summer seasons, while there is no evidence for a brightening in the other seasons. Paper 1 contributes to the existing literature by reporting decadal trends of solar radiation for each $0.5° \times 0.5°$ grid cell on the global land surface to inform the global brightening/dimming process.

Trend analysis is also applied in other papers in the thesis. In particular, the second paper calculates the warming trends of global surface temperature using data from climate model output, which are later used as input parameters for climate sensitivity estimation. The third and fourth paper are focused on examining agricultural and economic impacts of climate change, respectively. Climate trends of temperature and precipitation are summarized on a country scale (crop growing season average trends in the third paper and annual average trends in the fourth paper) and realized impacts of historical trends are reported in the fourth paper.

A linear trend of y_t is the estimate of the slope coefficient of a linear regression of y_t on time. The decadal trend can be obtained by multiplying the slope coefficient by 10. Figure 1.3 shows an example of linear trend estimation.

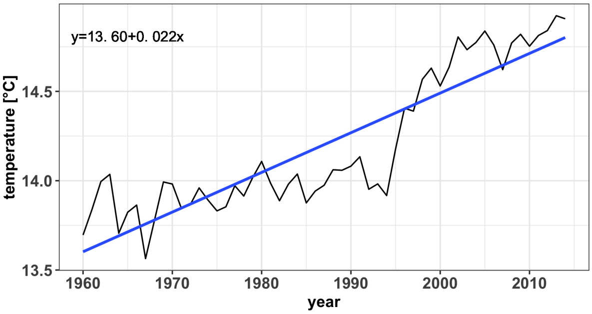

Fig. 1.3 Trend estimation illustration. Black line stands for temperature observations, blue line stands for linear trend approximation. The estimation of the regression equation is shown on the top-left corner of the figure, with the intercept coefficient (β_0) being 13.6 and the linear trend coefficient (β_1) being 0.022. Note that the x-axis (year) is rescaled to start from 0 in the equation estimation.

A linear trend regression model is given by

$$y_t = \beta_0 + \beta_1 T_t + \varepsilon_t \tag{1.1}$$

where $t = 1, \ldots, T$, and T_t is the time variable assigned to y_t. β_0 is the intercept and β_1 is the slope coefficient which can be interpreted as the linear trend of y_t.

Eqn. (1.1) can be written in a matrix form

$$\boldsymbol{y} = \boldsymbol{X}\boldsymbol{\beta} + \boldsymbol{\varepsilon} \tag{1.2}$$

where $\boldsymbol{y}$ is a $T \times 1$ vector, and $\boldsymbol{\beta} = (\beta_0, \beta_1)'$, and $\boldsymbol{X}$ is a $T \times 2$ matrix, with the first column being 1 indicating the intercept constant.

The ordinary least-squares (OLS) estimation minimizes the sum of squared errors (SSE):

$$Minimize_{\boldsymbol{\beta}} SSE(\boldsymbol{\beta}) = \boldsymbol{\varepsilon}'\boldsymbol{\varepsilon} = (\boldsymbol{y} - \boldsymbol{X}\boldsymbol{\beta})'(\boldsymbol{y} - \boldsymbol{X}\boldsymbol{\beta})$$

Expanding this gives

$$\boldsymbol{\varepsilon}'\boldsymbol{\varepsilon} = \boldsymbol{y}'\boldsymbol{y} - 2\boldsymbol{y}'\boldsymbol{X}\boldsymbol{\beta} + \boldsymbol{\beta}'\boldsymbol{X}'\boldsymbol{X}\boldsymbol{\beta}$$

The necessary condition for a minimum is

$$\frac{\partial S(\boldsymbol{\beta})}{\partial \boldsymbol{\beta}} = -2\boldsymbol{X}'\boldsymbol{y} + 2\boldsymbol{X}'\boldsymbol{X}\boldsymbol{\beta} = 0$$

Then the explicit solution is

$$\begin{aligned} \boldsymbol{\beta} &= (\boldsymbol{X}'\boldsymbol{X})^{-1}\boldsymbol{X}'\boldsymbol{y} \\ &= (\mathbb{E}(\boldsymbol{X}'\boldsymbol{X}))^{-1}\,\mathbb{E}(\boldsymbol{X}'\boldsymbol{y}) \end{aligned} \tag{1.3}$$

The OLS moment estimator is therefore given by

$$\begin{aligned} \widehat{\boldsymbol{\beta}} &= \left(\frac{1}{T}\sum_{t=1}^{T} \boldsymbol{x}_t\boldsymbol{x}_t'\right)^{-1} \left(\frac{1}{T}\sum_{t=1}^{T} \boldsymbol{x}_t y_t\right) \\ &= \left(\sum_{t=1}^{T} \boldsymbol{x}_t\boldsymbol{x}_t'\right)^{-1} \left(\sum_{t=1}^{T} \boldsymbol{x}_t y_t\right) \end{aligned} \tag{1.4}$$

1.2.3 Panel Data Analysis

Economists traditionally use the term **Panel data**, also called **longitudinal data**, to refer to data structures consisting of observations on many individuals for multiple time periods. The observed "individuals" can be, for example, people, households, workers, firms, schools, production plants, industries, regions, states, or countries. The distinguishing feature relative to cross-sectional datasets is the presence of multiple observations for each individual. More broadly, panel data methods can be applied to any context with cluster-type dependence (Hansen, 2019).

Paper 2 uses a panel data structure with stations being individuals, where parameters can be estimated by fully-modified least squares estimators (FM-OLS, refer to paper 3 for details). Paper 3 and 4 apply a panel data structure with countries being individuals. Here I introduce the individual fixed effects model, which consists of the baseline of the empirical frameworks applied in paper 3 and 4. We consider the linear individual effects model given by

$$y_{it} = \boldsymbol{x}'_{it}\boldsymbol{\beta} + u_i + \varepsilon_i \tag{1.5}$$

or in a matrix form

$$\boldsymbol{y}_i = \boldsymbol{X}'_i\boldsymbol{\beta} + \mathbf{1}_i u_i + \boldsymbol{\varepsilon}_i \tag{1.6}$$

where y_{it} is indexed by an individual i and time t, $i = 1, \dots, N$ and $t = 1, \dots, T$, u_i is the individual-specific effect that represents a time-invariant unobserved missing variable. For example, if $\boldsymbol{y}_i$ represents economic outputs of country i, $\boldsymbol{X}_i$ represents climate variables, then the individual-specific effects, u_i, will absorb effects of omitted factors that influence the country's historical average economic development, such as history, culture, topography, demography, institutional qualities, etc.

When u_i is interpreted as a missing variable it is natural to expect it to be correlated with the regressors $\boldsymbol{x}_{it}$. Correlation between u_i and $\boldsymbol{x}_{it}$ will cause both pooled and random effect estimators to be biased due to the classic problems of omitted variables bias and endogeneity. If we leave the relationship between u_i and $\boldsymbol{x}_{it}$ fully unstructured, then the only way to consistently estimate the coefficient $\boldsymbol{\beta}$ is by an estimator which is invariant to u_i. This can be achieved by transformations which eliminate u_i.

On such transformation is the within transformation. I will present here this transformation in detail.

Define the mean of a variable for a given individual as

$$\bar{y}_i = \frac{1}{T_i} \sum_{t \in S_i} y_{it}$$

We call this the individual-specific mean. Subtracting the individual-specific mean from the variable we obtain the deviations

$$\dot{y}_{it} = y_{it} - \bar{y}_i$$

Similarly for the regressors we define the individual-specific means and the demeaned values

$$\bar{\boldsymbol{x}}_i = \frac{1}{T_i} \sum_{t \in S_i} \boldsymbol{x}_{it}$$
$$\dot{\boldsymbol{x}}_{it} = \boldsymbol{x}_{it} - \bar{\boldsymbol{x}}_i$$

Taking individual-specific averages to Eqn. (1.6) we obtain

$$\bar{y}_i = \bar{\boldsymbol{x}}_i' \boldsymbol{\beta} + u_i + \bar{\varepsilon}_i$$

where $\bar{\varepsilon}_i = \frac{1}{T_i} \sum_{t \in S_i} \epsilon_{it}$. Subtracting from Eqn. (1.6) we obtain

$$\dot{y}_{it} = \dot{\boldsymbol{x}}_{it}' \boldsymbol{\beta} + \dot{\varepsilon}_{it} \tag{1.7}$$

where $\dot{\varepsilon}_i t = \epsilon_{it} - \bar{\varepsilon}_i$. By doing so, the individual effect u_i has been eliminated. It can be written in matrix notation

$$\dot{\boldsymbol{y}}_{it} = \dot{\boldsymbol{X}}_{it}' \boldsymbol{\beta} + \dot{\boldsymbol{\varepsilon}}_{it} \tag{1.8}$$

The OLS estimator to Eqn. (1.8) is

$$\begin{aligned} \bar{\boldsymbol{\beta}}_{\textbf{fe}} &= \left(\sum_{i=1}^{N} \sum_{t \in S_i} \dot{\boldsymbol{x}}_{it} \dot{\boldsymbol{x}}_{it}' \right)^{-1} \left(\sum_{i=1}^{N} \sum_{t \in S_i} \dot{\boldsymbol{x}}_{it} \dot{y}_{it} \right) && (1.9) \\ &= \left(\sum_{i=1}^{N} \dot{\boldsymbol{X}}_i' \dot{\boldsymbol{X}}_i \right)^{-1} \left(\sum_{i=1}^{N} \dot{\boldsymbol{X}}_i' \dot{\boldsymbol{y}}_i \right) && (1.10) \end{aligned}$$

This is known as the **within** estimator of $\boldsymbol{\beta}$. It is called the within estimator because it is based on the variation of the data within each individual.

1.2.4 Data Availability

Climate Data

Climate scientists have been using climate/weather data to examine long-term trends of climate evaluation and occurrences of extreme weather events (see e.g., Jones et al., 1996; Burke et al., 2006; Auffhammer et al., 2013; Carleton and Hsiang, 2016). To clarify the difference between climate and weather, climate is a long average of weather at a given location, while weather refers to short term atmospheric conditions. Climate change refers primarily to long-term changes.

There are several main sources of climate data: observations from weather stations, observation-derived products (e.g., satellite data), and climate model simulations. Observations collected from weather stations are regarded as the most reliable, however, they are afflicted with problems about spatial and temporal coverage. This is because it is difficult to main observation stations at mountainous and marine regions; moreover, maintenance and operational failures cause interruptions and discontinuity of observations. Missing value problem is especially typical in solar radiation datasets, because there is no extensive coverage of such observation stations, and existing stations tend to cluster in developed regions, such as Western Europe and North America. However observations for a range of other variables are complete, such as temperature, precipitation, cloud coverage, due to their widespread coverage of weather stations and their well-developed interpolation techniques. Given the disparity in data availability between solar radiation and other climate factors, paper 1 explores the possibility to predict solar radiation using other climate factors as explanatory variables. And it turns out that our selected climate variables can explain more than 90% of the total variation of global solar radiation.

In paper 1, we obtain data of climatic predictors from the Climate Research Unit Time-series data version 4.04 (CRU-TS v.4.04, Harris et al., 2020). The CRU dataset provides high resolution ($0.5^\circ \times 0.5^\circ$) gridded data of monthly observations for a wide range of meteorological variables over the period 1901-2019. It is derived by the interpolation of monthly climate anomalies from extensive networks of weather station observations. It covers all land domains of the world except Antarctica, and there are no missing values in the defined domain. CRU dataset is applied in all four papers contained in the thesis. Paper 2 uses the temperature data to estimate climate sensitivity; paper 3 and 4 aggregate gridded temperature and precipitaion data to country-level data and, based on which, estimate economic impacts of climate change.

Global Climate Models (GCMs) provide simulations of historical climate and predictions of climate. GCMs are physics-based models are based on well-documented physical processes to simulate the transfer of energy and materials through the climate system. They use mathematical equations to characterize how energy and matter interact in different parts of the ocean, atmosphere, land; therefore, they are sometimes also called Atmosphere-Ocean GCMs, Earth System Models (ESMs), or simply, and most commonly, climate models. Paper 2 uses GCM data to estimate climate sensitivity and compares the results with the reported values in order to verify the robustness of our proposed empirical estimation framework. GCM data can be obtained from the Coupled Model Intercomparison Project - Phase 6 archive (CMIP6, Eyring et al., 2016).

Economic Data

Using country-year panel data, Paper 3 and paper 4 examine the effects of climate change on crop yields and economic growth, respectively. Crop yields data can be obtained from the Food and Agriculture Organization of the United Nations (FAOSTAT, http://www.fao.org/faostat/en/#data/QC). Economic indicators are available from the World Bank's World Development Indicators dataset (WDI, 2020),

1.3 Philosophy of Science

This thesis uses quantitative models to describe natural processes, assess impacts of climate change. The issue of double-counting has long been the subject of debate in the philosophical as well as statistical literature. Double counting is defined as if data have been used to construct a hypothesis, then the data should not be used again as evidence in support of the hypothesis (Deborah, 2008). That is to say, an accordance between evidence and hypothesis provides a genuine test of hypothesis only if evidence is not used in the hypothesis' construction. It is believed that double counting has the potential of posing unreliable inferences. For example, if the model is constructed in a certain way that presumes some beliefs, it is highly doubtful an inference that the belief is actually true. Although the inferences were originated from fitting the data, they were constrained to reflect what is real, or at least trying to do so. We shall not reject the existence meaning of hypothesis testing, indiscriminately disparages all procedures that involve double counting will result in negating certain reliable model validation and conclusion, thereby we are not able to generate useful conclusions from data dependent inferences. Therefore, meticulous cautiousness is required when dealing with double counting, it is the condition, property, probativeness of the hypothesis test that determine whether a double use of data in hypothesis testing is acceptable.

Popper and Notturno (1994) provides a solution for accepting a hypothesis. According to their theory, observations and experiments can be accepted as supporting a theory (or a hypothesis, or a scientific assertion) only if these observations or experiments are severe tests of the theory—or in other words, only if they result from serious attempts to refute the theory, especially from trying to find faults where these might be expected in the light of all our knowledge. Severity here is the probability that the test rejects a hypothesis h when h is false. Requiring severity is similar to requiring a high power of a statistical test to detect the falsity of h. When severity is satisfied we argue that the test is genuinely probative, otherwise a good fit between the data and hypothesis would be very difficult to generate were hypothesis incorrect. When the severity is seriously violated we may conclude that the hypothesis is not determinant in the way that helps to generate a good fit of data, i.e., such a fit could result from a fit even if the hypothesis were false. In conclusion, if the occurrence of a good fit between the data and hypothesis is impossible unless the hypothesis is true, then we could be sure that inference from the hypothesis is correct.

According to Akaike (1998), an unbiased estimate of the predictive accuracy of a model can be obtained by considering both its fit to data and its simplicity, as measured by the number of adjustable parameters it contains. A model should be simple, reduce the redundancy to the maximum degree. In practice, we give a regulation term to punish the model with more number of parameters. For the complex model to have the higher predictive ability, not only should it fit the data better, but also it fits the data sufficiently better to compensate for the loss in simplicity that it represents (Hitchcock and Sober, 2004).

At last, a caveat that should be kept in mind is that no model is perfect, models can not reflect the reality perfectly, nonetheless we could still at least learn some valuable insights about the world from the models. “All models are wrong, some are useful.” said the famous statistician George Box. We can not pursue perfection in our models, no model can simulate observations with one hundred percentage confidence. There are always randomness in the reality that can not be captured perfectly in the model, probably there are important factors that we neglected, maybe we over simplified reality with unrealistic assumptions. In all, each model is wrong in a different way. Although there is weakness in our model, they are not useless at all. All together they might provide useful perspectives to our problem to solve.

1.4 Overview of Four Papers

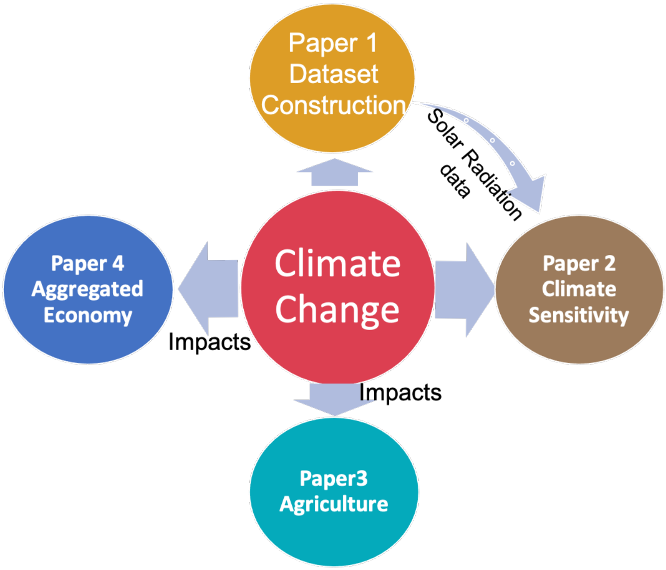

Fig. 1.4 Thesis outline.

Figure 1.4 shows a diagram of the structure of this thesis. The central topic of the thesis is climate change, revolving around which, four papers are developed. In particular, the first two papers altogether constrain the uncertainty of climate sensitivity. The first paper conducts a spatial interpolation to construct a solar radiation dataset that is used in the empirical estimation of climate sensitivity in the second paper. The last two papers are focused on assessing the agricultural and aggregated economic impacts of climate change, respectively. The constructed solar radiation dataset was also applied in the last two papers but the results show that solar radiation is not a significant factor. In what follows, I will provide a summary for each of the four papers consisting of the thesis.

1.4.1 Paper 1: Global Trends in Downward Surface Solar Radiation from Spatial Interpolated Ground Observations during 1961-2019

Paper 1 constructs a high resolution ($0.5^\circ \times 0.5^\circ$) global solar radiation dataset that spans nearly 60 years with monthly frequency and has complete global land surface coverage. The constructed dataset provides the prerequisite input, solar radiation data, for paper 2 that empirically estimates climate sensitivity.

In particular, this paper applies a machine learning method, Random Forest, to interpolate an observational solar radiation dataset. We use a wide range of explanatory variables to predict solar radiation, including climatic variables (e.g., temperature indices, precipitation, cloud coverage, vapour pressure, etc.), time point indicators (year and month), and coordinates of locations (latitude and longitude). The trained Random Forest model has remarkable performance; it is able to capture more than 90% of the total variation of global surface solar radiation. Among the predictors, we find that maximum temperature and month indicator provide the most explanatory power in predicting solar radiation. The trained model is then applied to interpolate solar radiation values for unsampled locations and thereby generating a global dataset with complete land coverage.

Based on the output dataset, we further analyze solar radiation trends on a global and a continental level. We also report seasonal patterns of historical radiation evolution.

1.4.2 Paper 2: High-sensitivity Earth System Models most Consistent with Observations

Paper 2 estimates Earth's Transient Climate Response (TCR), defined as the global mean surface air temperature change due to a doubling of atmospheric CO_2, at the time of doubling. TCR is a critical parameter for inetegrated assessment models that are extensively applied by policy makers to evaluate consequences of alternative emission scenarios and inform climate change policy.

Using the solar radiation dataset built from the first paper and other additional climate datasets, we estimated TCRs of 22 global climate models by employing an empirical framework that relates temperature to solar radiation and CO_2 in a cointegrating equilibrium relationship. The empirical TCRs provides a much narrower confidence interval ($2.3 \pm 0.4°C$) as compared to reported TCR by CMIP6 (Coupled Model Intercomparison Project). Using the narrowed distribution of TCR, we calculated the remaining carbon budgets. We find that constrained by a $1.5°C$ warming target that aligned with the Paris agreement goals, we have around nine years of current CO_2 emissions.

1.4.3 Paper 3: Heterogeneity in Climate Change Effects on Soybean Yields

Paper 3 investigates the effects of climate change on soybean yield growth. Based on a panel data analysis approach, we examine how soybean yields response to climate change from both a global and regional level. Under a global homogeneous assumption, we find a non-linear relationship between growing season average temperature and yield growth. In particular, global yield growth minimizes at $24.9°C$, meaning that warming damages are exacerbating until the optimum and, above that, a continual warming is less detrimental probably due to adaption of local crop variety to heat for countries that have been persistently hot. However, our further analyses show evidence that the global response function is not representative for all individual regions. By including regional dummies to our empirical model, we find significant heterogeneity among regions. For example, for mid- and high-latitude developed countries, temperature is not a significant factor to crop yields growth. Moreover, Southeast Asia shows a strikingly different response curve from the global one. The region indicates a parabola that maximizes at $24.34°C$, suggesting northern, cooler countries within the region, such as China, South Korea, and Japan may be beneficiaries of a warmer climate, whereas hot countries situated at the southern fringes will be affected adversely.

Compared to the large regional heterogeneity of temperature responses, the effects of precipitation are more consistent across regions. Despite of the fact that there exist various optimal precipitation levels for various regions, in general, regions will benefit from more precipitation before respective optimums and be harmed by extra precipitation above optimums. We also show the dominant effects of temperature on soybean yields as compared to precipitation.

1.4.4 Paper 4: The Relative Role of Temperature and Precipitation in Global Economic Growth

Paper 4 follows the similar logic of paper 3 but is focused on examining historical impacts of climate change on aggregate economic growth. Based on a panel of 169 countries over the period 1961-2019, we summarized climate changes that have occurred and estimated realized economic impacts of theses changes. We find pervasive warming trends for countries worldwide and a majority of them shows a rise of temperature at accelerating rates. We also find that cooler countries exhibit larger magnitude of a rise of temperature as well as larger variability than warmer countries. On the other hand, precipitation shows no evident long-term trends and precipitation varies largely across the years for countries with a large amount of rainfall.

In addition to the conventional country-year fixed effects model (FE), we applied an innovative approach—interactive fixed effects model (IE), which allows heterogeneity to enter the model in a multiplicative way. We find that the two models show highly consistent response surfaces, both indicating concave surfaces to changes in temperature and precipitation; nonetheless, the FE model has more drastic responses to extreme climate conditions. For instance, for Sub-Saharan Africa, where climate has been extremely hot and dry, the effects of historical climate change are reported as reductions of GDP growth by 0.73 and 0.58 percentage points for the FE and IE model, respectively. On a global level, the average historical impacts of climate change on GDP growth are reported as -0.30 and -0.19 percentage points by the FE and IE model, respectively.

Summary of Author Contributions in Papers

The first paper is a collaborative work with Thomas Leirvik and Martin Wild. T.L. and I initiated and conceived the research. T.L. and M.W. provided invaluable comments and guidance as I implemented the empirical calculation. All of us contributed in writing the paper. I am the first and corresponding author of this paper.

In the second paper, I collaborated with Thomas Leirvik, Trude Storelvmo, Kari Alterskjær, Peter C.B. Phillips, and Christopher J. Smith. My contribution to the paper is that I performed data integration and technical analysis relevant to TCR estimation. I am the first and corresponding author of this paper.

The third paper is a single-author paper initiated, implemented, and written by me. In the last paper, I collaborated with Thomas Leirvik and Hande Karabiyik. T.L. and H.K. conceived and initiated the research. H.K. implemented the statistical tests and empirical estimation of the response function. I calculated historical impacts of climate change based on the estimated response function. T.L. provided significant insights in improving the model. H.K. and I wrote the paper with input from T.L. Since this project is still in progress, we have not decided yet the order of contribution.

References

Akaike, H. (1998). Information Theory and an Extension of the Maximum Likelihood Principle. pages 199–213. Springer, New York, NY.

Auffhammer, M., Hsiang, S., Schlenker, W., and Sobel, A. (2013). Using Weather Data and Climate Model Output in Economic Analyses of Climate Change. Technical report, National Bureau of Economic Research, Cambridge, MA.

Auffhammer, M., Ramanathan, V., and Vincent, J. R. (2012). Climate change, the monsoon, and rice yield in India. *Climatic Change*, 111(2):411–424.

Barreca, A., Clay, K., Deschenes, O., Greenstone, M., and Shapiro, J. S. (2016). Adapting to climate change: The remarkable decline in the US temperature-mortality relationship over the Twentieth Century. *Journal of Political Economy*, 124(1):105–159.

Barreca, A. I. and Shimshack, J. P. (2012). Absolute humidity, temperature, and influenza mortality: 30 years of county-level evidence from the united states. *American Journal of Epidemiology*, 176(SUPPL. 7).

Berlemann, M. and Wenzel, D. (2018). Precipitation and Economic Growth. *CESifo Working Paper No. 7258*.

Bhargava, A., Jamison, D. T., Lau, L. J., and Murray, C. J. (2001). Modeling the effects of health on economic growth. *Journal of Health Economics*, 20(3):423–440.

Bhatt, S., Gething, P. W., Brady, O. J., Messina, J. P., Farlow, A. W., Moyes, C. L., Drake, J. M., Brownstein, J. S., Hoen, A. G., Sankoh, O., Myers, M. F., George, D. B., Jaenisch, T., William Wint, G. R., Simmons, C. P., Scott, T. W., Farrar, J. J., and Hay, S. I. (2013). The global distribution and burden of dengue. *Nature*, 496(7446):504–507.

Bloom, D. E., Canning, D., and Sevilla, J. (2004). The effect of health on economic growth: A production function approach. *World Development*, 32(1):1–13.

Budyko, M. I. (1969). The effect of solar radiation variations on the climate of the Earth. *Tellus*, 21(5):611–619.

Bureau of Meteorology (2020). Annual climate statement 2020. Technical report.

Burke, E. J. and Brown, S. J. (2008). Evaluating uncertainties in the projection of future drought. *Journal of Hydrometeorology*, 9(2):292–299.

Burke, E. J., Brown, S. J., and Christidis, N. (2006). Modelling the recent evolution of global drought and projections for the twenty-first century with the Hadley Centre climate model. *Journal of Hydrometeorology*, 7(5):1113–1125.

Burke, M., Hsiang, S. M., and Miguel, E. (2015). Global non-linear effect of temperature on economic production. *Nature*, 527(7577):235–239.

Carballar-Lejarazú, R., Ogaugwu, C., Tushar, T., Kelsey, A., Pham, T. B., Murphy, J., Schmidt, H., Lee, Y., Lanzaro, G. C., and James, A. A. (2020). Next-generation gene drive for population modification of the malaria vector mosquito, Anopheles gambiae. *Proceedings of the National Academy of Sciences of the United States of America*, 117(37):22805–22814.

Carleton, T. A. and Hsiang, S. M. (2016). Social and economic impacts of climate.

Chiacchio, M. and Wild, M. (2010). Influence of NAO and clouds on long-term seasonal variations of surface solar radiation in Europe. *Journal of Geophysical Research Atmospheres*, 115(10).

Collins, F. C. (1995). *A comparison of spatial interpolation techniques in temperature estimation*. PhD thesis, Virginia Tech.

Craig, M., Le Sueur, D., and Snow, B. (1999). A climate-based distribution model of malaria transmission in sub-Saharan Africa.

Dai, A. (2013). Increasing drought under global warming in observations and models. *Nature Climate Change*, 3(1):52–58.

Deborah, M. (2008). How to discount double-counting when it counts: Some clarifications. *The British Journal for the Philosophy of Science*, Volume 59.

Dell, M., Jones, B. F., and Olken, B. A. (2009). Temperature and income: Reconciling new cross-sectional and panel estimates. *American Economic Review*, 99(2):198–204.

Dell, M., Jones, B. F., and Olken, B. A. (2012). Temperature shocks and economic growth: Evidence from the last half century. *American Economic Journal: Macroeconomics*, 4(3):66–95.

Deschenes, O. (2014a). Temperature, human health, and adaptation: A review of the empirical literature. *Energy Economics*, 46:606–619.

Deschenes, O. (2014b). Temperature, human health, and adaptation: A review of the empirical literature. *Energy Economics*, 46:606–619.

Diffenbaugh, N. S. and Burke, M. (2019). Global warming has increased global economic inequality. *Proceedings of the National Academy of Sciences of the United States of America*, 116(20):9808–9813.

Duan, Y., Kumar, S., and Kinter, J. L. (2021). Evaluation of Long-term Temperature Trend and Variability in CMIP6 Multimodel Ensemble. *Geophysical Research Letters*, page e2021GL093227.

Erxleben, J., Elder, K., and Davis, R. (2002). Comparison of spatial interpolation methods for estimating snow distribution in the Colorado Rocky Mountains. *Hydrological Processes*, 16(18):3627–3649. https://doi.org/10.1002/hyp.1239.

Eyring, V., Bony, S., Meehl, G. A., Senior, C. A., Stevens, B., Stouffer, R. J., and Taylor, K. E. (2016). Overview of the Coupled Model Intercomparison Project Phase 6 (CMIP6) experimental design and organization. *Geoscientific Model Development*, 9(5):1937–1958.

Flato, G. and Marotzke, J. (2013). *Evaluation of Climate Models*. Cambridge University Press.

Gerten, D., Rost, S., von Bloh, W., and Lucht, W. (2008). Causes of change in 20th century global river discharge. *Geophysical Research Letters*, 35(20):20405.

Gething, P. W., Smith, D. L., Patil, A. P., Tatem, A. J., Snow, R. W., and Hay, S. I. (2010). Climate change and the global malaria recession. *Nature*, 465(7296):342–345.

Gething, P. W., Van Boeckel, T. P., Smith, D. L., Guerra, C. A., Patil, A. P., Snow, R. W., and Hay, S. I. (2011). Modelling the global constraints of temperature on transmission of Plasmodium falciparum and P. vivax. *Parasites and Vectors*, 4(1):1–11.

Hansen, B. (2019). *Econometrics*.

Harris, I., Osborn, T. J., Jones, P., and Lister, D. (2020). Version 4 of the CRU TS monthly high-resolution gridded multivariate climate dataset. *Scientific Data*, 7(1).

Hitchcock, C. and Sober, E. (2004). Prediction versus Accommodation and the Risk of Overfitting. *The British Journal for the Philosophy of Science*, 55(1):1–34.

Ivinson, A. J. (2002). Macroeconomics and Health: Investing in Health for Economic Development. *Nature Medicine*, 8(6):551–552.

Jiang, Y. (2008). Prediction of monthly mean daily diffuse solar radiation using artificial neural networks and comparison with other empirical models. *Energy Policy*, 36(10):3833–3837. https://doi.org/10.1016/J.ENPOL.2008.06.030.

Jones, P., Hulme, M., Briffa, K., Jones, C., Mitchell, J., and Murphy, J. (1996). Summer moisture variability over Europe in the Hadley Centre GCM using the Palmer Drought Severity Index. *International Journal of Climatology*, 16(2):155–172.

Kucharik, C. J. and Serbin, S. P. (2008). Impacts of recent climate change on Wisconsin corn and soybean yield trends. *Environmental Research Letters*, 3(3):34003.

Kukal, M. S. and Irmak, S. (2018). Climate-Driven Crop Yield and Yield Variability and Climate Change Impacts on the U.S. Great Plains Agricultural Production. *Scientific Reports*, 8(1):1–18.

Leirvik, T. and Yuan, M. (2021). A Machine Learning Technique for Spatial Interpolation of Solar Radiation Observations. *Earth and Space Science*, 8(4):e2020EA001527.

Lewis, N. S. (2016). Research opportunities to advance solar energy utilization. *Science*, 351(6271):aad1920.

Lobell, D. B. and Burke, M. B. (2008). Why are agricultural impacts of climate change so uncertain? the importance of temperature relative to precipitation. *Environmental Research Letters*, 3(3):034007.

Norris, J. R. and Wild, M. (2007). Trends in aerosol radiative effects over Europe inferred from observed cloud cover, solar "dimming," and solar "brightening". *Journal of Geophysical Research Atmospheres*, 112(8).

Obryk, M. K., Fountain, A. G., Doran, P. T., Lyons, W. B., and Eastman, R. (2018). Drivers of solar radiation variability in the McMurdo Dry Valleys, Antarctica. *Scientific Reports*, 8(1):5002.

Paaijmans, K. P., Blanford, S., Chan, B. H., and Thomas, M. B. (2012). Warmer temperatures reduce the vectorial capacity of malaria mosquitoes. *Biology Letters*, 8(3):465–468.

Phillips, P. C., Leirvik, T., and Storelvmo, T. (2020). Econometric estimates of Earth's transient climate sensitivity. *Journal of Econometrics*, 214(1):6–32.

Popper, K. R. K. R. and Notturno, M. A. (1994). *The myth of the framework : in defence of science and rationality*. Routledge.

Rind, D., Goldberg, R., Hansen, J., Rosenzweig, C., and Ruedy, R. (1990). Potential evapotranspiration and the likelihood of future drought. *Journal of Geophysical Research*, 95(D7):9983–10004.

Sanchez-Lorenzo, A., Wild, M., Brunetti, M., Guijarro, J. A., Hakuba, M. Z., Calbó, J., Mystakidis, S., and Bartok, B. (2015). Reassessment and update of long-term trends in downward surface shortwave radiation over Europe (1939-2012). *Journal of Geophysical Research*, 120(18):9555–9569.

Scafetta, N. and West, B. J. (2005). Estimated solar contribution to the global surface warming using the ACRIM TSI satellite composite. *Geophysical Research Letters*, 32(18):1–4.

Schlenker, W., Hanemann, W. M., and Fisher., A. C. (2005). Will U.S. Agriculture Really Benefit from Global Warming? Accounting for Irrigation in the Hedonic Approach on JSTOR. *The American Economic Review*, 95(1):395–406.

Schlenker, W. and Lobell, D. B. (2010). Robust negative impacts of climate change on African agriculture. *Environmental Research Letters*, 5(1):014010.

Scudellari, M. (2019). Self-destructing mosquitoes and sterilized rodents: the promise of gene drives.

Scudiero, E., Corwin, D. L., Morari, F., Anderson, R. G., and Skaggs, T. H. (2016). Spatial interpolation quality assessment for soil sensor transect datasets. *Computers and Electronics in Agriculture*, 123:74–79. https://doi.org/10.1016/J.COMPAG.2016.02.016.

Seppanen, O., Fisk, W. J., and Faulkner, D. (2003). Cost benefit analysis of the night-time ventilative cooling in office building.

Shapiro, L. L., Whitehead, S. A., and Thomas, M. B. (2017). Quantifying the effects of temperature on mosquito and parasite traits that determine the transmission potential of human malaria. *PLoS Biology*, 15(10):e2003489.

Stjern, C. W., Kristjánsson, J. E., and Hansen, A. W. (2009). Global dimming and global brightening - An analysis of surface radiation and cloud cover data in northern Europe. *International Journal of Climatology*, 29(5):643–653.

Storelvmo, T., Leirvik, T., Lohmann, U., Phillips, P. C. B., and Wild, M. (2016). Disentangling greenhouse warming and aerosol cooling to reveal Earth's climate sensitivity. *Nature Geoscience*, 9(4):286–289.

Sun, H., Gui, D., Yan, B., Liu, Y., Liao, W., Zhu, Y., Lu, C., and Zhao, N. (2016). Assessing the potential of random forest method for estimating solar radiation using air pollution index. *Energy Conversion and Management*, 119:121 – 129. https://doi.org/10.1016/j.enconman.2016.04.051.

Wang, K. and Dickinson, R. E. (2013). Contribution of solar radiation to decadal temperature variability over land. *Proceedings of the National Academy of Sciences of the United States of America*, 110(37):14877–14882.

WDI (2020). Word Development Indicators.

Wild, M. (2009). Global dimming and brightening: A review. *Journal of Geophysical Research*, 114(D10):D00D16.

Wild, M., Ohmura, A., Schär, C., Müller, G., Folini, D., Schwarz, M., Zyta Hakuba, M., and Sanchez-Lorenzo, A. (2017). The Global Energy Balance Archive (GEBA) version 2017: A database for worldwide measured surface energy fluxes. *Earth System Science Data*, 9(2):601–613.

Zhou, Q., Flores, A., Glenn, N. F., Walters, R., and Han, B. (2017). A machine learning approach to estimation of downward solar radiation from satellite-derived data products: An application over a semi-arid ecosystem in the us. *PloS one*, 12(8):e0180239. https://doi.org/10.1371/journal.pone.0180239.

CHAPTER 2

Global Trends in Downward Surface Solar Radiation from Spatial Interpolated Ground Observations during 1961-2019[1]

Collaborative Paper with Thomas Leirvik[1] and Martin Wild[2]

[1] *Nord University Business School, Norway*
[2] *Institute for Atmospheric and Climate Science, ETH Zurich,*
Zürich, Switzerland

Abstract

Downward surface solar radiation (SSR) is a crucial component of the Global Energy Balance, affecting temperature and the hydrological cycle profoundly, and it provides crucial information about climate change. Many studies have examined SSR trends, however they are often concentrated on specific regions due to the limited spatial coverage of ground based observation stations. To overcome the spatial limitation, this study performs a spatial interpolation based on a machine learning method, Random Forest, to interpolate monthly SSR using a number of climatic variables (e.g., various temperature indices, cloud coverage), time point indicators (the year and month of an SSR record), and coordinates of locations (latitude and longitude of the SSR record).

The predictors that provide the largest explanatory power for monthly SSR are monthly maximum temperature and month of the interpolation (representative for the TOA insolation conditions). The output of the spatial interpolation is a 0.5° × 0.5° monthly gridded dataset with complete land coverage over the period 1961-2019, which is used afterwards in a comprehensive trend analysis for *i*) each continent separately, and *ii*) the entire globe.

---

[1] Paper submitted to *Journal of Climate.* Revision & Resubmit.

The continental level analysis reveals the major contributors for the global dimming and brightening. In particular, the global dimming is primarily dominated by negative trends in Asia and North America; whereas Europe and Africa, as a matter of fact, have shown significant increases in SSR over the dimming period 1961-1984. Over the brightening period 1985-2019, Europe and Oceania are the largest two contributors.

2.1 Introduction

Surface solar radiation is a crucial climate variable and a main constitute of the Global Energy Balance, playing an important role in temperature change and the hydrological cycle (e.g., Budyko, 1969; Pfeifroth et al., 2018; Obryk et al., 2018). The positive trend in downward surface solar radiation since the 1980s in combination with increasing greenhouse gases lead to an intensification of the land-based hydrological cycle (Wild et al., 2008; Wild and Liepert, 2010; Wild, 2016). Moreover, it has profound impacts on various aspects of society and economy, especially on agriculture. For example, crop yields could be significantly influenced not only by increases or decreases of solar radiation through enhancing or weakening of photosynthesis, a so-called “insolation effect”, but also indirectly by the resulting temperature change from solar radiation variations (Greenwald et al., 2006; Roderick and Farquhar, 2012; Gupta et al., 2017; Proctor et al., 2018).

To analyze the drivers and economic impact of climate change, it is of critical importance to have an understanding of surface solar radiation (hereafter referred to as SSR), in terms of its trends, levels, and variations. Ground-based observations are believed to be the most reliable long-term data source for solar radiation, and have been used in many climate studies to monitor its evolution (e.g., Wild et al., 2005; Sanchez-Lorenzo et al., 2015, 2017; Pfeifroth et al., 2018). SSR is a key driver of climate, and observations have been applied to study its effect on temperature (e.g. Storelvmo et al., 2016; Phillips et al., 2020. Despite their reliability as compared to other sources, one of the main drawbacks of ground-based measurements is their limited temporal and spatial coverage. For a start, extensive SSR observations have a relatively short history of only multiple decades; they were not widely available until the 1960s and have a time lag effect due to the time-consuming process of data collecting and homogenizing. Moreover, continuity of observed time series is often interrupted by missing values in observational stations due to device failure and operational malfunction. As for spatial coverage, climate stations tend to be concentrated in developed regions which can provide the financial and technical support to maintain the devices. They also tend to cluster on flat terrain rather than mountainous areas where it could be hard to establish stations in the first place. For areas with sparse station coverage, the available observations from the stations might not be sufficient to represent the overall trend over the areas. Therefore it is essential to extrapolate the available observations, in the dimension of both space and time, thereby enabling a more comprehensive overview, which better represents all areas with continuous time series. The method that aims to fill gaps in spatial datasets is called spatial interpolation. Conventional spatial interpolation methods such as Inverse Distance Weighting, Kriging, splines, etc., have seen extensive applications in various climate processes (e.g., Collins, 1995; Erxleben et al., 2002; Scudiero et al., 2016). This study contributes to, and expands, the existing literature by applying a novel machine learning method to interpolate a station observation dataset of SSR.

Machine learning methods have seen an increasing number of applications in spatial interpolation and shown effectiveness in reproducing and predicting climate variables with high accuracy and low uncertainty (see e.g., Jiang, 2008; Sun et al., 2016; Zhou et al., 2017). Qin et al. (2019) compared the performance of four physically deterministic models with eight machine learning models in an application of reproducing data of a certain type of radiation and reported outperformance of the machine learning methods. Existing literature are mostly focused on simulating regional patterns of climate variables, for example, Zhou et al. focus on the US whereas Qin et al. focus on China. In this study we aim for a comprehensive study of SSR on a global scale; therefore, it is essential that the selected method should be able to cope with a large quantity of data. Among a wide range of machine learning approaches, *Random Forest* has exceptional advantages in handling a large number of explanatory variables and in its capacity of processing large datasets due to its computational efficiency (Firth et al., 2005; Myoung et al., 2020). The study of Leirvik and Yuan

(2020) compared the performance of Random Forest with those of seven other conventional (deterministic) spatial interpolation methods (e.g., linear regression models, Kriging, Regression Kriging) in an application of predicting global SSR, and showed a profound advantage of Random Forest in prediction accuracy and performance stability. In their application they also investigated the potential of other machine learning models (i.e., *support vector machine* and *gradient boosting machine*), but they found it is hard for other machine learning methods to converge in the specific application given the global scale of the input dataset and the large number of explanatory variables. Due to the superior performance of the Random Forest method in the settings described above, which is similar to the setting in this paper, we choose to apply the Random Forest model to unsampled areas, thereby constructing a global, and more complete, dataset than has been constructed before.

In this paper, we apply Random Forest to a global SSR dataset, the dataset of the Global Energy Balance Archive (GEBA). A total of 15 variables are selected as predictors for SSR, including 9 climatic variables (various temperature indices, cloud cover, frost days, etc.), geographical coordinates (i.e., longitude and latitude), altitude, urbanization and temporal indicators that indicate the time point (year and month) of the observed/simulated SSR record. The model is first trained on available observations in the dataset (with global average R squared and mean absolute error being 0.91 and 11.86 Wm^{-2}, respectively), and then the model is applied to interpolate values at unsampled locations. The result is a $0.5° \times 0.5°$ monthly gridded dataset, conforming with the resolution and time step of the input CRU dataset. The constructed dataset provides SSR estimations with complete global land coverage and temporal coverage of 59 years (1961-2019). Based on this dataset, remote land areas, such as Africa, Siberia, etc., that were barely investigated before, are made accessible for investigation of their long-term trends.

Trends could vary, or even reverse, during a multidecadal time period, making it highly important to detect potential breakpoints over the whole period. In fact, not only are the long-term trends reaching far back in the past of interest, it is also of critical importance to identify the most recent sustainable trends up until now. Particularly, global SSR experiences a widespread reduction (on the order of $3-9\ Wm^{-2}$ per decade) from the 1950s to the 1980s and followed by an increase (on the order of $1-4\ Wm^{-2}$ per decade), which are referred to as "global dimming" and "global brightening", respectively (Wild et al., 2005; Wild, 2009; Gilgen et al., 2009; Wild, 2012; Pfeifroth et al., 2018). Aggregated series over a region reveal the overall inter-annual variation and trends, but sub-regional trends are neutralized, or masked, by the aggregation if they are of opposite sign, which is often the case in many continents. Therefore, the spatial distribution is investigated for each continent in this study, and the results show significant spatial diversity.

The paper is organized as follows: section 2 describes the datasets and methods used in the spatial interpolation; model performance and trend analyses based on the constructed dataset are discussed in section 3; section 4 is a discussion of the results found in the paper.

2.2 Datasets and Method

2.2.1 Method

Random Forest (RF) is a decision tree technique for regression and classification (Breiman, 2001). In contrast to conventional decision tree methods, Random Forest constructs a forest of decision trees that operates as a predicting ensemble whose prediction accuracy is higher than that of any individual tree. Randomness in the RF is the distinctive characteristic that makes it one of the most powerful and widely-used machine learning methods in recent applications (Sun et al., 2016; Zhou et al., 2017; Xu et al., 2018).

There are mainly two sources of this randomness. Firstly, the RF uses bootstrap to generate training sets for each decision tree which allows for replacement. The process is often known as bagging; it helps to improve the performance stability by reducing variance and avoiding over-fitting in the algorithm. Secondly, it incorporates feature randomness in that each tree in the forest corresponds to only a random subset of independent variables. This adds more diversity in the trees, resulting in a higher utilization for various regressors in parallel, rather than splitting at the most separation among observations sequentially in one decision tree. The parameters that control the two types of randomness are the number of bootstraps (i.e., the number of independent samples used to train the model) and the degree of feature randomness (i.e., the number of candidate independent variables to split at in each node). Through a parameter tuning process the number of bootstraps is set to 700 and the degree of feature randomness is set to 8 (see Supporting Information (SI) A.3.1 for details).

A range of variables are used as predictors for SSR, including climatic variables that are closely related to the variation of SSR, geographical characteristics of locations, together with temporal stamps of the records. Table 2.1 summarizes the symbols and detailed definition of the predictors.

Table 2.1 Predictors summary

Variable Category	Symbol	Definition
Climatic Variables	cld	cloud cover as percentage
	dtr	diurnal temperature range in $°C$
	frs	number of days with ground frost
	pre	monthly total precipitation data in mm/month
	tmn	minimum temperature in $°C$
	tmp	mean temperature in $°C$
	tmx	maximum temperature in $°C$
	vap	vapour pressure in hPa
	wet	number of rainy days in a month
Geographical Variables	lat	latitude of the location
	lon	longitude of the location
	alt	terrain altitude in m
	urban	1 if urban, 0 if rural
Temporal Variables	year	year of the observation/estimation
	mon	month of the observation/estimation

Three error metrics are calculated for model evaluation: Mean Absolute Error (MAE), Root Mean Squared Error (RMSE), and R squared (R^2). They are given by the following equations:

$$\begin{aligned} MAE &= \frac{1}{n}\sum_{i=1}^{n}|\hat{z}_i - z_i| \\ RMSE &= \sqrt{\frac{1}{n}\sum_{i=1}^{n}(\hat{z}_i - z_i)^2} \\ R^2 &= 1 - \frac{\sum_{i=1}^{n}(\hat{z}_i - z_i)^2}{\sum_{i=1}^{n}(z_i - \bar{z}_i)^2} \end{aligned} \tag{2.1}$$

where n is the number of predictions, $\hat{z}_i$ is the predicted value of station i, and z_i is the observed value of station i. No percentage error measure is used in the paper because it could be biased toward very large values by small observation values close to zero, which are common in winter.

2.2.2 Datasets

Ground-based all-sky SSR observations were obtained from the Global Energy Balance Archive (GEBA, Wild et al. (2017)). The GEBA dataset contains monthly SSR values from around 1500 observation stations scattered on all continents except for Antarctica. Table 2.2 provides a summary of the number of stations and monthly observations in each station. Europe accounts for more than one-third of the global stations, making it the most extensively covered continent (refer to SI Figure A.1 for a global station distribution map). The dataset has an unparalleled temporal coverage, which starts from the early 1950s until 2013. This dataset has been previously examined for temporal homogeneity by Sanchez-Lorenzo et al. (2013) and widely used in the literature since the 1990s (see e.g., Ohmura and Gilgen (1993); Arking (1996); Nabat et al. (2014); Wang et al. (2014); Cherian et al. (2014); He et al. (2018)).

The climatic variables as predictors for SSR are available from the Climate Research Unit Time-series data version 4.04 (CRU-TS v.4.04, Harris et al. (2020)). The CRU dataset provides high resolution (0.5° × 0.5°) gridded data of monthly observations for a range of meteorological variables over the period 1901-2019 (Table 2.1). A 0.5°×0.5° global altitude map is available from NESDIS (1995). The GRUMP dataset (V1) (CIESIN, 2004) provides a 30 arc-second urban extents grid based on 1995 data for all land areas except Antarctica and parts of the Greenland ice sheet. Each grid is classified as either rural or urban.

Table 2.2 Number of stations and observations in each continent

Continent	**Abbr.**[a]	**# of stations**[b]	**# of obs.**[c]
South America	SA	134	13,362
Oceania	OC	76	13,549
Africa	AF	234	33,238
North America	NrA	214	37,427
Asia	AS	312	98,912
Europe	EU	516	131,734
Total		1486	328,222

[a] Abbreviation for continent names.
[b] Number of stations in the continent.
[c] Number of monthly observations in the continent.

In order to merge the GRUMP with the CRU data, each 0.5° × 0.5° grid cell was obtained as the mean of the 3600 GRUMP values contained in the cell.

The training dataset is obtained by co-locating the GEBA stations with corresponding gridboxes in the gridded datasets, such that for each station in the GEBA a range of predictor variables as well as the SSR values are matched by month. Limited by the data availability in the GEBA dataset, the training dataset covers the period from 1961 until 2013. For interpolation, all three gridded datasets are merged and provide the input variables for the trained RF model. The interpolation data covers the period from 1961-2019, with the end year given by the extension of the CRU dataset.

2.3 Results

2.3.1 Estimation and Evaluation

A continent-by-continent 10-fold cross validation (CV) was implemented on the training dataset, such that each continent's distinctive characteristics is sufficiently accounted for. Otherwise, if a global universal model is trained, the trained model would be biased towards the SSR dynamics of the continent with the most concentrated observations, i.e., Europe. 10-fold CV means to partition the training dataset into 10 equal size subsamples. Of the 10 subsamples, a single subsample is retained as the validation data for testing the model, and the remaining 9 subsamples are used as the data to train the model. The cross-validation is repeated 10 times, such that each of the 10 subsamples is used once as validation data. Combining together simulations for all 10 validation subsets generates a complete out-of-sample simulation (i.e., the data used for validation is not used in training) for each observation.

Table 2.3 shows the error measures of monthly anomalies and raw values (or unprocessed values) of SSR for each continent. In order to obtain monthly anomalies, for each station raw monthly SSR values are deseasonalized by subtracting the 1961-2013 mean for the corresponding month, or the mean over the sub-period during which the station existed/exists. Stations exiting less than 15 years are excluded to alleviate bias brought from stations that only existed briefly in history. The R^2 of raw values range from the lowest 0.79 (South America) to the highest 0.97 (North America and Europe), with a global average of 0.91. This indicates that our RF model captures approximately 91% of the global SSR variation, primarily induced by the seasonal cycles. If removing seasonality from SSR, the R^2 calculated based on monthly anomalies remain to be reasonably high for Oceania, North America, Asia, and Europe, indicating the model's ability in capturing interannual variabilities of these continents; generally more than 35% of the interannual variability and nearly 50% for Europe. On the other hand, the model is not as effective in capturing interannual variabilities of SSR in South America and Africa, with R^2 of anomalies being only 0.09 and 0.11, respectively. This means that the large values of R^2 of raw values are dominated by seasonality in the two continents. The small values of R^2 based on monthly anomalies could be possibly due to either the limitation of the model's simulation capacity or the weaker interannual variability in the continents.

RF is a data-intensive machine learning approach which learns model features solely based on input data and does not rely on any presumptions about model structure or specification; the performance of which is highly dependent on the input training data, from perspectives of both quality and quantity. Note that the RF model was trained for per continent, that is, data characteristics in each continent affects its performance. Specifically, possible reasons that lead to the lower RF performance in South America and Africa include, but are not limited to, the relatively smaller amount of data available and/or the lack of homogeneity in the continents' data. The scatter plots of simulations against observations (Figure 2.1) provide further graphical confirmation of this. The continents with better performance show highly clustered points alongside the regression line, in contrast to South America and Africa (Figure 2.1AB), which show more scattered points away from the regression line.

Table 2.3 Error measures for RF simulations

	Anomalies			**Raw**
Continent	**MAE.ano**	**RMSE.ano**	**R.Squared.ano**	**R.Squared.raw**
South America	17.97	24.40	0.09	0.79
Africa	13.62	18.42	0.11	0.87
Oceania	10.03	14.33	0.37	0.96
North America	9.29	13.33	0.39	0.97
Asia	11.84	16.67	0.39	0.92
Europe	8.42	12.95	0.49	0.97
Global Avg.	11.86	16.68	0.30	0.91

Monthly anomalies are calculated as the deviation from the 1961-2013 mean.

From the permutation variable importance analysis (Figure 2.2), we see that the most important variable in determining monthly SSR is not surprisingly *month*. The strong influence of the *month* comes from the fact that SSR has a strong seasonal cycle, at least outside the tropics, so for a prediction of SSR on a monthly basis it is essential to know which month/time of the year it is. On the other hand, the physical process behind this *month* variable would then be the varying incoming solar radiation at the Top of Atmosphere (TOA) over the course of a year (determined by astronomical factors). So one could see the *month* also as an indication of the TOA insolation at the location to be interpolated. Latitude is the third most influential indicator; it represents the spatial distribution of SSR, more specifically, SSR varies largely as latitude changes, while longitude (the 9th important indicator) makes little contribution in estimating SSR. However, while the above quantities govern the seasonal and latitudinal distribution of SSR, they do not influence the estimation of the SSR trends. These are determined by the climatic variables, among which temperature indices (i.e., *tmx*, *tmp*, *dtr*, *tmn*) and cloud coverage (*cld*) provide the most explanatory power. Particularly, monthly maximum temperature (*tmx*)

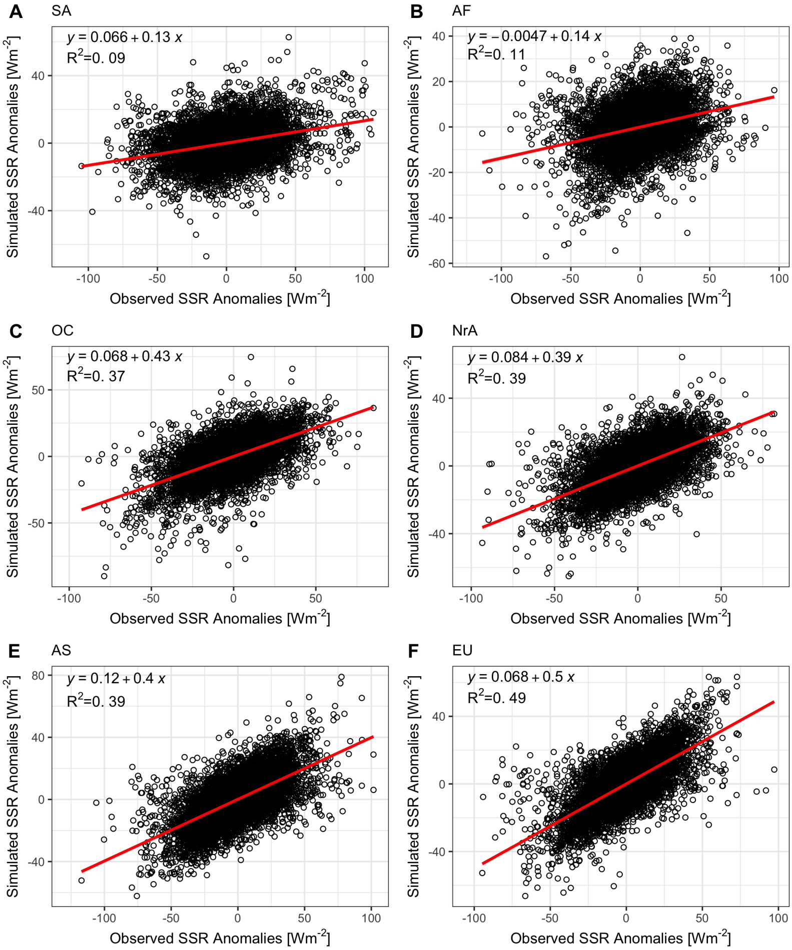

Fig. 2.1 Simulated against observed monthly anomalies. The red line is obtained by regressing simulated SSR on observed SSR, together with the corresponding equation and R squared. R^2 is the coefficient of determination of the regression. See SI Figure A.4 for a scatter plot counterpart of SSR raw values.

is the second most important variable, only second to *month*. Monthly average temperature and diurnal temperature range are also important indicators for SSR trends.

2.3.2 Interpolated SSR Dataset Trend Analysis

The 10-fold cross validation (CV) shows the RF model's capability in out-of-sample estimation of SSR. In order to make use of the SSR information in

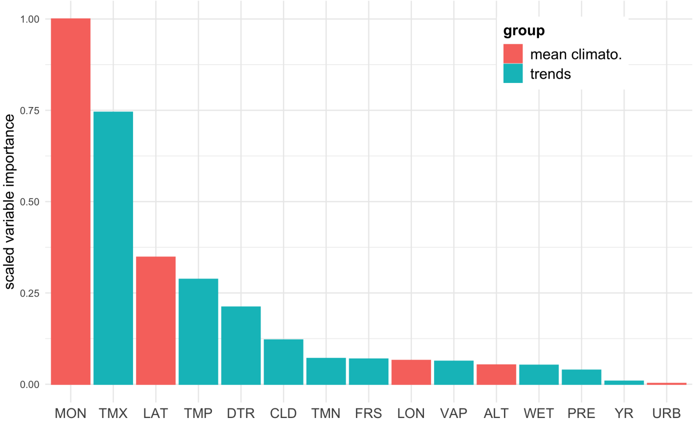

Fig. 2.2 Random Forest permutation variable importance. All importance values are scaled by the largest importance. The variables are classified into two groups: the climate variables that govern the SSR trends (in blue); and the static variables (e.g., latitude) and month (a proxy of TOA) that determine the mean climatologies of SSR and have no influence on the trends (in coral).

the GEBA dataset exhaustively, all available SSR observations (instead of 9 out of 10 subsamples used in the 10-fold CV) are used to train the RF model per continent. The trained RF models are then applied to the interpolation data. The result of the interpolation is a 0.5 by 0.5 degree gridded monthly SSR dataset over the period 1961-2019 with complete coverage over global land areas. The resolution and the time span is determined by the input climatic variables from the CRU datasest. Note that the GEBA (training) dataset has substantial amount of observations only until 2013. By extending the prediction period up until 2019, we assume the prediction relationship between SSR and the predictors remain the same for the history and onwards.

A station in the GEBA dataset—station 1188—is given as an example to illustrate the procedure. The station is located at Locarno-Monti (46.17N, 8.78E), Switzerland, and is one of the longest-standing stations in Europe. We started with the observations (shown by the red lines in Figure 2.3) from the GEBA dataset. A 10-fold CV was implemented on Europe and thereby generating out-of-sample estimations corresponding to the observations. The estimation series are shown by the black lines. Then all available data in Europe were used to train a RF model which was later used in interpolation for each gridbox in Europe. By extracting the values in the gridbox in which station 1188 is located, interpolation series are obtained (shown by the blue lines). We see that the interpolation series approximate the observations more precisely than the simulations, this is because the interpolation is an in-sample forecast which uses 10% more data than the simulations which are based on the 10-fold CV. By comparing the blue lines with the red lines, we see that the interpolation series are able to capture the observed SSR variation with reasonable accuracy, indicating the robustness of the RF model and the reliability of the generated interpolation series.

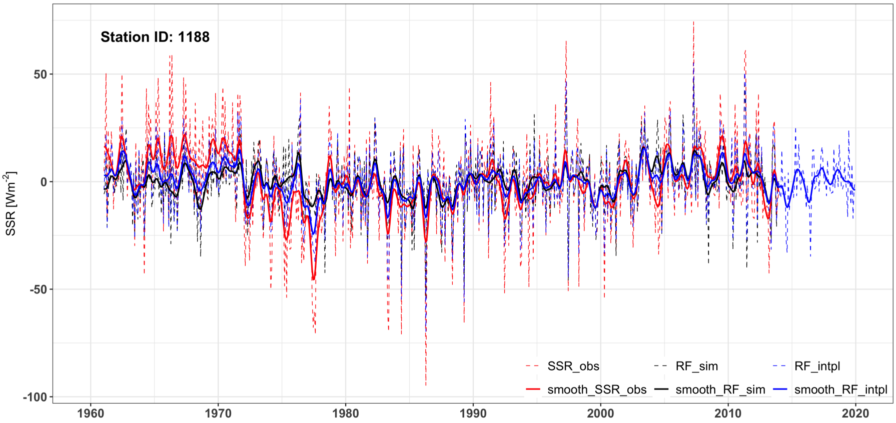

Fig. 2.3 Monthly anomalies for station 1188, Locarno-Monti, Switzerland. Monthly SSR anomaly series (dashed lines) are shown for observations (the red dashed line), simulations (the black dashed line), and interpolations (the blue dashed line), together with their corresponding smoothed series (solid lines) using 12-month Gaussian kernel. The series are expressed as anomalies from the 1961-2019 mean.

Trend Overview over the Entire Period

Annual anomalies for global land areas and for each continent are shown in Figure 2.4 and 2.5. The global average SSR exhibits rapid dimming trends from 1961 until the mid 1980s, followed by a moderate reversal. A similar reversal is observed in Oceania, North America, and South America, in contrast to the relatively continuous positive trends in Europe and Africa. Asia had a drastic dimming period from 1961 until early 1990s and the continental average SSR has been stable since then.

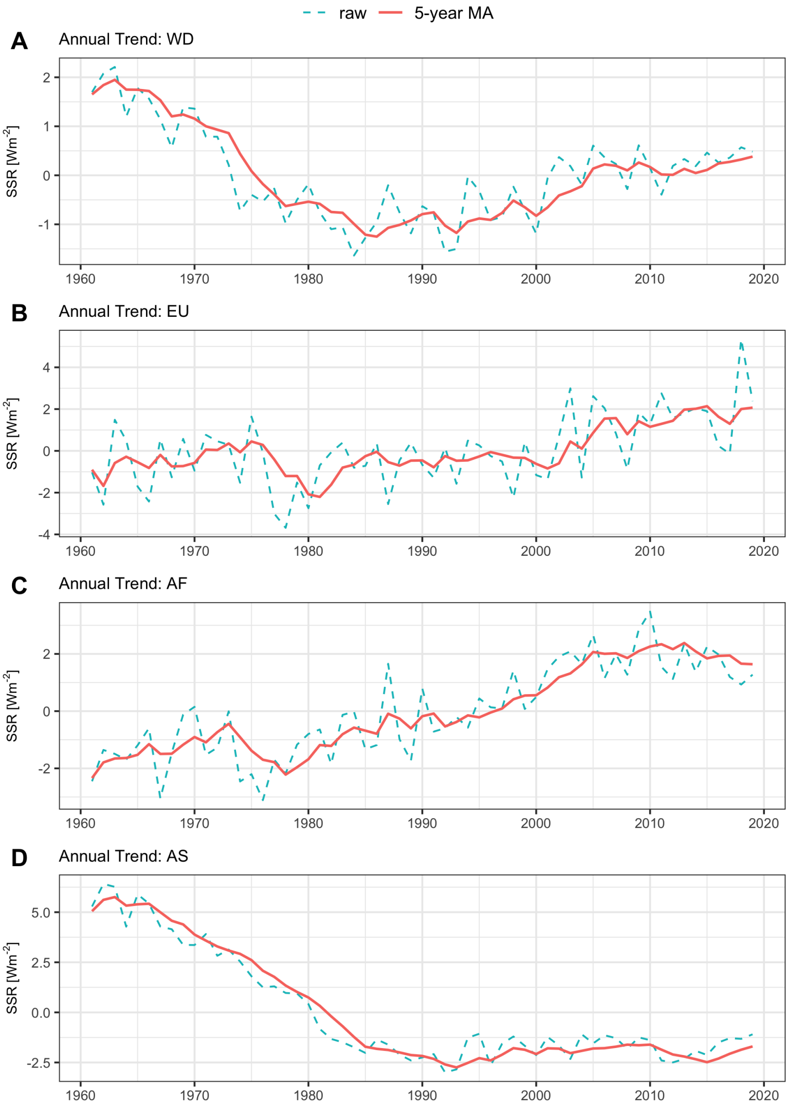

Fig. 2.4 Annual anomalies over the period 1961-2019, part I. The raw series is shown by the green dashed line, and the 5-year moving average (MA) series is shown by the coral solid line. When the number of years is less than 5, a partial moving average is used for the available years up until the time point. The anomaly series are based on the average of the period 1961-2019. Subplots show results respectively for: A-World, B-Europe, C-Africa, D-Asia. Refer to SI Figure A.5—Figure A.8 for the continents' monthly anomaly figures.

Although the global trend reversal takes place at the mid 1980s, each continent shows different breakpoints, making it of interest to detect structural

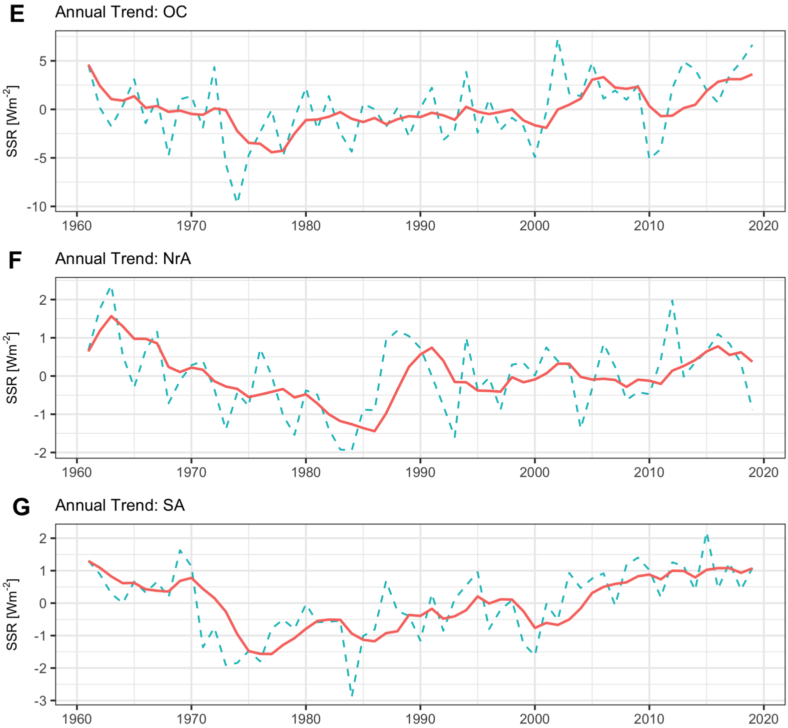

Fig. 2.5 Annual average anomalies over the period 1961-2019, part II. Refer to Figure 2.4 for the series legends. Subplots show results respectively for: E-Oceania, F-North America, G-South America. Refer to SI Figure A.9—Figure A.11 for the continents' monthly anomaly figures.

change for each continent separately. Breakpoints were detected based on moving sums (MOSUMS) of recursive and least-squares residuals for annual mean values which, despite of losing monthly temporal details, enables an investigation of interannual variation and time series segments (Forkel et al., 2013). Time series segment and structural change detection is widely used in climate research (e.g., Cró and Martins, 2017; Adedoyin et al., 2020; Vu et al., 2019). Readers are referred to Holben (1986) and Bai and Perron (1998, 2003) for the detailed implementation of the algorithm.

Any breakpoints with the Mann-Kendall trend test significant at 5% are identified and trends over the separated segments are reported in Table 2.4. Asia and North America, with decadal linear trends being -3.07 and -1.06 Wm^{-2}/dec, respectively, are the two largest contributors to the global dimming;

whereas the global brightening is mostly attributed to the increasing trends in Africa, Europe, and Oceania. Overall, with the exception of the stagnated trends in Africa for the past decade, continents show either a trend transition from negative to neutral/positive (Asia, North America, and Oceania) or a trend strengthening from less positive to more positive (Europe, and South America). It is worth noting that except for Africa that has two breakpoints (1973 and 2010), only one breakpoint is detected for other continents. In what follows, this paper will investigate more thoroughly on periods after the latest detected breakpoints. However, since the lastest breakpoint (2010) in Africa is rather recent and the period after that might not be long enough to consider its long-term trends, we will focus on the period after 1973 when Africa is referred to.

Given the large variability of SSR, the linear trends could be affected significantly by the different choices of start and end time. To avoid this bias, a running-trend estimation was implemented on the annual global average series for all possible segments equal or longer than 10 years. The global decadal trend raster (Figure 2.6) corroborates the annual anomaly series (Figure 2.4A). The most negative trends are found between 1965 and 1970 (referring to the start points), in contrast to the most positive trends over 1990-2000. After entering into the 21st century, the trends fade away. The continental running-trend rasters (Figure 2.7) show that Europe, Africa, and South America are dominated by positive trends, in contrary to Asia which is dominated by negative trends. The largest variation occurs in Oceania, where the trends span from the most negative $-5\ Wm^{-2}/dec$ in the mid 1960s to the most positive 5 Wm^{-2}/dec around the mid 1990s and the early 2010s.

The results shed light on how SSR trends evolve over time; nevertheless, because the data are aggregated over areas, either globally or continentally, opposite trends cancel each other out when calculating the areal averages, resulting in less distinct trends overall. Therefore also the regional distribution of trends as resolved by the 0.5 by 0.5 degree has been investigated. In what follows, interannual variabilities of annual and seasonal SSR for the globe and each continent are discussed based on their latest detected breakpoints

Table 2.4 Decadal linear trends for annual average SSR. After significant breakpoints are detected, the linear trend of the continental average time series is estimated by least-squares for each segment. The first row for each continent or the world shows the trend over the whole period; sub-periods split by the breakpoints are shown in the following rows. For instance, the global average trend shows a negative slope of $-0.15\ Wm^{-2}/dec$ over 1961-2019 and one breakpoint at 1984 is significantly detected. Split by 1984, a negative trend of $-1.54\ Wm^{-2}/dec$ is reported over the first segment and a positive trend of $+0.49\ Wm^{-2}/dec$ is reported over the latter segment.

Continent	Segment	Slope[a]	Slope std	t value	Pval	Pval.symbol[b]
World	1961-2019	-0.150	0.069	-2.185	0.033	*
	1961-1984	-1.535	0.117	-13.077	0.000	***
	1985-2019	0.486	0.071	6.892	0.000	***
Europe	1961-2019	0.500[c]	0.113	4.433	0.000	***
	1961-1976	0.921	0.701	1.313	0.210	
	1977-2019	1.010	0.161	6.258	0.000	***
Africa	1961-2019	0.760	0.072	10.520	0.000	***
	1961-1973	1.196	0.620	1.927	0.080	.
	1974-2010	1.319	0.122	10.850	0.000	***
	2011-2019	-0.564	0.679	-0.831	0.434	
Asia	1961-2019	-1.278	0.123	-10.406	0.000	***
	1961-1993	-3.074	0.112	-27.476	0.000	***
	1994-2019	-0.032	0.132	-0.244	0.810	
Oceania	1961-2019	0.638	0.244	2.614	0.011	*
	1961-1972	-0.573	2.382	-0.241	0.815	
	1973-2019	1.484	0.311	4.778	0.000	***
North America	1961-2019	0.015	0.072	0.202	0.840	
	1961-1986	-1.064	0.188	-5.667	0.000	***
	1987-2019	0.015	0.146	0.103	0.918	
South America	1961-2019	0.193	0.076	2.550	0.013	*
	1961-1970	0.284	0.611	0.466	0.654	
	1971-2019	0.547	0.072	7.568	0.000	***

[a] Slope unit: Wm^{-2} per decade.

[b] Significance symbol representation:
*** indicates $p < 0.001$, ** for $p < 0.01$, * for $p \leq 0.05$, . for $p \leq 0.1$, and no symbol if $p > 0.1$.

[c] The linear trend is smaller than in both segments due to the large jump in 1976 (refer to panel B in Figure 2.4).

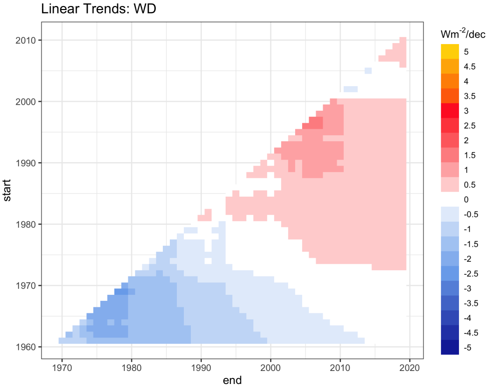

Fig. 2.6 Decadal trend raster for the global. The trends are estimated on global average SSR. The y-axis denotes the start years, and the x-axis denotes the end years.

respectively. Furthermore, the spatial distribution of the trends is visualized in annual and seasonal maps.

Latest sustainable Trend

Based on the structural breaks in trends, the latest sustainable trends, i.e., the period after the latest detected breakpoints, over the globe and each continent are inspected in this section. Their spatial and seasonal patterns are presented as trend maps for each season and the entire year. Seasons are defined as follows: winter (DJF: December-February), spring (MAM: March-May), summer (JJA: June-August), and autumn (SON: September-November). Seasonal trends after the detected breakpoints for the globe and each continent are reported in Table 2.5, which will be elaborated in the sections in what follows.

World

The global brightening starts from 1984 and continues onwards, at a moderate rate of $+0.49\ Wm^{-2}/dec$, only about one-third of the dimming rate before ($-1.54\ Wm^{-2}/dec$). Although the global average SSR has shown a positive trend since 1985, on a regional level, significant dimming is observed in certain regions, in particular eastern US, South Asia, and the Pacific island countries (Figure 2.8A). Generally, the majority of the globe has shown positive trends since 1985. Two centroids of the most positive trends globally are observed in Tibet, China, and Riyadh, Saudi Arabia, with decadal trends between 5 to 6 Wm^{-2} per decade.

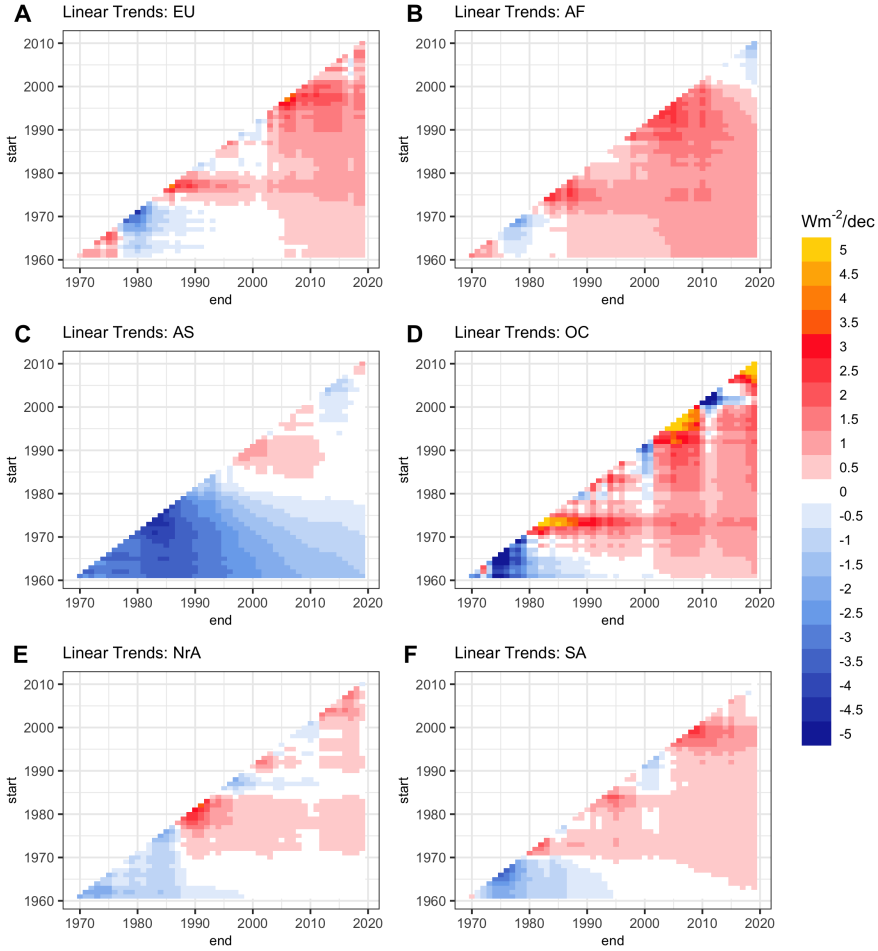

Fig. 2.7 Decadal trend rasters for continents.

The seasonal maps show that the northern hemisphere spring and summer show the largest trend variability (Figure 2.8C-D), that is, during which both the strongest positive and negative trends take place. On the other hand, northern hemispheric winter shows the modest trends, both positive and negative trends are diminished as expected due to the lower absolute SSR values in northern hemispheric winter in the extratropics. Note that the decadal trends are squeezed into a range of $-7 \sim 7\ Wm^{-2}$ per decade, namely, any extreme values falling out of the range are assigned as -7 if a value is smaller than -7 , and 7 if a value

Table 2.5 Decadal linear trends for seasonal average SSR over the period from the detected breakpoints until 2019.

Continent	Seasons	Slope[a]	Slope Std	t value	Pval	Pval.symbol[b]
World (1985-)	DJF	0.352	0.106	3.306	0.002	**
	MAM	0.609	0.120	5.087	0.000	***
	JJA	0.468	0.115	4.071	0.000	***
	SON	0.513	0.131	3.900	0.000	***
Europe (1977-)	DJF	-0.136	0.114	-1.192	0.240	
	MAM	1.318	0.333	3.956	0.000	***
	JJA	2.265	0.388	5.839	0.000	***
	SON	0.605	0.226	2.673	0.011	*
Africa (1974-)	DJF	1.031	0.177	5.838	0.000	***
	MAM	1.218	0.151	8.086	0.000	***
	JJA	0.671	0.109	6.179	0.000	***
	SON	1.038	0.129	8.047	0.000	***
Asia (1994-)	DJF	0.025	0.233	0.106	0.916	
	MAM	0.439	0.257	1.711	0.100	
	JJA	-0.273	0.261	-1.048	0.305	
	SON	-0.380	0.290	-1.312	0.202	
Oceania (1973-)	DJF	1.128	0.593	1.902	0.064	.
	MAM	1.470	0.612	2.402	0.020	*
	JJA	1.305	0.441	2.961	0.005	**
	SON	1.801	0.485	3.712	0.001	***
North America (1987-)	DJF	0.097	0.238	0.406	0.687	
	MAM	-0.375	0.250	-1.500	0.144	
	JJA	0.055	0.251	0.220	0.828	
	SON	0.304	0.313	0.972	0.339	
South America (1971-)	DJF	0.370	0.094	3.948	0.000	***
	MAM	0.480	0.134	3.574	0.001	***
	JJA	0.730	0.131	5.577	0.000	***
	SON	0.582	0.093	6.276	0.000	***

[a] Slope unit: Wm^{-2} per decade.

[b] Significance symbol representation: refer to Table 2.4

is larger than 7[2]. More specifically, we observe that the positive trends over

---

[2] The 99% percentile of seasonal trends in JJA is 7.08 Wm^{-2} per decade, therefore, about 1% values larger than that are forced to be 7. As we will see in the forthcoming result (Figure 2.15), the

Tibet and Riyadh are mostly attributed to high rates in northern hemispheric spring and summer. Also noteworthy is that the dimming trends are observed throughout the year in India, with the most negative trends observed in summer. For the southern hemisphere the strongest trends are observed in winter (JJA) and spring (SON), showing widespread positive trends in general.

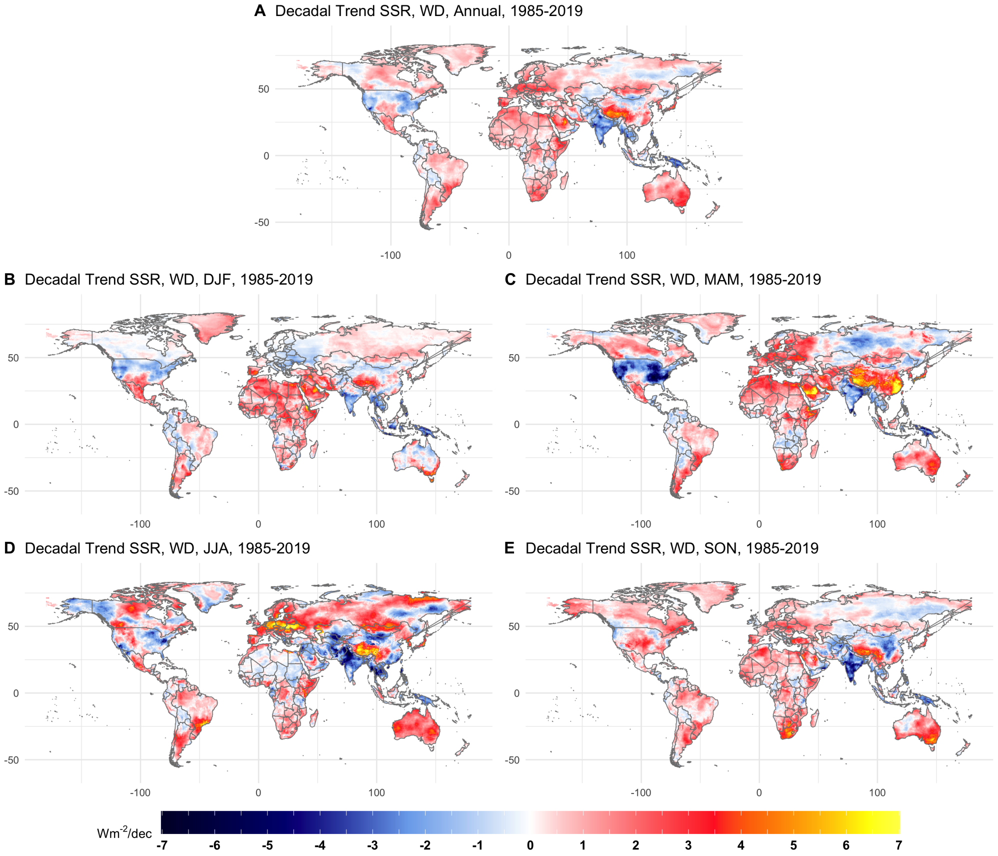

Fig. 2.8 Linear trends of the annual and seasonal average SSR over the globe during the period 1985-2019 (after the breakpoint at 1984). The values are estimated for each 0.5 × 0.5 degree grid and expressed as Wm^{-2} per decade. Panel A shows the decadal trends for annual average SSR. Panel B-E show the decadal trends for individual seasons. The seasons are defined as spring (MAM, dated from Mar. to May.), summer (JJA, dated from Jun. to Aug.), autumn (SON, dated from Sep. to Nov.), and winter (DJF, dated according to the year in which Jan. and Feb. belong to, plus Dec. from the previous year).

---

largest concentration of the trends falls within $[-4, 4]$ Wm^{-2}, i.e., the upper and lower 1.5 standard deviation from the mean, making it reasonable to visualize values in a truncated range of $[-7, 7]$ Wm^{-2} per decade to better see the small absolute values.

Europe

The recent long-term trends in Europe show an increase of average SSR at the rate of 1.01 Wm^{-2}/dec starting from 1977 and up until now (Table 2.4). At a seasonal scale, except for winter, all the other seasons show significant positive average trends, with summer having the strongest rate at 2.27 Wm^{-2}/dec (Table 2.5).

The spatial distribution in the annual mean shows a widespread increase with the most positive area located in the Central European Domain (CED) (Figure 2.9A), defined as land areas from $45°N$ to $55°N$ and $10°W$ and $35°E$, namely in Germany, southern Poland, Slovakia, and Ukraine. The mean annual trend for the CED is 1.81 Wm^{-2}/dec, which is about 0.80 Wm^{-2}/dec higher than the annual trend over the whole continent. In fact, a larger difference, 2.02 Wm^{-2}/dec (4.11 and 2.09 Wm^{-2}/dec for decadal trends over CED and the whole EU land area, respectively), is observed if only summer (JJA) is considered. The spatial pattern is also found by Sanchez-Lorenzo et al. (2017), who reported higher rates of annual and seasonal SSR for the CED as compared to the entire continent. In particular, they documented a 1.0 Wm^{-2} per decade higher rate for the CED as compared to the whole continent for the annual series over the period 1983-2010, in contrast to a larger difference of 2.2 Wm^{-2}/dec for the summer counterpart. It is worth noting that in summer, the trends in the Mediterranean area are actually negative, in contrary to the general positive trends over the rest of the continent. In particular, the Mediterranean area shows negative trends throughout the year except spring. The negative trends are also reported in Sanchez-Lorenzo et al. (2017). Furthermore, our study shows no significant European-average trends in winter; however, at a regional level, CED shows slightly negative trends, and also noteworthy are the positive trends observed in Spain and France. The continuous increase in the winter series in Spain is also reported by Sanchez-Lorenzo et al. (2013).

Africa

Our results show that Africa exhibits a widespread increase in SSR, especially from the 1970s to 2000s, during which the continent average SSR increases at 1.32 Wm^{-2}/dec (Table 2.4, Figure 2.4C). Entering into the 2010s, the brightening trends tend to cease and no significant trends are observed. Central Africa

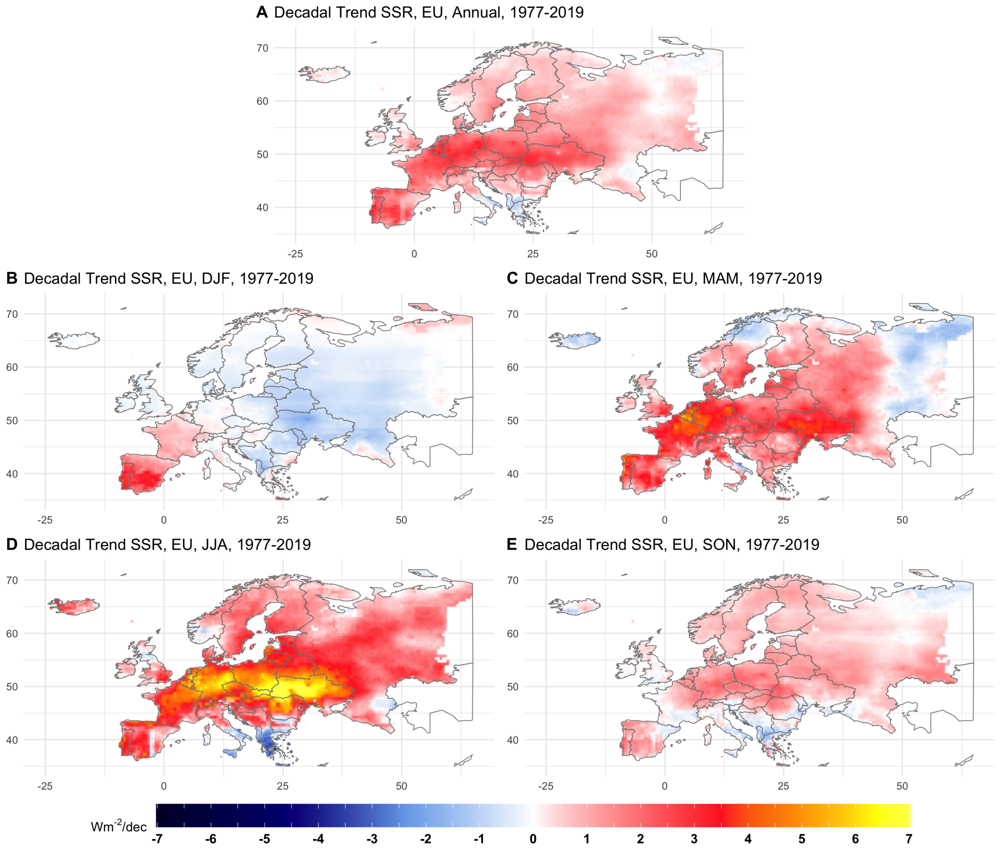

Fig. 2.9 Linear trends of the annual and seasonal average SSR in Europe during the period 1977-2019.

$(20^\circ S \sim 20^\circ N)$ exhibits generally weaker annual mean trends ($0.84\ Wm^{-2}/dec$) as compared to the areas in the two ends (Figure 2.10A). The mean decadal trends for annual average SSR are 1.19 and 1.54 Wm^{-2}/dec for northern and southern Africa, respectively. This is consistent with the spatial pattern reported by Soares et al. (2019).

On the seasonal basis, all seasons show positive average trends, with the strongest rate found in northern hemispheric spring at 1.22 Wm^{-2} per decade (Figure 2.10B-E, Table 2.5). The weakest trends are found in northern hemispheric summer, during which equator areas show strong positive trends while Sahara area shows neutral trends.

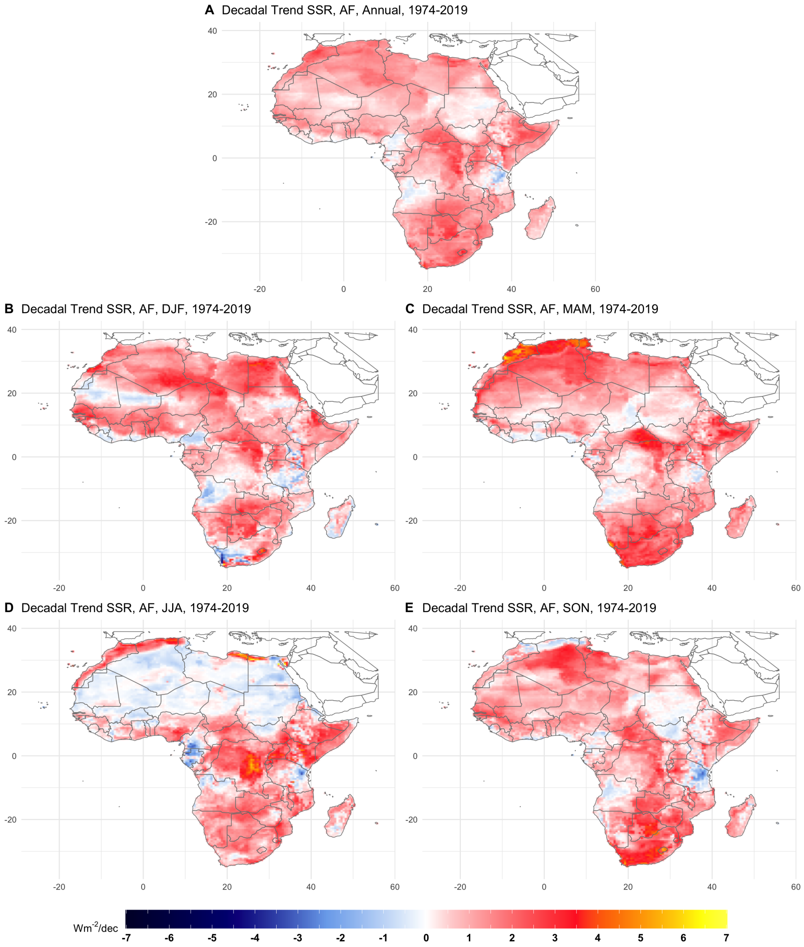

Fig. 2.10 Linear trends of the annual and seasonal average SSR in Africa during the period 1974-2019.

Asia

Large spatial variability is observed in Asia. Even though extremely strong trends exist, the opposite signs neutralize each other, resulting in insignificance in continental average trends after 1993 (Table 2.4, Figure 2.4D). On the regional level (Figure 2.11A), considerably negative trends are observed in India and Southeast Asia (consisting of countries south of China and the Pacific island countries), in contrast to the highly positive trends in the Middle East countries, Tibet, middle east of Russia, and the areas surrounding the Sea of Japan.

Generally, the negative trends over India and Southeast Asia persist throughout the year, with the most negative trends observed in summer.

On the continental scale, the most negative trends take place in autumn, with a value of $-0.38\,Wm^{-2}/dec$, while summer shows a weaker negative trend at $-0.27\,Wm^{-2}/dec$ (Table 2.5). Winter and spring show slightly positive continental average trends. Nevertheless, none of the seasonal as well as the annual continental trends are significant due to the substantial variability within the continent. The nonsignificant trends corroborate the findings by Yang et al. (2018), who indicated that the trend reversal, or jump, in the early 1990s in China is exaggerated falsely because of instrument and operational changes. A series of procedures were performed by Yang et al. to obtain a homogenized series, and based on which, they concluded that no significant trends are found in China over the period 1990-2016. Moreover, the interpolated dataset of the current paper mitigates the jump reported in the original observations by Moseid et al. (2020). This highlights that our constructed dataset functions as an adjustment to the raw observations toward a homogeneous dataset.

On a seasonal basis, two centroids of strong positive trends are identified in east China and middle Saudi Arabia in spring. In the southeastern China, trends vary largely among the seasons, more specifically, significant negative ones in autumn and winter, and substantial positive ones in spring and summer (Figure 2.11B-E).

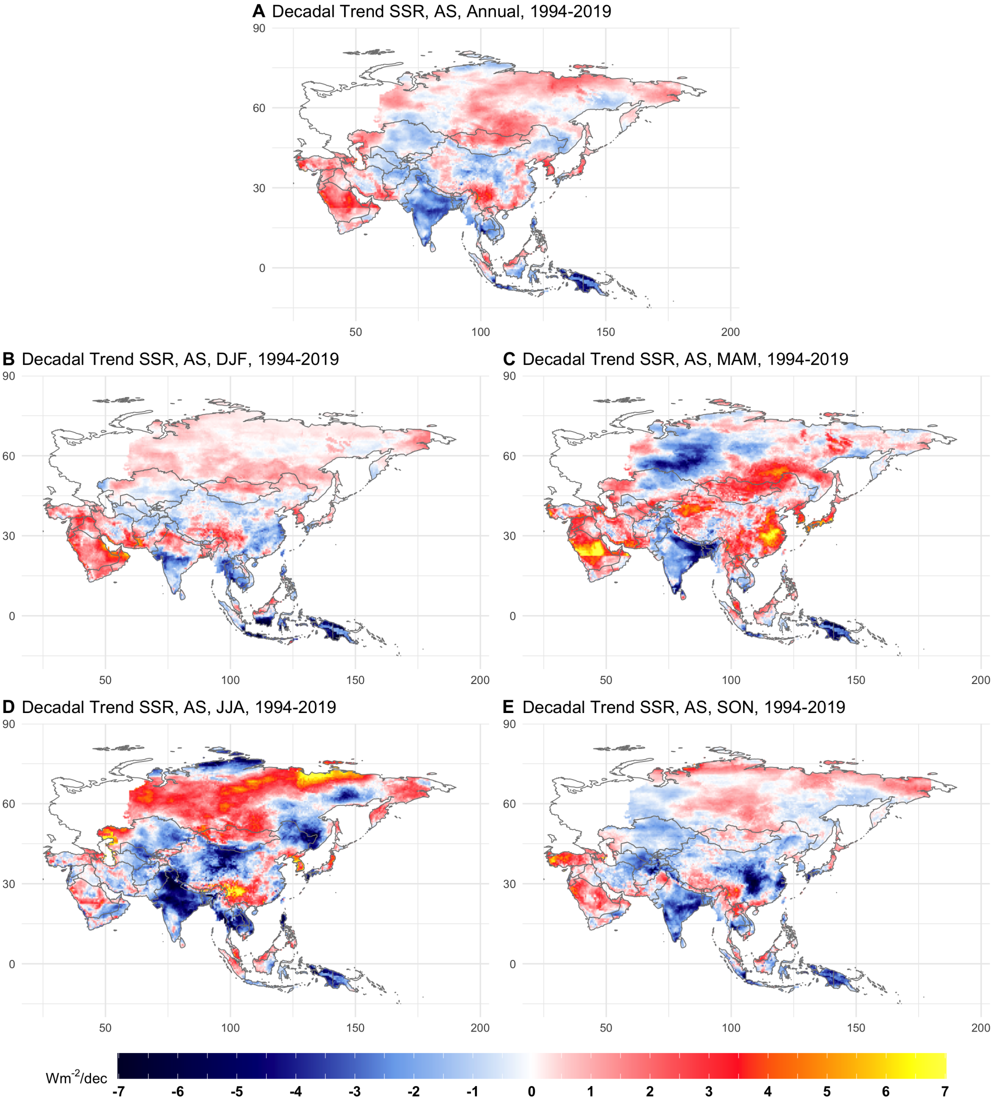

Fig. 2.11 Linear trends of the annual and seasonal average SSR in Asia during the period 1994-2019.

Oceania

Caution needs to be taken for users to interpret the historic SSR trends in Oceania prior to 1988: the original data in Australia have been artificially detrended, as the Metservice there was afraid that the instruments were drifting.

Therefore, the trends prior to 1988 (Figure 2.5E) might be flatter than they are supposed to be in reality.

The latest sustainable SSR annual mean trend over Oceania is 1.48 Wm^{-2}/dec starting from 1973, which is the strongest among all continents (Table 2.4, Figure 2.5E). The continent shows high extent of homogeneity (Figure 2.12). In particular, unanimous positive annual average trends are observed in Australia, with the west coast being more positive than the east coast. New Zealand shows a tendency of neutral trends. The seasonal maps show highly consistent positive trends; specifically, all seasons show positive continental average trends. The only neutral regional trends are found in the west-south coastline in summer (DJF). On a seasonal basis, the strongest continental average trend is found in spring (SON) at 1.80 Wm^{-2}/dec and the weakest continental average trend is found in summer (DJF) at 1.13 Wm^{-2}/dec (Table 2.5).

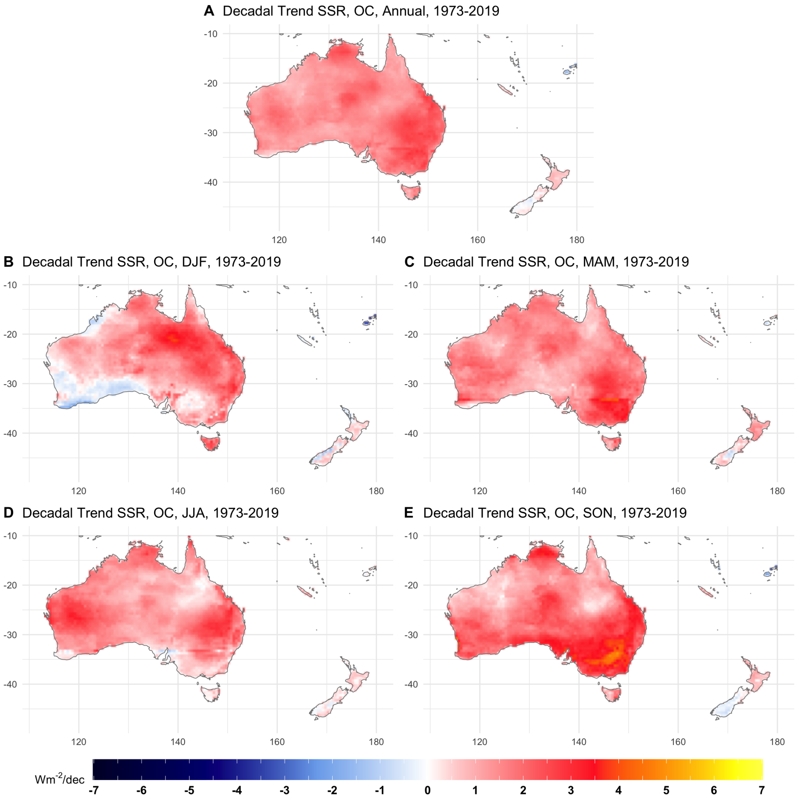

Fig. 2.12 Linear trends of the annual and seasonal average SSR in Ocean during the period 1973-2019.

North America

North America has highly diverging trends; similar to Asia, both strong positive and negative trends are observed over the period 1987-2019, resulting in the overall neutral continental average trends (Table 2.5, Figure 2.5F). Significant negative trends are observed in the eastern US in spring (Figure 2.13C). The majority of the mainland US shows generally negative trends throughout the year, except for the west-middle areas which show an increase in summer. Canada shows a tendency of positive or neutral trends throughout the year over most areas excluding the part bordering with Alaska in summer. Additionally, positive trends are also observed in Greenland and Mexico. On a seasonal basis, spring and summer show strong regional trends and winter shows the weakest trends.

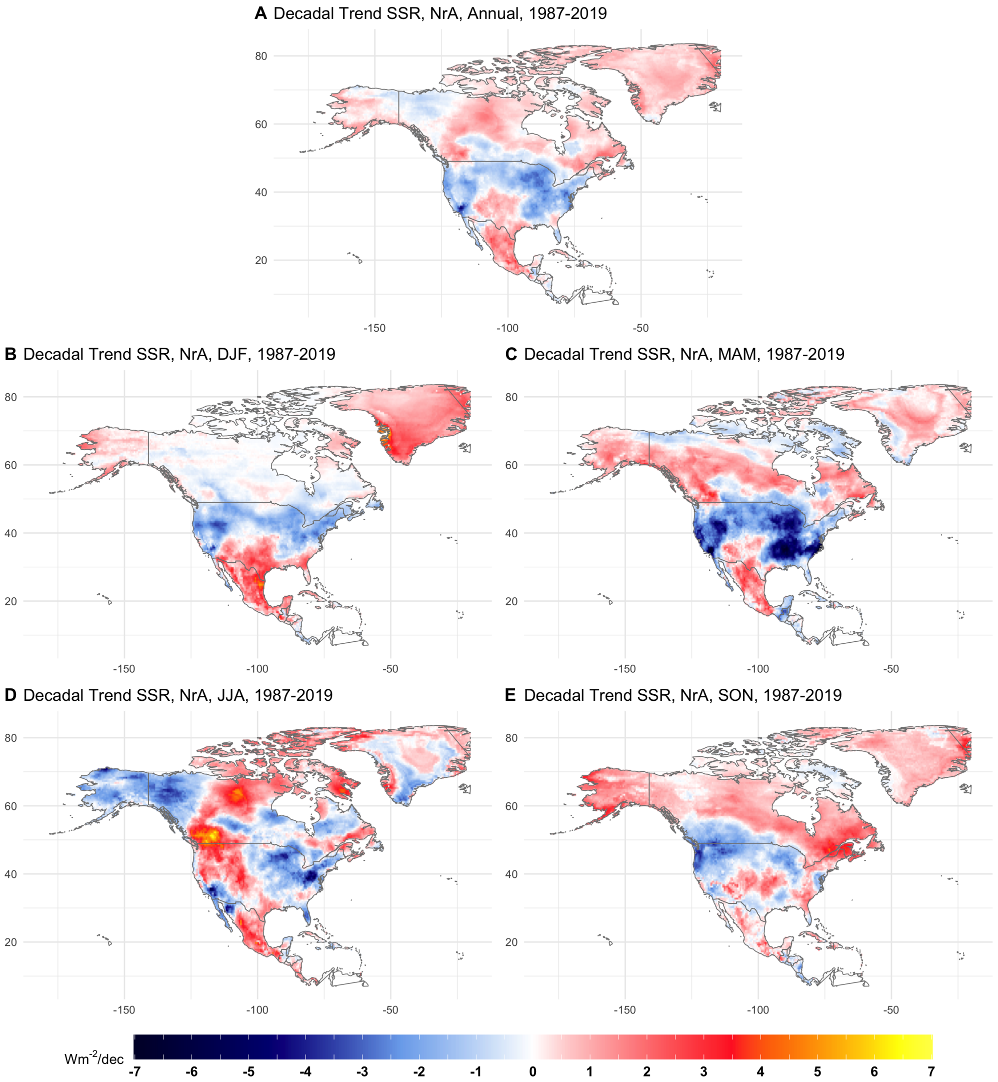

Fig. 2.13 Linear trends of the annual and seasonal average SSR in North America during the period 1987-2019.

South America

South America shows a significant and widespread increase in SSR after 1971 at an annual rate of 0.55 Wm^{-2}/dec (Table 2.4, Figure 2.5G). The annual average SSR trends are stronger in south (Figure 2.14A); especially in the southern region beyond $30°S$, the annual continental trend of which is 0.60

Wm^{-2}/dec. Specifically, separated by $30°S$, the southern region and northern region show a tendency of increase at rates 1.06 and 0.46 Wm^{-2} per decade, respectively. On the seasonal scale, all seasons show significant increases, with winter (JJA) having the strongest continental average trend at 0.73 Wm^{-2}/dec, and summer (DJF) showing the weakest trend at 0.37 Wm^{-2} per decade (Table 2.5). The spatial distribution shows high degree of consistency among seasons.

2.4 Discussion

This study interpolates a ground-based solar radiation observation dataset and constructs a dataset with complete global land coverage at high resolution covering nearly six decades. This enables a temporal and spatial trend analysis at the continental and the regional level, making possible for the data scarce continents, e.g. Africa, to obtain a comprehensive quantification of the long-term trends. Rather than relying principally on graphic visualization, a structural breakpoint detection algorithm based on moving sums (MOSUMS test) is applied and provides quantitative identification of any structural changes in long-term series. The results show that the global dimming-brightening transition takes place around 1984, in line with existing literature based on station observations. The two divided segments show a decrease and an increase at -1.54 Wm^{-2} and $+0.49$ Wm^{-2} per decade, respectively. However, it is worth noting that on the continental level, four out of six continents, i.e., Europe, Africa, Oceania, and South America, actually show no significant decreasing trends over the entire period 1961-2019. In particular, they generally show a transition from no significant trends to positive trends (Europe, Oceania, and South America), or experience a positive trend strengthening (Africa). Therefore, it is obvious that the global dimming is attributed to the substantial reduction of SSR in Asia and North America, which show reduction rates at -3.07 Wm^{-2}/dec and -1.06 Wm^{-2}/dec, respectively.

Over the brightening period (1985-2019), considerable spatial diversity is observed. In particular, two positive centroids are Riyadh, Saudi Arabia and Tibet, China; substantial decreasing trends are observed in the eastern US, South Asia, and the Pacific Island countries. Compared to the large spatial

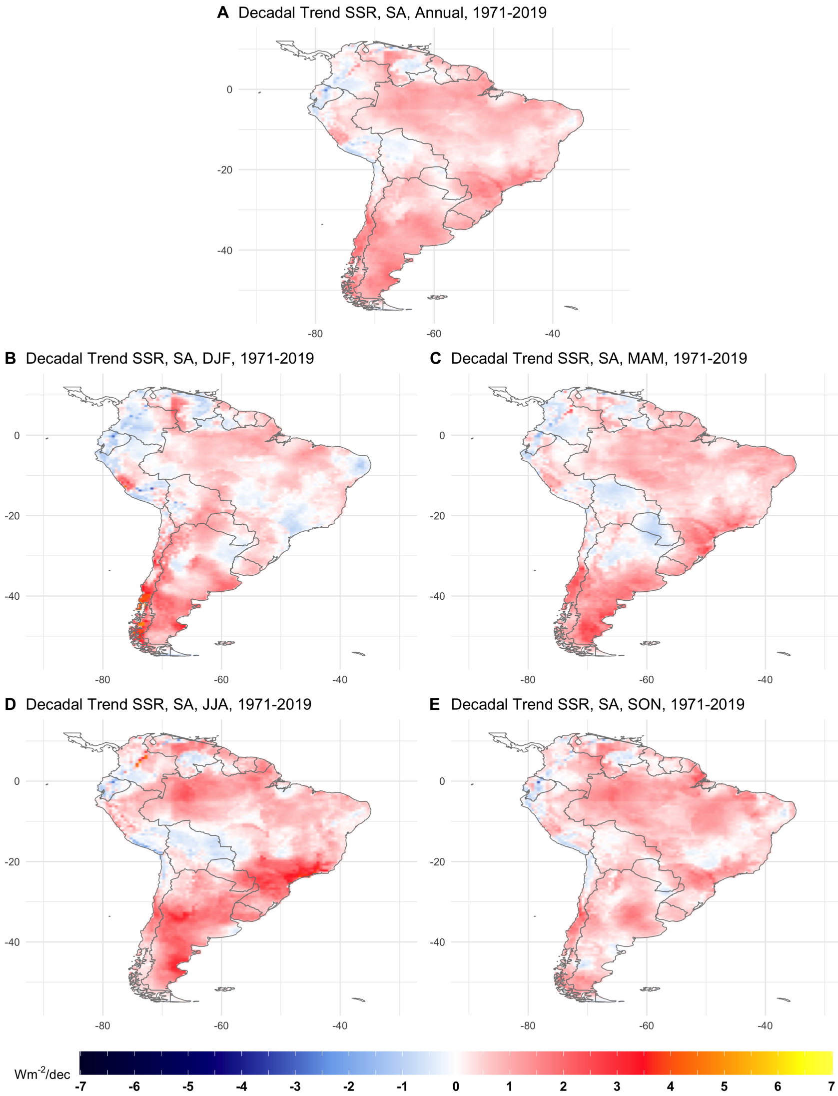

Fig. 2.14 Linear trends of the annual and seasonal average SSR in South America during the period 1971-2019.

variability in the northern hemisphere, the southern hemisphere, on the other hand, shows a consistent widespread increase.

In order to obtain an overview of the distribution of decadal trends for each gridbox within a continent, Figure 2.15 shows a box plot for annual trends as well as for each seasonal trends for all gridboxes per continent. A longer box and a longer distance between whiskers indicate larger variability and more heterogeneity among gridboxes in a continent. We observe that most boxes are generally symmetric, that means the distribution is approximately normal. However, there exist certain boxes which are asymmetric and show skewness. For instance, the fact that the median is closer to the lower hinge shows that the winter box in North America is right skewed. In other words, the majority of trends for gridboxes are of small values, but the average trend of all gridboxes is shifted toward a larger value by certain gridboxes with strong trends. The box plots also indicate that northern hemisphere continents, i.e., Asia, North America, and Europe, show larger variability than southern hemisphere continents, which can be concluded from their wider ranges between upper and lower whisker. On a seasonal basis, the largest variability generally exists in summer, and the smallest variability exists in winter. The decadal variability for individual seasons varies largely among the continents. Specifically, box plots for South America, Africa, and Oceania are more truncated and more consistent among various seasons. In other words, decadal variabilities in southern hemisphere continents are at approximately the same level among all seasons.

The intra-annual variability is largely determined by clouds, but the longer term (decadal) variabilities are often more governed by aerosol changes (Wild, 2016; Boers et al., 2017; Pfeifroth et al., 2018). Wild et al. (2021) reported that the major cause of the brightening in Europe, especially in the Central Europe Domain, is highly affected by the aerosol effects through a reduction in anthropogenic aerosol emissions after the 1980s. Moreover, Sanchez-Lorenzo et al. (2017) found that seasonal variability of solar radiation trends in Europe is closely related to changes in cloud coverage. For example, the high rates of brightening in spring are accompanied with large rates of decrease in cloud cover; however, the strong trends in summer are less substantiated by cloud cover changes, which, in fact, demonstrate slightly positive trends. Based on the reported evidence, we speculate that the profound positive summer trends in Europe could be due to the reduction of pollution aerosols in summer (Panel EU in Figure 2.15).

This study provides an observation based dataset with complete spatial and temporal coverage. It completes the global surface solar radiation trend analysis by analyzing continents which are rarely examined before. The quantification of long-term trends is of significant importance to solar energy deployment (Müller et al., 2014). Last but not least, this study has the potential to be used for comparison with climate model simulations. It could serve as a benchmark reference to the evaluation and calibration for global or regional climate models. Other potential applications could be climate change monitoring and a strengthened understanding of its closely related atmospheric or hydrological processes, for instance, temperature changes, aerosol dispersion, etc.

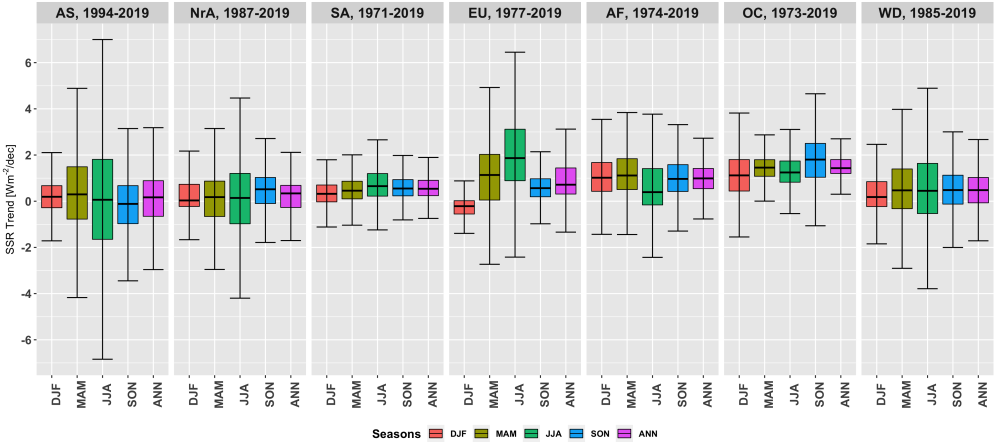

Fig. 2.15 Box plot for seasonal and annual SSR Trends. The box plots are statistics calculated based on trends at all individual gridboxes for each continent over the period after the last corresponding breakpoint and up until 2019. Five values are shown for each box plot from bottom to top: lower whisker, first quartile (Q_1), median (Q_2), third quartile (Q_3), and upper whisker. The upper whisker is defined as either the maximum value or, if smaller, as the third quartile plus 1.5 times the interquartile range ($IQR = Q_3 - Q_1$); equally, the lower whisker is defined as the the minimum value or, if larger, as the first quartile minus the 1.5 times interquartile range. Continent panels are aligned ascendingly by the median of annual SSR trends from the left to the right, together with the world plot at the end. Four seasons (DJF, MAM, JJA, SON) and annual (ANN) trends are shown for each continent.

References

Adedoyin, F., Ozturk, I., Abubakar, I., Kumeka, T., Folarin, O., and Bekun, F. V. (2020). Structural breaks in CO2 emissions: Are they caused by climate change protests or other factors? *Journal of Environmental Management*, 266:110628.

Arking, A. (1996). Absorption of solar energy in the atmosphere: Discrepancy between model and observations. *Science*, 273(5276):779–782.

Bai, J. and Perron, P. (1998). Estimating and Testing Linear Models with Multiple Structural Changes. *Econometrica*, 66(1):47.

Bai, J. and Perron, P. (2003). Computation and analysis of multiple structural change models. *Journal of Applied Econometrics*, 18(1):1–22.

Boers, R., Brandsma, T., and Siebesma, A. P. (2017). Impact of aerosols and clouds on decadal trends in all-sky solar radiation over the Netherlands (1966–2015). *Atmospheric Chemistry and Physics*, 17(13):8081–8100.

Breiman, L. (2001). Random forests. Machine Learning. 45:5–32.

Budyko, M. I. (1969). The effect of solar radiation variations on the climate of the Earth. *Tellus*, 21(5):611–619.

Cherian, R., Quaas, J., Salzmann, M., and Wild, M. (2014). Pollution trends over Europe constrain global aerosol forcing as simulated by climate models. *Geophysical Research Letters*, 41(6):2176–2181.

CIESIN (2004). Global rural–urban mapping project (grump), alpha version: urban extents grids.

Collins, F. C. (1995). *A comparison of spatial interpolation techniques in temperature estimation*. PhD thesis, Virginia Tech.

Cró, S. and Martins, A. M. (2017). Structural breaks in international tourism demand: Are they caused by crises or disasters? *Tourism Management*, 63:3–9.

Erxleben, J., Elder, K., and Davis, R. (2002). Comparison of spatial interpolation methods for estimating snow distribution in the Colorado Rocky Mountains. *Hydrological Processes*, 16(18):3627–3649.

Firth, L., Hazelton, M. L., and Campbell, E. P. (2005). Predicting the onset of Australian winter rainfall by nonlinear classification. *Journal of Climate*, 18(6):772–781.

Forkel, M., Carvalhais, N., Verbesselt, J., Mahecha, M., Neigh, C., and Reichstein, M. (2013). Trend Change Detection in NDVI Time Series: Effects of Inter-Annual Variability and Methodology. *Remote Sensing*, 5(5):2113–2144.

Gilgen, H., Roesch, A., Wild, M., and Ohmura, A. (2009). Decadal changes in shortwave irradiance at the surface in the period from 1960 to 2000 estimated from Global Energy Balance Archive Data. *Journal of Geophysical Research*, 114(8):D00D08.

Greenwald, R., Bergin, M. H., Xu, J., Cohan, D., Hoogenboom, G., and Chameides, W. L. (2006). The influence of aerosols on crop production: A study using the CERES crop model. *Agricultural Systems*, 89(2):390–413.

Gupta, R., Somanathan, E., and Dey, S. (2017). Global warming and local air pollution have reduced wheat yields in India. *Climatic Change*, 140(3-4):593–604.

Harris, I., Osborn, T. J., Jones, P., and Lister, D. (2020). Version 4 of the CRU TS monthly high-resolution gridded multivariate climate dataset. *Scientific Data*, 7(1).

He, Y., Wang, K., Zhou, C., and Wild, M. (2018). A Revisit of Global Dimming and Brightening Based on the Sunshine Duration. *Geophysical Research Letters*, 45(9):4281–4289.

Holben, B. N. (1986). Characteristics of maximum-value composite images from temporal AVHRR data. *International Journal of Remote Sensing*, 7(11):1417–1434.

Jiang, Y. (2008). Prediction of monthly mean daily diffuse solar radiation using artificial neural networks and comparison with other empirical models. *Energy Policy*, 36(10):3833–3837.

Leirvik, T. and Yuan, M. (2020). A machine learning technique for spatial interpolation of solar radiation observations. *Earth and Space Science Open Archive*, page 30.

Moseid, K. O., Schulz, M., Storelvmo, T., Julsrud, I. R., Olivié, D., Nabat, P., Wild, M., Cole, J., and Takemura, T. (2020). Bias in CMIP6 models compared to observed regional dimming and brightening trends (1961–2014). *Atmospheric Chemistry and Physics*, pages 1–20.

Müller, B., Wild, M., Driesse, A., and Behrens, K. (2014). Rethinking solar resource assessments in the context of global dimming and brightening. *Solar Energy*, 99:272–282.

Myoung, B., Rhee, J., and Yoo, C. (2020). Long-Lead Predictions of Warm Season Droughts in South Korea Using North Atlantic SST. *Journal of Climate*, 33(11):4659–4677.

Nabat, P., Somot, S., Mallet, M., Sanchez-Lorenzo, A., and Wild, M. (2014). Contribution of anthropogenic sulfate aerosols to the changing Euro-Mediterranean climate since 1980. *Geophysical Research Letters*, 41(15):5605–5611.

NESDIS (1995). TerrainBase, Global 5 Arc-minute Ocean Depth and Land Elevation from the US National Geophysical Data Center (NGDC).

Obryk, M. K., Fountain, A. G., Doran, P. T., Lyons, W. B., and Eastman, R. (2018). Drivers of solar radiation variability in the McMurdo Dry Valleys, Antarctica. *Scientific Reports*, 8(1):5002.

Ohmura, A. and Gilgen, H. (1993). Re-Evaluation of the Global Energy Balance. pages 93–110. American Geophysical Union (AGU).

Pfeifroth, U., Sanchez-Lorenzo, A., Manara, V., Trentmann, J., and Hollmann, R. (2018). Trends and Variability of Surface Solar Radiation in Europe Based On Surface- and Satellite-Based Data Records. *Journal of Geophysical Research: Atmospheres*, 123(3):1735–1754.

Phillips, P. C., Leirvik, T., and Storelvmo, T. (2020). Econometric estimates of Earth's transient climate sensitivity. *Journal of Econometrics*, 214(1):6–32.

Proctor, J., Hsiang, S., Burney, J., Burke, M., and Schlenker, W. (2018). Estimating global agricultural effects of geoengineering using volcanic eruptions. *Nature*, 560(7719):480–483.

Qin, W., Wang, L., Zhang, M., Niu, Z., Luo, M., Lin, A., and Hu, B. (2019). First effort at constructing a high-density photosynthetically active radiation dataset during 1961-2014 in China. *Journal of Climate*, 32(10):2761–2780.

Roderick, M. L. and Farquhar, G. D. (2012). Geoengineering: Hazy, cool and well fed?

Sanchez-Lorenzo, A., Calbó, J., and Wild, M. (2013). Global and diffuse solar radiation in Spain: Building a homogeneous dataset and assessing their trends. *Global and Planetary Change*, 100:343–352.

Sanchez-Lorenzo, A., Enriquez-Alonso, A., Wild, M., Trentmann, J., Vicente-Serrano, S. M., Sanchez-Romero, A., Posselt, R., and Hakuba, M. Z. (2017). Trends in downward surface solar radiation from satellites and ground observations over Europe during 1983–2010. *Remote Sensing of Environment*, 189:108–117.

Sanchez-Lorenzo, A., Wild, M., Brunetti, M., Guijarro, J. A., Hakuba, M. Z., Calbó, J., Mystakidis, S., and Bartok, B. (2015). Reassessment and update of long-term trends in downward surface shortwave radiation over Europe (1939-2012). *Journal of Geophysical Research*, 120(18):9555–9569.

Scudiero, E., Corwin, D. L., Morari, F., Anderson, R. G., and Skaggs, T. H. (2016). Spatial interpolation quality assessment for soil sensor transect datasets. *Computers and Electronics in Agriculture*, 123:74–79.

Soares, P. M., Brito, M. C., and Careto, J. A. (2019). Persistence of the high solar potential in Africa in a changing climate. *Environmental Research Letters*, 14(12):124036.

Storelvmo, T., Leirvik, T., Lohmann, U., Phillips, P. C. B., and Wild, M. (2016). Disentangling greenhouse warming and aerosol cooling to reveal Earth8217;s climate sensitivity. *Nature Geoscience*, 9:286–289.

Sun, H., Gui, D., Yan, B., Liu, Y., Liao, W., Zhu, Y., Lu, C., and Zhao, N. (2016). Assessing the potential of random forest method for estimating solar radiation using air pollution index. *Energy Conversion and Management*, 119:121 – 129.

Vu, T. T., Kiesel, J., Guse, B., and Fohrer, N. (2019). Analysis of the occurrence, robustness and characteristics of abrupt changes in streamflow time series under future climate change. *Climate Risk Management*, 26:100198.

Wang, K., Ma, Q., Wang, X., and Wild, M. (2014). Urban impacts on mean and trend of surface incident solar radiation. *Geophysical Research Letters*, 41(13):4664–4668.

Wild, M. (2009). Global dimming and brightening: A review. *Journal of Geophysical Research*, 114(D10):D00D16.

Wild, M. (2012). Enlightening Global Dimming and Brightening. *Bulletin of the American Meteorological Society*, 93(1):27–37.

Wild, M. (2016). Decadal changes in radiative fluxes at land and ocean surfaces and their relevance for global warming. *Wiley Interdisciplinary Reviews: Climate Change*, 7(1):91–107.

Wild, M., Gilgen, H., Roesch, A., Ohmura, A., Long, C. N., Dutton, E. C., Forgan, B., Kallis, A., Russak, V., and Tsvetkov, A. (2005). From dimming to brightening: Decadal changes in solar radiation at earth's surface. *Science*, 308(5723):847–850.

Wild, M., Grieser, J., and Schär, C. (2008). Combined surface solar brightening and increasing greenhouse effect support recent intensification of the global land-based hydrological cycle. *Geophysical Research Letters*, 35(17).

Wild, M. and Liepert, B. (2010). The Earth radiation balance as driver of the global hydrological cycle.

Wild, M., Ohmura, A., Schär, C., Müller, G., Folini, D., Schwarz, M., Zyta Hakuba, M., and Sanchez-Lorenzo, A. (2017). The Global Energy Balance Archive (GEBA) version 2017: A database for worldwide measured surface energy fluxes. *Earth System Science Data*, 9(2):601–613.

Wild, M., Wacker, S., Yang, S., and Sanchez-Lorenzo, A. (2021). Evidence for Clear-sky Dimming and Brightening in Central Europe. *Geophysical Research Letters*, page e2020GL092216.

Xu, T., Guo, Z., Liu, S., He, X., Meng, Y., Xu, Z., Xia, Y., Xiao, J., Zhang, Y., Ma, Y., and Song, L. (2018). Evaluating Different Machine Learning Methods for Upscaling Evapotranspiration from Flux Towers to the Regional Scale. *Journal of Geophysical Research: Atmospheres*, 123(16):8674–8690.

Yang, S., Wang, X. L., and Wild, M. (2018). Homogenization and trend analysis of the 1958-2016 in situ surface solar radiation records in China. *Journal of Climate*, 31(11):4529–4541.

Zhou, Q., Flores, A., Glenn, N. F., Walters, R., and Han, B. (2017). A machine learning approach to estimation of downward solar radiation from satellite-derived data products: An application over a semi-arid ecosystem in the us. *PloS one*, 12(8):e0180239.

CHAPTER 3

High-sensitivity Earth System Models most Consistent with Observations[1]

Collaborative Paper with Thomas Leirvik[1], Trude Storelvmo[1,2], Kari Alterskjær[1,3], Peter C.B. Phillips[4,5,6,7], and Christopher J. Smith[8,9]

[1] *Nord University Business School, Norway*
[2] *University of Oslo, Nord University, Norway*
[3] *Center for International Climate and Environmental Research (Cicero), Norway*
[4] *University of Auckland, New Zealand*
[5] *Yale University, United States of America*
[6] *Singapore Management University, Singapore*
[7] *University of Southampton, United Kingdom*
[8] *University of Leeds, United Kingdom*
[9] *International Institute for Applied Systems Analysis (IIASA), Laxenburg, Austria*

---

[1] Paper submitted to *Nature Communications*. Under review.

Abstract

Earth's transient climate response (TCR) quantifies the global mean surface air temperature change due to a doubling of atmospheric CO_2, at the time of doubling. TCR is highly correlated with near-term climate projections, and thus of utmost relevance for climate policy, but remains poorly constrained. Within state-of-the-art Earth System Models (ESMs) participating in the Coupled Model Intercomparison Project (CMIP6), the TCR range (1.1 - 2.9°C) is much too wide to offer useful guidance to policymakers on remaining carbon budgets aligneded with the Paris agreement goals. To address this issue, we here present an observation-based TCR estimate of 2.3±0.4°C (95 % confidence interval). We show that this method correctly diagnoses TCR from 22 CMIP6 ESMs if the same variables are taken from the ESMs as are available from observations. This increases confidence in the new estimate and range, which are higher and narrower, respectively, than those of the CMIP6 ensemble.

The question of exactly how sensitive Earth's climate is to atmospheric greenhouse gas perturbations has been long-standing in the climate research community and is of mounting concern in society at large. Yet, arguably, we are no closer to the answer today than we were several decades ago (IPCC, 2001). This uncertainty, in turn, translates into highly uncertain climate projections for a given future emission-scenario (Tebaldi et al., 2020), with obvious consequences for society's ability to take necessary mitigation and adaptation action. TCR has been demonstrated to correlate well with near-term climate projections across a wide range of emission scenarios (Grose et al., 2018; Huusko, L., Bender, F., Ekman, A. & Storelvmo, 2021), and is therefore among the metrics of Earth's climate sensitivity most relevant for today's decision makers.

The latest generation of ESMs in the CMIP6 (Eyring et al., 2016) ensemble produces a mean TCR of 2.0°C, somewhat higher than the previous ESM generation (CMIP5 mean of 1.8°C) (Meehl et al., 2020). For context, the most recent report from the Intergovernmental Panel for Climate Change (IPCC AR5) assessed the likely TCR range to be 1.0 to 2.5°C (Flato and Marotzke, 2013). Multiple CMIP6 models now produce TCR values well above the upper end of this range (Meehl et al., 2020), raising questions about the plausibility of some of the most sensitive ESMs.

New observation-based TCR estimate

The above serves as the backdrop for the research presented here, which takes advantage of a new observational approach to determine TCR (Phillips et al., 2020). The method merges observations of well-mixed atmospheric greenhouse gas concentrations with surface air temperature and surface radiation fluxes from more than 2500 locations worldwide for the past five decades into a panel data set and thereafter uses statistical methods that are well established within the field of econometrics to indirectly determine TCR (see Methods). An important innovation of the approach is that it uses an observational proxy for the cooling effect of aerosols, in order to isolate the observed surface air temperature change that can be attributed to atmospheric greenhouse gas changes, thus allowing for TCR inference. Other efforts to constrain TCR based on historical observations have generally relied on ESM output for aerosol cooling estimates (Otto et al.,

2013) or have been based on the premise that aerosol cooling has remained nearly constant in recent decades (Jiménez-de-la Cuesta and Mauritsen, 2019). The latter is based on the fact that globally, emissions of aerosol particles and their precursors have been relatively stable since the mid-1970s. However, there is ample evidence that a near-constant global mean atmospheric aerosol burden does not directly translate to a constant global mean aerosol cooling, as the spatial distribution of aerosols is also of critical importance for the global mean aerosol effect on climate (Regayre et al., 2014; Shindell et al., 2015; Persad and Caldeira, 2018). Indeed, the spatial distribution of atmospheric aerosols has changed considerably in recent decades (Hoesly et al., 2018), and the associated climate impacts are expected to be non-negligible (Marvel et al., 2016). These effects can be captured with spatial modeling through our panel data approach.

Given its independence from ESMs, the method applied here has the potential to serve as an important tool for evaluation of ESM-simulated TCR. In a first application of this method, TCR was estimated to 2.0±0.8°C (Storelvmo et al., 2016), while in the present study updates to the observational data sets and further development of the method (Phillips et al., 2020) produce a somewhat higher estimate and a considerably narrower uncertainty range of 2.3±0.4°C, thus supporting some of the higher TCR estimates emerging from CMIP6. Here, we present evidence that the observational method can in fact correctly diagnose TCR. This is done by comparing the standard TCR calculation from 22 CMIP6 models (see Supplementary Table B.3) with the TCR values estimated when the same variables that are available from observations are also extracted from the 22 models and used in the same way in the observational analysis (the TCR values estimated from the observational analysis will hereinafter be referred to as E-TCR). The number of ESMs included in the analysis was determined by the availability of model simulations and output variables required to calculate E-TCR.

Increasing confidence in the new TCR estimate

To determine whether any method can in fact correctly diagnose TCR, one could simply wait for a couple of decades, as the role of aerosol cooling is expected to diminish with time due to projected reductions in anthropogenic aerosol emissions (Gidden et al., 2019; Shindell and Smith, 2019). The observed warming would therefore increasingly be attributable to greenhouse gas increases, and first and foremost CO_2 (Myhre et al., 2015). With time, it should therefore be possible to infer TCR from observations with a considerably reduced uncertainty range. However, important climate policy decisions cannot wait for the more constrained TCR estimates that would eventually emerge; for example, a halving of the uncertainty range for TCR has been estimated to have a net present value of about $9.7 trillion if accomplished by 2030 (Hope, 2015).

Motivated by this urgency, we here test the new method on 'synthetic observations' from the aforementioned 22 ESMs, to confirm that it can correctly diagnose the 'true' TCR from each of the models. The 'true' value is based on ESM simulations in which atmospheric CO_2 is increased by 1% per year until a doubling is reached, at which point TCR can be calculated as the global mean surface air temperature difference relative to that of a control simulation with pre-industrial atmospheric CO_2 concentrations.

As evident from Figure 3.1, the TCR distribution based on the standard calculation and the E-TCR emerging from the synthetic observations extracted from the ESMs are indeed very similar, albeit the latter produces a slightly higher ensemble mean (E-TCR mean of 2.16°C vs. TCR mean of 2.05 °C).

As further proof that the observational TCR estimate is reliable, there is also a positive correlation between the estimated E-TCR values and the TCR values based on standard calculations for the CMIP6 models (r=0.61, Figure 3.2), with low-TCR models correctly being diagnosed as such, and vice versa. Nevertheless, we note a slight tendency for the method to overestimate TCR from low-sensitivity ESMs and underestimate high-sensitivity models' TCR.

Finally, Figure 3.3 shows that among the 22 ESMs considered, 20 have TCR values that lie within the estimated 95% confidence interval, while the remaining two (NorESM2-LM and GISS-E2-1-H) have TCR values that are at the confidence interval margins.

Based on this evidence we have high confidence in the ability of the TCR method to correctly diagnose the TCR of the real climate system, which is thus very likely to lie in the estimated observation-based confidence interval of 1.9

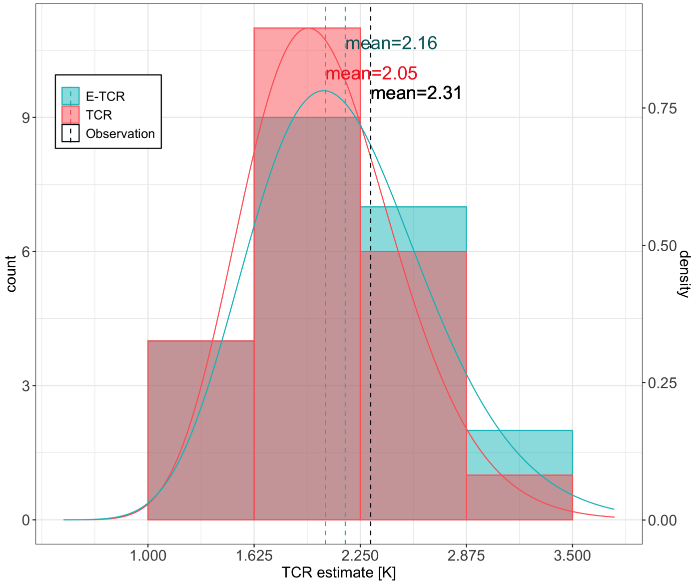

Fig. 3.1 Histograms of TCR from 22 CMIP6 models based on standard calculations (red) and estimated based on synthetic observations extracted from the ESMs (blue). Fitted gamma distributions for the standard TCR calculations (red line) and the estimated values (blue line) are also shown.

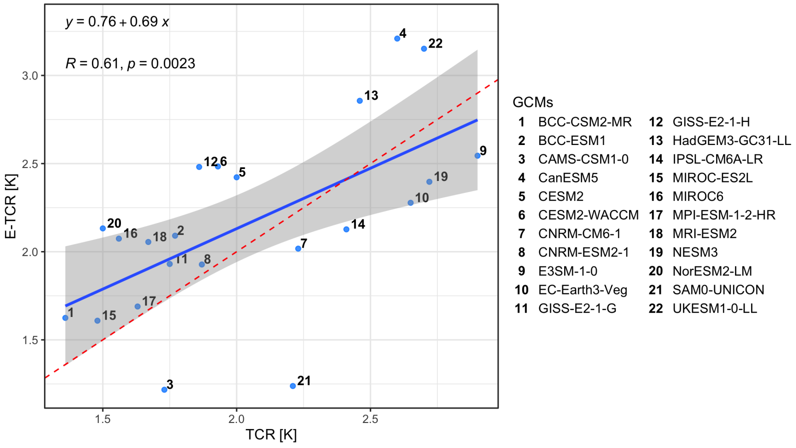

Fig. 3.2 TCR values based on standard calculations vs. those estimated based on synthetic observations from 22 CMIP6 models

to 2.7°C. Notably, only about half the CMIP6 models analyzed here produce TCRs that lie within this range. Out of the ones that do not, ten underestimate TCR relative the observation-based range, while only one overestimates it. In

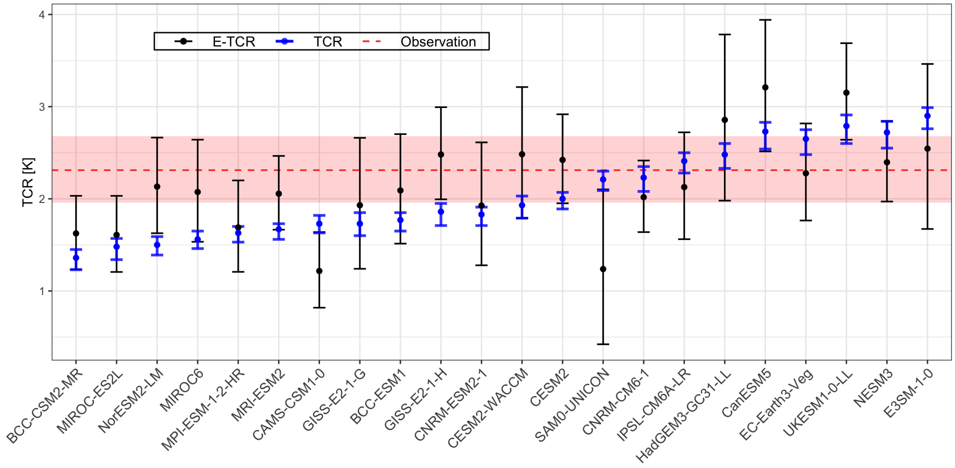

Fig. 3.3 TCR values based on standard calculations for 22 CMIP6 models (blue filled circles, bars showing 95% confidence interval) and the corresponding estimated TCR values (black filled circles, bars showing 95% confidence intervals) using the exact same data and method as were used to produce the observational estimate. The horizontal dashed red line shows central observational estimate, while the pale red shaded band shows the observational 95% confidence interval.

other words, the higher CMIP6 ensemble mean TCR relative to previous ESM generations is strongly supported by the findings presented here. This stands in contrast to recent studies that have attempted to use the rate of warming in recent decades to constrain TCR, arriving at best estimates of TCR as low as 1.6°C (Tokarska et al., 2020). However, these findings rely heavily on the accuracy of a near-constant aerosol cooling in recent decades, as simulated by CMIP6 models, which is not supported by the present observational framework (see Supplementary Material).

Implications for climate projections and remaining carbon budgets

The implications of these findings are wide-reaching. Using statistical methods suited to the nonstationary and jointly dependent properties of the data we have shown that the CMIP6 models with higher TCR are generally more consistent with observations. The results further demonstrate that the approach used to estimate TCR from observations (E-TCR) is capable of diagnosing the true TCR when applied to synthetic observations from 22 CMIP6 ESMs. This capability reinforces the method used here to produce a TCR estimate of $2.3 \pm 0.4°C$, a finding that requires a substantial downward revision of how much additional burning of coal, gas and oil is allowable without considerable risk of exceeding $1.5°C$ of warming relative to pre-industrial times, as most previous calculations have assumed a TCR that is well below the observation-based estimate presented here (Millar et al., 2017).

Using the distribution of observation-based TCR of 2.3 ± 0.4°C, convoluted with other uncertainties in the remaining carbon budget (Matthews et al., 2021), leads to a remaining carbon budget to 1.5°C of 360 (245-470) $GtCO_2$ (median and 33-67% range) from 2020 (see Methods), or around nine years of current CO_2 emissions (Friedlingstein et al., 2020). Reported CMIP6 TCR values provide a remaining carbon budget of 405 (275-535) $GtCO_2$ from 2020, hence the revised TCR results in a median reduction in the remaining carbon budget of approximately one year of allowable CO_2 emissions. This reduction can be compared with a recent assessment of TCR from other lines of evidence (Sherwood et al., 2020) that results in a remaining carbon budget of 450 (305-590) $GtCO_2$, or approximately two more years' allowable CO_2 emissions for a 50% chance of remaining below 1.5°C compared to the observational TCR estimate. The narrower distribution and higher central value of observational TCR compared to other estimates also reduces the uncertainty in the remaining carbon budget (Figure 3.4), and one effect of this is to reduce the probability that larger values of cumulative emissions are consistent with a 1.5°C carbon budget.

Data and Methods

The data leading to the findings presented above come from both observations and ESM simulations. Observed surface air temperature data are available from the Climate Research Unit in the University of East Anglia (Harris et al., 2020). Observed surface solar radiation data are from an interpolated dataset based on the Global Energy Balance Archive (Wild et al., 2017), constructed using a machine learning method (Leirvik and Yuan, 2021). Both the observational datasets are available at 0.5° resolution. Simulation counterparts, termed

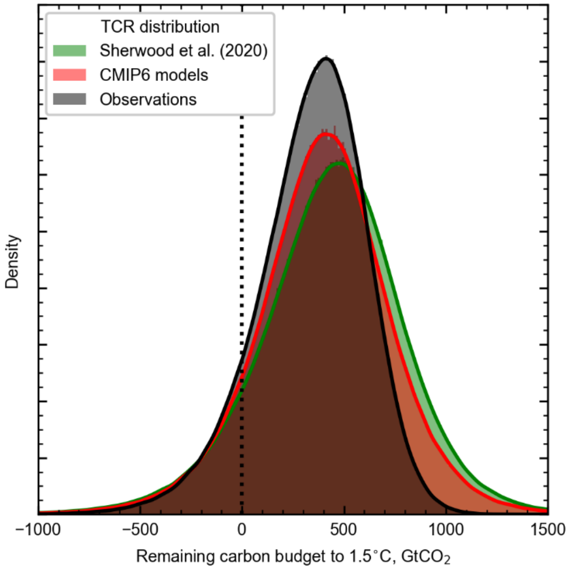

Fig. 3.4 Remaining carbon budget to 1.5°C using the distribution of TCR from observations (black), reported TCR values from CMIP6 models (red), and the distribution of TCR from the assessment of Sherwood et al. (2020) (Sherwood et al., 2020).

'synthetic observations', are obtained from the historical simulations of 22 Earth system models from the CMIP6 (Eyring et al., 2016). A single realization is used per model, even though ensembles of simulations are available for some models. The simulation data of surface air temperature and surface solar radiation are gridded monthly records over all land areas except for Antarctica, with various resolutions. We thereby aggregate the grid cell values to global land averages, weighed by the cosine of latitudes to account for the areas of gridboxes reduce with increasing latitude. Due to data availability we limit the study to the time period from 1964 to 2014.

Our source of global CO_2 equivalent concentrations is the National Oceanic and Atmospheric Administration (NOAA) Annual Greenhouse Gas Index (ACGI), which contains measures of the interannual variability of global forcing resulting from changes in greenhouse gases. CO_2 is known to be the largest contributor to the index, and all non-CO_2 greenhouse gas effects are converted into changes in global forcing and aggregated with that of CO_2. In other words, the Annual Greenhouse Gas Index is deemed as an instrument of equivalent CO_2 atmospheric concentrations.

Panel data sets generally consist of information accumulated over time (t) for units that are, in this case, spatial grid cells (i). The transient climate response in this study is estimated using an empirical econometric framework which relates surface air temperature at time $t+1$ for location i ($T_{i,t+1}$) to temperature and surface solar radiation observed at the same location but in the previous time period ($T_{i,t}$ and $R_{i,t}$, respectively), and CO_2 equivalent emissions ($CO_{2,t}$). The CO_2 is assumed uniformly distributed in the atmosphere, so there is no location unit i. The following econometric representation is used for the analysis in this paper

$$T_{i,t+1} = \alpha_i + \beta_1 T_{i,t} + \beta_2 R_{i,t} + \phi_i \lambda_t + u_{i,t+1}, \tag{3.1a}$$

$$\lambda_t = \gamma_0 + \gamma_1 \bar{T}_t + \gamma_2 \bar{R}_t + \gamma_3 ln(CO_{2,t}), \tag{3.1b}$$

$$i = 1, \cdots, N \text{ and } t = 1, \cdots, n$$

Here, Eqn.(3.1a) uses regressor values for temperature and radiation at time t for unit i[2], whereas Eqn. (3.1b) uses averages of these two variables taken over all spatial cells i at time t. The component λ_t provides a measure of the prevailing time specific global factors at t representing the global energy effects determined by the global mean temperature ($\bar{T}_t$), radiation ($\bar{R}_t$), and the logarithm of the CO_2 equivalent emissions ($ln(CO_{2,t})$). The transient climate response can be estimated as a “reduced form” parameter

$$TCR = \frac{\gamma_3}{1-\beta_1-\gamma_1} \times \ln(2), \tag{3.2}$$

that embodies the global impact of these various forces on temperature. Estimates of the coefficients are obtained by fully modified least squares (FM-OLS, Phillips and Hansen, 1990), which allows for general assumptions concerning the cross section and time series dependence common in panel data. Readers are referred to the SI for the details of the estimation method.

Note that our datasets cover only land areas. Therefore we need to convert to a global estimate by following a conversion procedure (Storelvmo et al.,

---

[2] A unit here is a grid-cell or a physical station at which climatic measurements takes place.

2016), which converts land transient climate response to global transient climate response based on land/ocean area fraction and land-ocean warming ratio (see the SI for details).

Remaining carbon budget calculation

The remaining carbon budget (RCB) up to a particular temperature limit above pre-industrial ΔT_{lim}, such as 1.5°C, can be conceptualized as (Matthews et al., 2021)

$$RCB = \frac{\Delta T_{lim}(1 - f^*_{nc}) - \Delta T_{anth}(1 - f_{nc})}{TCRE}, \tag{3.3}$$

where ΔT_{anth} is the anthropogenic-attributed warming since pre-industrial, f_{nc} is the present-day fraction of anthropogenic effective radiative forcing from non-CO_2 sources, f^*_{nc} is the non-CO_2 forcing fraction at net-zero CO_2 emissions, and TCRE is the transient climate response to cumulative emissions of CO_2.

TCRE can be approximated as (Jones and Friedlingstein, 2020)

$$TCRE = a_f \cdot \frac{TCR}{\Delta C_{2\times CO_2}}, \tag{3.4}$$

where a_f is the cumulative airborne fraction taken at the time of doubling of CO_2 in a 1% per year compound CO_2 increase (i.e., approximately after 70 years) and $\Delta C_{2\times CO_2}$ is the increase in atmospheric carbon mass for a doubling of pre-industrial CO_2. Using a pre-industrial CO_2 value of 284.32 ppm representative of 1850 conditions (Meinshausen et al., 2017) as used in CMIP6 and a conversion of 1 ppm = 2.124 GtC (Friedlingstein et al., 2020) gives $\Delta C_{2\times CO_2} = 604$ GtC.

To generate distributions of the remaining carbon budget to $\Delta T_{lim} = 1.5$°C a 1-million member Monte Carlo ensemble was produced. TCR is sampled as gamma distributed for reported TCR from CMIP6 models from the distribution in Figure 3.1, and as normally distributed for the observational TCR using the mean of 2.31 K and standard deviation 0.18 K. For the estimate from Sherwood et al. (2020) we use a normal distribution with mean of 1.85 K and standard deviation of 0.35 K to approximate the median and 66% range of 1.8 (1.5-2.2) K in Sherwood et al. 2020. In all cases, airborne fraction is sampled from a normal distribution using the results from 11 CMIP6 carbon-cycle models in Arora et al. (2020) with mean 0.532 and standard deviation 0.033.

From the derived TCRE distributions, the remaining carbon budget is computed by sampling the terms in Eqn. (3.3) from distributions in Matthews et al. (2021). f_{nc} is taken from mean 1990-2019 non-CO_2 forcing fractions from all 411 integrated assessment model (IAM) scenarios considered by the IPCC Special Report on 1.5°C (Rogelj et al., 2018) (median 0.14, 5-95% range -0.11 to 0.33) and sampled using a kernel density estimate. The non-CO_2 forcing fraction at net-zero $f^*_{nc} = 0.3081 f_{nc} + 0.14 + \epsilon$ where ϵ is sampled as a normal distribution (mean 0 and 5-95% range of 0.05) that represents additional future socioeconomic pathway uncertainty up to net-zero CO_2 emissions in IAM scenarios (Matthews et al., 2021). ΔT_{anth} is sampled as a skew-normal distribution fit to best-estimate and 5-95% uncertainty of anthropogenic warming from 1850-1900 to 2019 of 1.18 (1.05 to 1.41) °C (Matthews et al., 2021).

RCB calculations are converted from units of GtC to $GtCO_2$ (multiplied by 3.664) and reported to the nearest 5 $GtCO_2$ from the beginning of 2020. The RCB using observed TCR is 360 (245-470) $GtCO_2$, compared to 405 (275-535) $GtCO_2$ using the CMIP6 TCR and 450 (305-590) $GtCO_2$ using the Sherwood et al. (2020) TCR assessment. These estimates can be compared to the process-based estimate of 440 (230-670) $GtCO_2$ using the TCRE distribution in Matthews et al. (2021). The RCB estimates presented from the TCR assessments here have less spread than the range presented in Matthews et al. (2021), which is likely a consequence of the relatively small spread in the airborne fraction distribution.

References

Arora, V. K., Katavouta, A., Williams, R. G., Jones, C. D., Brovkin, V., Friedlingstein, P., Schwinger, J., Bopp, L., Boucher, O., Cadule, P., Chamberlain, M. A., Christian, J. R., Delire, C., Fisher, A. R. A., Hajima, T., Ilyina, T., Joetzjer, E., Kawamiya, M., Koven, C. D., Krasting, J. P., Law, R. M., Lawrence, D. M., Lenton, A., Lindsay, K., Pongratz, J., Raddatz, T., Séférian, R., Tachiiri, K., Tjiputra, J. F., Wiltshire, A., Wu, T., and Ziehn, T. (2020). Carbon-concentration and carbon-climate feedbacks in CMIP6 models and their comparison to CMIP5 models. *Biogeosciences*, 17(16):4173–4222.

Eyring, V., Bony, S., Meehl, G. A., Senior, C. A., Stevens, B., Stouffer, R. J., and Taylor, K. E. (2016). Overview of the Coupled Model Intercomparison Project Phase 6 (CMIP6) experimental design and organization. *Geoscientific Model Development*, 9(5):1937–1958.

Flato, G. and Marotzke, J. (2013). *Evaluation of Climate Models.* Cambridge University Press.

Friedlingstein, P., O'Sullivan, M., Jones, M. W., Andrew, R. M., Hauck, J., Olsen, A., Peters, G. P., Peters, W., Pongratz, J., Sitch, S., Le Quéré, C., Canadell, J. G., Ciais, P., Jackson, R. B., Alin, S., Aragão, L. E., Arneth, A., Arora, V., Bates, N. R., Becker, M., Benoit-Cattin, A., Bittig, H. C., Bopp, L., Bultan, S., Chandra, N., Chevallier, F., Chini, L. P., Evans, W., Florentie, L., Forster, P. M., Gasser, T., Gehlen, M., Gilfillan, D., Gkritzalis, T., Gregor, L., Gruber, N., Harris, I., Hartung, K., Haverd, V., Houghton, R. A., Ilyina, T., Jain, A. K., Joetzjer, E., Kadono, K., Kato, E., Kitidis, V., Korsbakken, J. I., Landschützer, P., Lefèvre, N., Lenton, A., Lienert, S., Liu, Z., Lombardozzi, D., Marland, G., Metzl, N., Munro, D. R., Nabel, J. E., Nakaoka, S. I., Niwa, Y., O'Brien, K., Ono, T., Palmer, P. I., Pierrot, D., Poulter, B., Resplandy, L., Robertson, E., Rödenbeck, C., Schwinger, J., Séférian, R., Skjelvan, I., Smith, A. J., Sutton, A. J., Tanhua, T., Tans, P. P., Tian, H., Tilbrook, B., Van Der Werf, G., Vuichard, N., Walker, A. P., Wanninkhof, R., Watson, A. J., Willis, D., Wiltshire, A. J., Yuan, W., Yue, X., and Zaehle, S. (2020). Global Carbon Budget 2020. *Earth System Science Data*, 12(4):3269–3340.

Gidden, M. J., Riahi, K., Smith, S. J., Fujimori, S., Luderer, G., Kriegler, E., van Vuuren, D. P., van den Berg, M., Feng, L., Klein, D., Calvin, K., Doelman, J. C., Frank, S., Fricko, O., Harmsen, M., Hasegawa, T., Havlik, P., Hilaire, J., Hoesly, R., Horing, J., Popp, A., Stehfest, E., and Takahashi, K. (2019). Global emissions pathways under different socioeconomic scenarios for use in CMIP6: a dataset of harmonized emissions trajectories through the end of the century. *Geoscientific Model Development*, 12(4):1443–1475.

Grose, M. R., Gregory, J., Colman, R., and Andrews, T. (2018). What Climate Sensitivity Index Is Most Useful for Projections? *Geophysical Research Letters.*

Harris, I., Osborn, T. J., Jones, P., and Lister, D. (2020). Version 4 of the CRU TS monthly high-resolution gridded multivariate climate dataset. *Scientific Data*, 7(1).

Hoesly, R. M., Smith, S. J., Feng, L., Klimont, Z., Janssens-Maenhout, G., Pitkanen, T., Seibert, J. J., Vu, L., Andres, R. J., Bolt, R. M., Bond, T. C., Dawidowski, L., Kholod, N., Kurokawa, J.-i., Li, M., Liu, L., Lu, Z., Moura, M. C. P., O'Rourke, P. R., and Zhang, Q. (2018). Historical (1750–2014) anthropogenic emissions of reactive gases and aerosols from the Community Emissions Data System (CEDS). *Geoscientific Model Development*, 11(1):369–408.

Hope, C. (2015). The $10 trillion value of better information about the transient climate response. *Philosophical Transactions of the Royal Society A: Mathematical, Physical and Engineering Sciences*, 373(2054):20140429.

Huusko, L., Bender, F., Ekman, A. & Storelvmo, T. (2021). Climate sensitivity indices and their relation with projected temperature change in CMIP6 models. *Environmental Research Letters*.

IPCC (2001). Third Assessment Report, Climate Change 2001: The Scientific Basis. *Climate Change 2001: The Scientific Basis*.

Jiménez-de-la Cuesta, D. and Mauritsen, T. (2019). Emergent constraints on Earth's transient and equilibrium response to doubled CO2 from post-1970s global warming. *Nature Geoscience*, 12(11):902–905.

Jones, C. D. and Friedlingstein, P. (2020). Quantifying process-level uncertainty contributions to TCRE and carbon budgets for meeting Paris Agreement climate targets. *Environmental Research Letters*, 15(7):074019.

Leirvik, T. and Yuan, M. (2021). A Machine learning technique for spatial interpolation of solar radiation observations. *Earth and Space Science*, page e2020EA001527.

Marvel, K., Schmidt, G. A., Miller, R. L., and Nazarenko, L. S. (2016). Implications for climate sensitivity from the response to individual forcings. *Nature Climate Change*, 6(4):386–389.

Matthews, H., Tokarska, K. B., Rogelj, J., Smith, C. J., MacDougall, A. H., Haustein, K., Mengis, N., Sippel, S., Forster, P. M., and Knutti, R. (2021). An integrated approach to quantifying uncertainties in the remaining carbon budget. *Communications Earth & Environment*, 2(1):1–11.

Meehl, G. A., Senior, C. A., Eyring, V., Flato, G., Lamarque, J. F., Stouffer, R. J., Taylor, K. E., and Schlund, M. (2020). Context for interpreting equilibrium climate sensitivity and transient climate response from the CMIP6 Earth system models.

Meinshausen, M., Vogel, E., Nauels, A., Lorbacher, K., Meinshausen, N., Etheridge, D. M., Fraser, P. J., Montzka, S. A., Rayner, P. J., Trudinger, C. M., Krummel, P. B., Beyerle, U., Canadell, J. G., Daniel, J. S., Enting, I. G., Law, R. M., Lunder, C. R., O'Doherty, S., Prinn, R. G., Reimann, S., Rubino, M., Velders, G. J., Vollmer, M. K., Wang, R. H., and Weiss, R. (2017). Historical greenhouse gas concentrations for climate modelling (CMIP6). *Geoscientific Model Development*, 10(5):2057–2116.

Millar, R. J., Fuglestvedt, J. S., Friedlingstein, P., Rogelj, J., Grubb, M. J., Matthews, H. D., Skeie, R. B., Forster, P. M., Frame, D. J., and Allen, M. R. (2017). Emission budgets and pathways consistent with limiting warming to 1.5 °C. *Nature Geoscience*, 10(10):741–747.

Myhre, G., Boucher, O., Bréon, F. M., Forster, P., and Shindell, D. (2015). Declining uncertainty in transient climate response as CO2 forcing dominates future climate change. *Nature Geoscience*, 8(3):181–185.

Otto, A., Otto, F. E., Boucher, O., Church, J., Hegerl, G., Forster, P. M., Gillett, N. P., Gregory, J., Johnson, G. C., Knutti, R., Lewis, N., Lohmann, U., Marotzke, J., Myhre, G., Shindell, D., Stevens, B., and Allen, M. R. (2013). Energy budget constraints on climate response.

Persad, G. G. and Caldeira, K. (2018). Divergent global-scale temperature effects from identical aerosols emitted in different regions. *Nature Communications*, 9(1):1–9.

Phillips, P. C., Leirvik, T., and Storelvmo, T. (2020). Econometric estimates of Earth's transient climate sensitivity. *Journal of Econometrics*, 214(1):6–32.

Phillips, P. C. B. and Hansen, B. E. (1990). Statistical Inference in Instrumental Variables Regression with I(1) Processes. *The Review of Economic Studies*, 57(1):99.

Regayre, L. A., Pringle, K. J., Booth, B. B. B., Lee, L. A., Mann, G. W., Browse, J., Woodhouse, M. T., Rap, A., Reddington, C. L., and Carslaw, K. S. (2014). Uncertainty in the magnitude of aerosol-cloud radiative forcing over recent decades. *Geophysical Research Letters*, 41(24):9040–9049.

Rogelj, J., Popp, A., Calvin, K. V., Luderer, G., Emmerling, J., Gernaat, D., Fujimori, S., Strefler, J., Hasegawa, T., Marangoni, G., Krey, V., Kriegler, E., Riahi, K., Van Vuuren, D. P., Doelman, J., Drouet, L., Edmonds, J., Fricko, O., Harmsen, M., Havlík, P., Humpenöder, F., Stehfest, E., and Tavoni, M. (2018). Scenarios towards limiting global mean temperature increase below 1.5 °c. *Nature Climate Change*, 8(4):325–332.

Sherwood, S. C., Webb, M. J., Annan, J. D., Armour, K. C., Forster, P. M., Hargreaves, J. C., Hegerl, G., Klein, S. A., Marvel, K. D., Rohling, E. J., Watanabe, M., Andrews, T., Braconnot, P., Bretherton, C. S., Foster, G. L., Hausfather, Z., Heydt, A. S., Knutti, R., Mauritsen, T., Norris, J. R., Proistosescu, C., Rugenstein, M., Schmidt, G. A., Tokarska, K. B., and Zelinka, M. D. (2020). An Assessment of Earth's Climate Sensitivity Using Multiple Lines of Evidence. *Reviews of Geophysics*, 58(4):e2019RG000678.

Shindell, D. and Smith, C. J. (2019). Climate and air-quality benefits of a realistic phase-out of fossil fuels. *Nature*, 573(7774):408–411.

Shindell, D. T., Faluvegi, G., Rotstayn, L., and Milly, G. (2015). Spatial patterns of radiative forcing and surface temperature response. *Journal of Geophysical Research: Atmospheres*, 120(11):5385–5403.

Storelvmo, T., Leirvik, T., Lohmann, U., Phillips, P. C. B., and Wild, M. (2016). Disentangling greenhouse warming and aerosol cooling to reveal Earth's climate sensitivity. *Nature Geoscience*, 9(4):286–289.

Tebaldi, C., Debeire, K., Eyring, V., Fischer, E., Fyfe, J., Friedlingstein, P., Knutti, R., Lowe, J., O'Neill, B., Sanderson, B., van Vuuren, D., Riahi, K., Meinshausen, M., Nicholls, Z., Hurtt, G., Kriegler, E., Lamarque, J.-F., Meehl, G., Moss, R., Bauer, S., Boucher, O., Brovkin, V., Golaz, J.-C., Gualdi, S., Guo, H., John, J., Kharin, S., Koshiro, T., Ma, L., Olivié, D., Panickal, S., Qiao, F., Rosenbloom, N., Schupfner, M., Seferian, R., Song, Z., Steger, C., Sellar, A., Swart, N., Tachiiri, K., Tatebe, H., Voldoire, A., Volodin, E., Wyser, K., Xin, X., Xinyao, R., Yang, S., Yu, Y., and Ziehn, T. (2020). Climate model projections from the Scenario Model Intercomparison Project (ScenarioMIP) of CMIP6. *Earth System Dynamics Discussions*, pages 1–50.

Tokarska, K. B., Stolpe, M. B., Sippel, S., Fischer, E. M., Smith, C. J., Lehner, F., and Knutti, R. (2020). Past warming trend constrains future warming in CMIP6 models. *Science Advances*, 6(12).

Wild, M., Ohmura, A., Schär, C., Müller, G., Folini, D., Schwarz, M., Zyta Hakuba, M., and Sanchez-Lorenzo, A. (2017). The Global Energy Balance Archive (GEBA) version 2017: A database for worldwide measured surface energy fluxes. *Earth System Science Data*, 9(2):601–613.

CHAPTER 4

Heterogeneity in Climate Change Effects on Soybean Yields

Abstract

Using a panel of 74 countries that spans nearly 60 years, this paper investigates the effects of climate change on global soybean yields. In alignment with other research, we find a global non-linear relationship between growing season average temperature and yield growth—a parabola that minimizes around $24.9°C$. It indicates that effects of warming change from being beneficial to harmful, and reach to the most damaging at the optimum temperature; however, beyond the optimum, warming becomes less detrimental probably due to adaption of local crop variety to heat at countries that have been persistently hot. However, by incorporating regional dummies to our empirical model, we find significant heterogeneity in different regions. For example, in contrary to the global response function that opens upwards, the opposite direction, a downward open response function, is found for Southeast Asia, such that crop yield growth maximizes at $24.23°C$. We also demonstrate non-linear effects of precipitation. In contrast to the large heterogeneity in temperature effects, the regional response functions for precipitation are more consistent over the world. Except for regions not sensitive to precipitation change, Southeast Asia, Eastern Europe & Central Asia, and Sub-Saharan Africa all show a downward open parabolic response curve to precipitation. In addition to temperature and precipitation, we highlight the importance of considering diurnal temperature change (dtr) in assessing climate change impacts on crop yields. We find significance of dtr across all regions—an additional $1°C$ dtr will slow global soybean yield growth by 4.1 percentage points.

4.1 Introduction

The Fifth Assessment Report of IPCC (Intergovernmental Panel on Climate Change) has reported global annual mean temperature has increased by $0.74°C$ during the last century, with even larger warming observed in specific regions (IPCC AR5, 2014). It also reported increased precipitation in Northern Hemisphere especially after 1951. Growing evidence demonstrates climate change has profound impacts on crop production. Understanding changes in crop production induced by climate change is of essential importance to food security, agricultural adaptation, and social welfare, as it characterizes historical patterns of crop responses to climate change, and provides a guidance to identify adaptation opportunities and potential agricultural consequences of future climate change.

Attempts to measure impacts of climate change on agriculture have evolved a lot since the early 1960s and broadly fall into two major approaches: process-based models, which simulate the key processes in crop growing and yield formation in experimental labs; and statistical models, which estimate the sensitivity of crop yields to climate variables based on regression analysis on observational data. Process-based crop simulation models parameterize soil, weather, and crop management in a function of the soil-plant-atmosphere biophysical dynamics. The simulation models are typically used for applications in on-farm and precision management, and are increasingly used in assessments of the short-term impact of climate variability (see e.g., Lobell and Burke, 2010; Rosenzweig et al., 2013; Lobell and Asseng, 2017). On the other hand, statistical models empirically estimate the relationship between crop yields and weather variables. Results from the two approaches are compared to each other in studies, suggesting broadly consistency (Lobell et al., 2008; Lobell and Burke, 2010; Liu et al., 2016) despite of certain divergence due to scenario settings and differences in the analytical approaches. Although both approaches can provide useful crop yield predictions, process-based models require more resources in calculation and calibration, moreover, they are limited to only a few varieties of crops, mostly maize, wheat, and rice, which limits their application beyond the major grains.

The statistical approach uses a so-called a *response function* to describe the effects of climate change on economic growth. Substantial debates about the response function exist over (i) the linearity of the relationship, (2) heterogeneity in countries' responses to climate change over the world. Lobell et al. (2008); Dell et al. (2012); Liu et al. (2016) used a linear specification of temperature and precipitation, which assumes monotonically effects of climate change. Based on a linear model, Dell et al. (2012) reported significant difference in responses between rich and poor countries. Rich countries are not sensitive to temperature change, yet are negative affected by more precipitation. On the other hand, poor countries are only sensitive to temperature variability; a $1°C$ rise in temperature will lead to a decrease of annual growth rate of economies by 1.35%. On the contrary, Burke et al. (2015) used a non-linear relationship, more specifically, a quadratic specification of weather variables, in the response function. They found a downward open curve response function of temperature, such that economic growth maximizes at $13.06°C$. They agreed that rich countries will be less affected by a global warming as compared to poor countries; however, they claimed the difference in the responses is not because they have different sensitivities to climate change, but rather due to their various initial levels of temperature on the response curve. Specifically, poor countries are hurt simply because they have annual average temperatures greater than the optimal value, and rich countries are less hurt, or even benefit, from a global warming because they are colder and have annual average temperatures smaller than the optimal value. Burke et al. further reported non-significance of precipitation to GDP growth.

Response difference is also found among regions from meta-analyses, which consolidate regional estimates from numerous references and based on which generate bootstrapped estimates of responses for individual regions/countries (see e.g., Lobell et al., 2008; Liu et al., 2016; Carleton and Hsiang, 2016; Zhao et al., 2017). Nevertheless, it remains unclear whether the difference in responses is due to different sensitivities of response functions, or just because regions have different starting points on the response curve. To investigate the attribution of the regional heterogeneity, we interact climate variables with regional dummy variables and a rich/poor dummy. This specification explicitly allows for differing sensitivities to climate change based on region and rich/poor categories.

Temperature is deemed to be the dominant factor in the response functions in literature (see e.g., Burke et al., 2015; Diffenbaugh and Burke, 2019; Zhao et al., 2017). Understanding crop responses to temperature and the magnitude of regional temperature changes are the two most important needs for reducing uncertainty in predicting future crop yields (Lobell et al., 2008). Previous studies of response functions have primarily focused on the impacts of growing season average temperature, with few work ever quantifying crop yield responses to extreme temperatures. However, extremes are important to consider for that extreme temperatures occurring at crucial stages of crop formation can drastically reduce the final production (Zhang et al., 2014). Response functions could provide significantly different predictions when using extreme temperature proxies, if a crop is substantially more sensitive to one specific extreme temperature index (Lobell and Field, 2007). For example, the predictions using extreme temperature indices are more than 20% lower than that of using average temperature for wheat (Lobell and Field, 2007).

Given the increasing frequency of extreme temperatures, the risks of crop yields damaged by extreme temperature stresses have been increasingly of concern. In order to take into account the effects of temperature extremes, we investigate a novel temperature index, diurnal temperature change ($dtr = t_{max} - t_{min}$, which measures the difference between the temperature extremes). Diurnal temperature reflects the magnitude of temperature stresses. A large diurnal temperature suggests the occurrence of a heat stress (increase of t_{max}) or a cold stress (decrease of t_{min}). Our results further show that the diurnal temperature change is indeed a significant factor to crop yields.

Based on a country-year panel consisting of 74 countries over the period 1963-2018, we investigate how soybean yields have been affected by climate change and focus on the response heterogeneity among regions. The remainder of the paper is organized as follows. Section 2 describes the data and model applied in our estimation strategy. Section 3 provides descriptive statistics of the data and summarizes regression results. Section 4 discusses the results.

4.2 Data and Method

4.2.1 Data

A. The CRU-TS climate dataset

Our analysis uses historical temperature temperature, precipitation, and diurnal temperature range (which is the difference between the maximum temperature and the minimum temperature) as controls in our empirical estimation of climate change effects. Climate Research Unit Time Series (CRU-TS V4.0, Harris et al., 2020) provides monthly time series of the climate variables from 1901 to 2019. Data is available at 0.5 × 0.5 degree resolution for all global land areas excluding Antarctica, and can be downloaded from the CRU website https://crudata.uea.ac.uk/cru/data/hrg/.

B. Growing season and harvest area datasets

Global growing season calendar is available from Sacks et al. (2010). The dataset contains gridded maps of crop planting and harvesting dates for a large variety of crops at 0.5 × 0.5 degree resolution. We select the monthly climate variables within the growing season of soybeans and calculate the averages of them. The resulting data are annual growing season averages of climate variables.

Monfreda et al. (2008) provides cropland coverage data. For each 0.5° grid, a fraction ranging from 0 to 1 of cropland to the whole land is given. Larger fraction means a greater ratio of cropland usage. We use crop fraction data as a mask to gridded climate observations, retaining grids with nonzero values of crop fraction and aggregating them into country level data.

C. Economic data

We use soybeans as an example to illustrate climate change effects on crop yields. Annual country level soybean yields can be obtained from the Food and Agriculture Organization of the United Nations (FAOSTAT, http://www.fao.org/faostat/en/#data/QC). We also consider regional and wealth heterogeneity in our analysis. We here use regional categories in Burke et al. (2015) which classify countries worldwide into six categories, primarily based on their geographical locations and economic development. Figure 4.1 shows the regional classification of the 74 soybean-producing countries applied in this study. In principle, countries clustering geographically belong to the same classification, except for *WEOFF*, which breaks geographical boundaries and covers most of the world's developed countries—Western Europe, Canada, the US, and Australia.

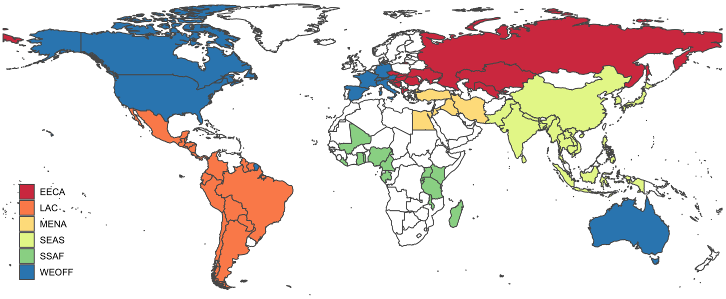

Fig. 4.1 Regional Categories for soybean-producing countries. Countries with the same color belong to the same regional category, while white countries mean they do not have soybean produce.

4.2.2 Empirical Framework

Our empirical framework follows the derivation from Burke et al. (2015), with the following extensions: i) exploring the effects of one new climate variable—diurnal temperature range; ii) allowing parameter heterogeneity in regional responses. Specifically, we consider the following model to estimate climate impacts on crop yields in country i year t

$$\Delta \log y_{i,t} = f_T(T_{i,t}) + f_P(P_{i,t}) + f_{DT}(DT_{i,t}) + \theta_{1,i}t + \theta_{2,i}t^2 + \mu_i + \nu_t + \epsilon_{i,t} \quad (4.1)$$

where $y_{i,t}$ are soybean yields, $f_T(.)$, $f_p(.)$ and $f_{DT}(.)$ are functions of growing season average monthly temperature, precipitation, and diurnal temperature range, respectively. μ_i are the country-fixed effects, v_t are year-fixed effects, and $\theta_{1,i}t + \theta_{2,i}t^2$ are country-specific quadratic time trends. The response is the first difference of the natural log of soybean yields, which can be interpreted as an approximation of annual percentage growth rates. The climate effects on crop yields are captured by the first three terms in Eqn. (B.1a). The quadratic country-specific time trends ($\theta_{1,i}t + \theta_{2,i}t^2$) permit soybean yields to evolve nonlinearly over time, accounting for changes driven by slow changing factors within a country, such as economic and technological advancements, agricultural infrastructure and management shifting, crop adaptation. All time-invariant factors that determine countries' historical average yield growth rates, such as history, culture, and demography, are accounted for in the country-fixed effects (μ_i). Time-varying global shocks such as volcanic eruptions and wild fires, are captured by the time-fixed effects (ν_t).

In the current study, we consider several specifications for functions of climate variables. We use a baseline regression that assumes all countries have the same response function, in particular, we use a quadratic specification for $f_T(.)$ and $f_p(.)$, and a linear specification for $f_{DT}(.)$. We call this a global heterogeneous specification that takes the following form

$$\begin{aligned} f_T(T_{i,t}) &= \beta_1 T_{i,t} + \beta_2 T_{i,t}^2 \\ f_P(T_{i,t}) &= \gamma_1 P_{i,t} + \gamma_2 P_{i,t}^2 \\ f_{DT}(DT_{i,t}) &= \lambda_1 DT_{i,t} \end{aligned} \tag{4.2}$$

The coefficient of diurnal temperature range, λ_1, represents the difference of the responses of crop yields to changes in maximum and minimum temperature. Since

$$\begin{aligned} DT_{i,t} &= T_{max,i,t} - T_{min,i,t} \\ \Delta DT_{i,t} &= \Delta T_{max,i,t} - \Delta T_{min,i,t} \end{aligned} \tag{4.3}$$

an increase of diurnal temperature range ($\Delta DT_{i,t} > 0$) suggests the increase of T_{max} is bigger than that of T_{min}, i.e., $\Delta T_{max,i,t} > \Delta T_{min,i,t}$, which will be the case when heat stress or cold stress happens. λ_1 can then be interpreted as the difference of sensitivity to T_{max} and T_{min}, or $\lambda_1 = \lambda_{max} - \lambda_{min}$, where λ_{max} and λ_{min} represent the sensitivity to T_{max} and T_{min}, respectively. Given that the temperature indices are negatively correlated to crop yields, a positive λ_1 indicates the crop is more sensitive to T_{min} ($|T_{min}| > |T_{max}|$), and a negative λ_1 suggests larger sensitivity to T_{max} ($|T_{min}| < |T_{max}|$).

We also examine two types of heterogeneity in our specifications: regional heterogeneity and wealth heterogeneity. In the regional heterogeneity specification, we interact the temperature and precipitation variables with regional dummy indicators identifying each of the regional category. More specifically, we have

$$\begin{aligned} f_T(T_{i,t}) &= \beta_1 T_{it} + \beta_2 T_{i,t}^2 + \Sigma_{j=3}^{7} \beta_j \times T_{i,t} \times D_{i,j} + \Sigma_{j=8}^{12} \beta_j \times T_{i,t}^2 \times D_{i,j} \\ f_P(T_{i,t}) &= \gamma_1 P_{it} + \gamma_2 P_{i,t}^2 + \Sigma_{j=3}^{7} \gamma_j \times P_{i,t} \times D_{i,j} + \Sigma_{j=8}^{12} \gamma_j \times P_{i,t}^2 \times D_{i,j} \end{aligned} \tag{4.4}$$

where $D_{i,j} = 1$ if country i is within region j; otherwise, $D_{i,j} = 0$. There are all together six regions, so if $D_{i,j} = 0$ for all $j = 1, \ldots, 5$, it indicates country i is within the reference region level.

To test for wealth heterogeneity, we interact the temperature and precipitation variables with an indicator for whether a country's purchasing-power-parity adjusted (PPP) GDP per captipa is above or below the median level across countries. That is, we have the following specification

$$\begin{aligned} f_T(T_{i,t}) &= \beta_1 T_{it} + \beta_2 T_{i,t}^2 + \beta_3 (T_{i,t} \times D_{i,t}) + \beta_4 (T_{i,t}^2 \times D_{i,t}) \\ f_P(T_{i,t}) &= \gamma_1 P_{it} + \gamma_2 P_{i,t}^2 + \gamma_3 (P_{i,t} \times D_{i,t}) + \gamma_4 (P_{i,t}^2 \times D_{i,t}) \end{aligned} \tag{4.5}$$

where $D_{i,t} = 1$ for country i with below-median income level in year t.

4.3 Results

4.3.1 Descriptive Statistics

Table 4.1 summarizes the number of observations per region in our consolidated dataset. We focus on a panel of 74 countries over the period 1963-2018 (56 years), with all together 2844 country-year observations. Soybean-producing countries are concentrated the most in Southeast Asia (SEAS) and Latin America (LAC). Table 4.2 shows the number of poor and rich countries in each region. We see that WEOFF countries are all defined as rich, while SSAF consists of only 1 rich country and the other 12 poor countries. Other regions are comprised of a mix of poor and rich countries.

Figure 5.1 shows the average levels and variability of temperature indices and precipitation over two selected periods, plotted against the percentage

Table 4.1 Dataset description

Region[a]	Long name	Country-year.obs	Country.obs	Year.obs
EECA	Eastern Europe and Central Asia	363	13	56
LAC	Latin America	676	18	56
MENA	Middle East and North Africa	186	5	56
SEAS	Southeast Asia	749	15	56
SSAF	Sub-Saharan Africa	475	14	56
WEOFF	Western Europe and offshores	395	9	56
	Sum	2844	74	

[a] Refer to Figure 4.1 for detailed area definition.

Table 4.2 Number of poor and rich countries in each region

Region	Wealth Level[a]	No.Country	Country members[b]
EECA	rich	10	BIH, CZE, HRV, HUN, KAZ, MKD, ROU, RUS, SVK, SVN
	poor	3	ALB, UKR, UZB
LAC	rich	8	ARG, BRA, CHL, COL, CRI, MEX, PAN, SUR
	poor	10	BLZ, BOL, ECU, GTM, GUY, HND, NIC, PER, PRY, SLV
MENA	rich	2	JOR, TUR
	poor	3	EGY, IRN, IRQ
SEAS	rich	4	CHN, JPN, KOR, THA
	poor	11	BGD, IDN, IND, KHM, LAO, LKA, MMR, NPL, PAK, PHL, VNM
SSAF	rich	1	GAB
	poor	13	BDI, CMR, GHA, KEN, LBR, MDG, MLI, MWI, NGA, RWA, TGO, TZA, UGA
WEOFF[c]	rich	9	AUS, AUT, CAN, CHE, DEU, ESP, FRA, ITA, USA

[a] Defined as poor with below median PPP-adjusted GDP per capita at 2018, otherwise rich.
[b] Country names are indexed in Alpha-3 codes by ISO 3166 standards.
[c] All countries in WEOFF are rich, therefore no poor row is shown.

change of average soybean yields. The circle symbols represent the average levels over period one—1980 to 1999. The plus symbols represent the average levels over period two—2000 to 2019. We choose to start from 1980 instead of 1960 to account for the data availability of crop yields. Recall that we have an unbalanced dataset; the lengths of yield data history are different among countries. Choosing the first period to start from 1980 is a result of

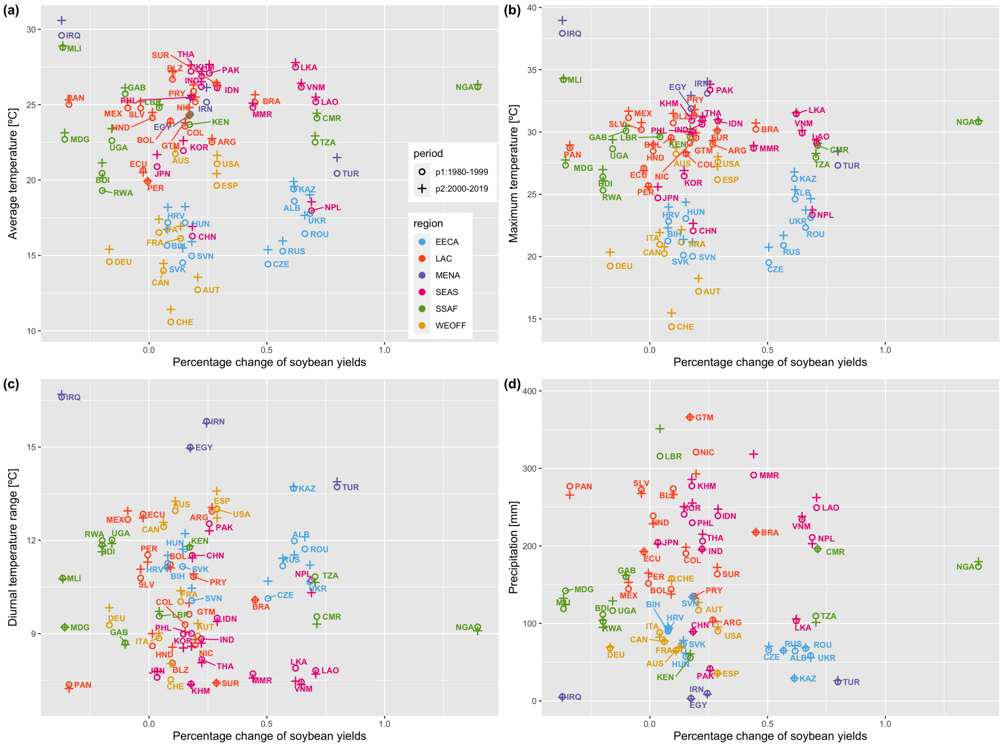

Fig. 4.2 Changes and variability in growing season temperature indices (panel (a)-(c)) and precipitation (panel (d)), plotted against percentage change of average soybean yields over two periods. Period one covers the period 1980-1999; period two covers the period 2000-2018. Average levels of climate variables are shown for the two periods, respectively (circles for period 1; pluses for period 2), against percentage change of average soybean yields over the two periods. Note that climate variables are averages over the growing season of soybeans for cropped areas in each country. Countries are colored based on regional categories.

balancing data completeness with trend visualization. To account for regional heterogeneity, we color countries based on their regional categories.

Figure 5.1 (a)(b) show that all countries get ubiquitously warmer. The largest warming is found in MENA ($1.02°C$) during the past forty years; with the smallest warming observed in LAC ($0.27°C$, Table 4.3). Moreover, the increase in maximum temperature tends to be the largest compared to average and minimum temperature, except for SEAS and SSAF, where the minimum temperature increases the most (refer to Table 4.3). Diurnal temperature range measures the difference between maximum and minimum temperature. A positive trend of diurnal temperature range shows the maximum temperature increases faster than minimum temperature, probably indicating the occurrence of heat stress or cold stress. WEOFF and EECA show a substantial rise of diurnal temperature range, on the other side, slightly decreasing trends are observed in SEAS and SSAF.

Precipitation trends vary largely across and within regions. On a regional level, an increase of precipitation is observed in EECA, SEAS, SSAF, and WEOFF (Table 4.3). The largest regional average increase is observed in SEAS; with an average increase of growing season mean precipitation of 6.77 *mm* over the past forty years, and the smallest increase of precipitation is found in WEOFF, with an average increase of 0.36 *mm*. LAC countries have large variability of precipitation trends within the region; dryer countries get more precipitation, and wet countries get less precipitation. The largest decrease in precipitation is observed in Nicaragua (NIC), with a decrease of 27.99 *mm*; on the other hand, an increase precipitation of 13.50 *mm* is observed in Peru (PER). On a global level, growing season average temperature and precipitation have increased by $0.56°C$ and 1.96 *mm* from 1980-1999 to 2000-2018, and global soybean yields have increase by 22% over the same period.

If treating all countries as a homogeneous group, panel (a)-(c) manifest no obvious patterns of temperature indices vs. yield growth rates; while panel (d) shows likely positive correlation between precipitation and yield growth, that is, in general, higher levels of annual growing season average precipitation tend to associate with higher rates of crop yields. However, if looking at individual regions separately, temperature levels could be related to crop yield growth for certain regions, such as SEAS, MENA, and LAC. For example, MENA (purple points) shows a clear negative correlation of average temperature and yield growth (panel (a)), that is, an increase of average temperature is detrimental to soybean yields. The hottest country in MENA, Iraq, which is actually also the hottest in the world, shows a substantial decrease of soybean yields. In contrast to Turkey, the coldest country in MENA, shows the most positive growth of soybean yields.

Disregarding the two outliers of China and Nepal, SEAS countries tend to have average temperature ranging from 20 to 27.5 $°C$. China and Nepal show relatively low level of temperature in soybean production areas. More than 50%

soybean production in China is from Northeast China, where the temperature is relatively low than the South Asia countries. SEAS indicates a possible nonlinear relationship. Before reaching an optimum average temperature, an increase in temperature levels leads to an increase in crop yields (see the points moving from Japan, South Korea, to Myanmar and Laos); above an optimum average temperature, an continual increase results in a reduction of crop yields (see countries with average temperature above $25°C$).

Panel (d) reveals a large spread of precipitation levels in LAC, indicating no relationship between precipitation levels and crop yield growth in this region. SEAS, on the contrary, shows a potential positive relationship between precipitation levels and yield growth. In summary, we observe pronounced regional difference in relationships between yield growth and climate variable variations; therefore, it is of essential importance to take into account regional heterogeneity in the estimation of response functions of crop yields.

Table 4.3 Descriptive statistics of changes of average climate variables from period 1980-1999 to 2000-2019. The mean statistics shows the average level of changes of climate variables within a region. The standard deviation statistics shows the variability of changes of climate variables within a region.

Region	Statistics	tmp $[°C]$	tmx $[°C]$	tmn $[°C]$	dtr $[°C]$	precip $[mm]$	Yield Growth
EECA	mean	0.969	1.107	0.832	0.275	2.590	0.389
	std	0.213	0.296	0.227	0.311	3.170	0.257
LAC	mean	0.267	0.313	0.221	0.092	−2.282	0.095
	std	0.225	0.317	0.170	0.236	10.216	0.188
MENA	mean	1.018	1.041	0.997	0.043	−0.277	0.212
	std	0.042	0.079	0.053	0.104	1.402	0.478
SEAS	mean	0.411	0.321	0.501	−0.180	6.768	0.344
	std	0.205	0.239	0.210	0.182	10.089	0.230
SSAF	mean	0.455	0.412	0.499	−0.087	3.098	0.150
	std	0.256	0.243	0.282	0.120	14.247	0.558
WEOFF	mean	0.706	0.857	0.556	0.301	0.361	0.117
	std	0.194	0.283	0.176	0.268	4.889	0.140
Global	mean	0.560	0.590	0.531	0.060	1.957	0.220
	std	0.340	0.421	0.305	0.282	9.568	0.326

[a] **Variable definition:** tmp: average temperature; tmx: maximum temperature; tmn: minimum temperature; dtr: diurnal temperature range; precip: precipitation

4.3.2 Panel Results

Response function

Table 4.4 examines the regression estimates under various model specifications. Column (1) presents results from estimating Eqn. (B.1a) for climate response under a homogeneous assumption across all countries. The global response function reveals soybean yield growth as a upward open quadratic function of temperature. Controlling for precipitation, an increase of temperature is increasingly damaging to crop yield growth until reaching a global optimum growing season temperature ($24.90°C$); above the optimum temperature the damage from a further increase of temperature is actually attenuated (as shown in Figure 4.3). One possible explanation for the diminishing negative effect of temperature increasing after a certain point could be that crop varieties at hot areas have adapted to local climate and are thereby more resilient to warming. The response function to precipitation is a parabola open downward. Fixing temperature, a dry country will benefit if it gets more precipitation until an optimal precipitation level; beyond that it is harmful to have more precipitation for a country with large amount of rain to begin with.

In column (2) we interact temperature with regional dummies. The coefficients of temperature and temperature squared represent response of the reference level, SEAS. We observe SEAS reacts strikingly different from the global homogeneous model; the signs of temperature and temperature squared are both reversed, showing a downward open quadratic response function. It indicates a warming in SEAS is increasingly beneficial before reaching an optimal temperature ($25.00°C$), after which the effects are mitigated and gradually becoming harmful as temperature increases. The coefficients on the interaction terms indicate the difference in response between SEAS and other regions. The interaction terms are statistically significant for MENA and LAC. To examine the magnitude of regional difference, we aggregate the reference response with that of the interaction terms and show the results in Table 4.5 column (2). MENA and LAC have significantly positive coefficients on temperature squared, indicating an upward open curve response function which coincides with the global temperature response function in Table 4.4 column (1). However,

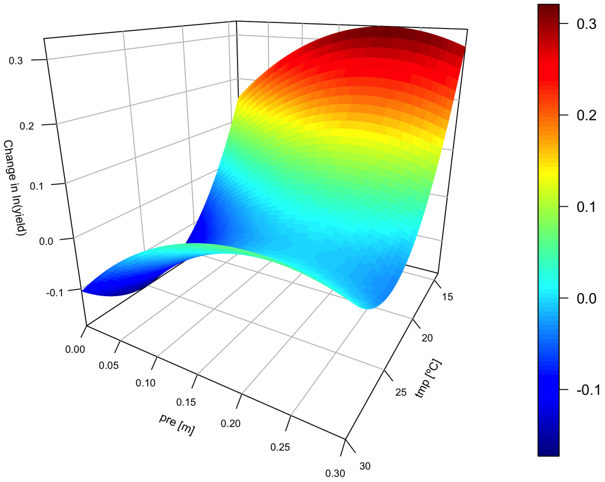

Fig. 4.3 Global response surface under homogeneous assumption across all countries. Model controls country fixed effects, year fixed effects, times trends, and diurnal temperature range.

there are many regions that can not be represented universally by the global response function. For example, SEAS has the opposite temperature–crop yield relationship; moreover, temperature is not even a significant factor to soybean yield variation in SSAF, EECA, and WEOFF.

Column (3) adds regional heterogeneity to precipitation. The regional difference of response in precipitation is significant as well. The soybean yields in SEAS, SSAF, and EECA show responsiveness to precipitation variation, while MENA, LAC, and WEOFF are insensitive to change in precipitation. Regional difference of precipitation response is not as contrasting as for temperature. Regional response function from column (3) and global response function from column (1) and (2) all show a downward open curve relationship between soybean yields and precipitation. The optimal precipitation in SEAS is 179 mm, above which level, an increase in precipitation will lead to an adverse effect to crop yields. Most countries in SEAS have precipitation level above 179 mm, indicating a negative effect on crop yields if countries get wetter. According to Figure 5.1, China, Pakistan, and Sri Lanka have lower levels of precipitation than the optimum level in SEAS, therefore they will benefit with more precipitation. However, China and Pakistan get dryer over the past forty years, indicating a detrimental effect on crop yields. Since China is colder than the optimal temperature in SEAS, historical warming has been beneficial to crop yield growth. Therefore, the negative effects of precipitation can be mitigated by the effects of temperature change in China. On the other hand, given the warm climate in Pakistan (above $25°C$), local soybean yields have experienced a double whammy from historical precipitation and temperature trends.

SSAF shows an optimal precipitation of 404 mm, which is far larger than usual values in the region (Figure 5.1 shows all MENA countries have average precipitation levels lower than 50 mm). Since it is unlikely that precipitations in MENA will jump from below 50 to above 404 mm, it is not a concern for MENA countries to experience a change of precipitation effects from positive to negative. In other words, local soybean yields will keep benefiting if precipitation increases in a foreseeable future. EECA has a linear positive relationship between precipitation and crop yields. An extra 10 mm of growing season average precipitation is associated with a 7.155 percentage points higher growth rate in EECA countries.

Column (4) examines whether rich and poor countries react differently by interacting climate variables with a wealth dummy. A country is defined as poor if it has below than median level of PPP-adjusted GDP per capita across all countries. The coefficients of the interaction terms between climate and the poor dummy are statistically insignificant, meaning that there is no significant difference in sensitivities to climate change for rich and poor countries. Table 4.5 column (4)-rich and column (4)-poor show the response estimates are indeed very similar for rich (reference level) and poor countries. Compared to poor countries, rich countries in SEAS have more concave responses to changes in temperature and precipitation (larger absolute values for the quadratic terms), with lower levels of optimal temperature and precipitation (23.42 $°C$ vs. $25.07°C$, 175 mm vs. 187 mm). Figure 4.4 (a) shows the response surface under homogeneous response assumption for rich and poor countries. Panel (b) and (c) show the response surfaces for rich and poor countries, respectively. However, the difference between poor and rich countries in SEAS is not necessarily applicable across all regions. For instance, poor countries in MENA and LAC have more convex temperature response function and lower optimal temperature values, suggesting that rich countries are less affected by temperature fluctuations (Figure 4.5).

Column (5) and (6) are lagged dependent variable models, which add 1 lag and 3 lags of log difference of soybean yields based on the model with regional heterogeneity, i.e., model (3). The parameter estimates are comparable to model (3), showing stability and robustness of the baseline model.

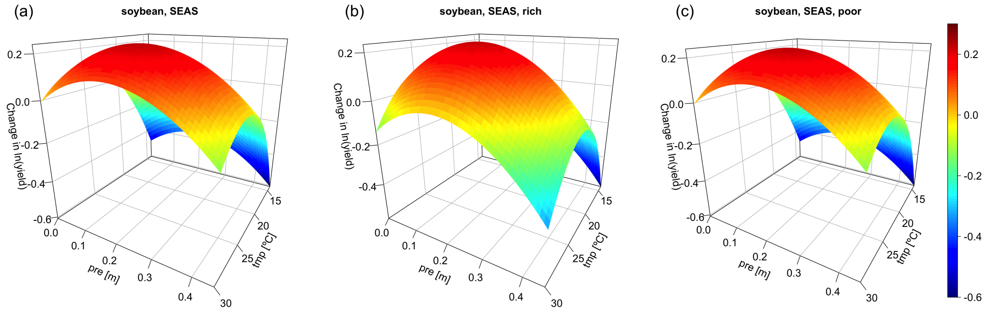

Fig. 4.4 Regional response surface for SEAS. (a) is obtained from Table 4.5 model (3), (b) is obtained from model (4)-rich, (c) is obtained from model (4)-poor.

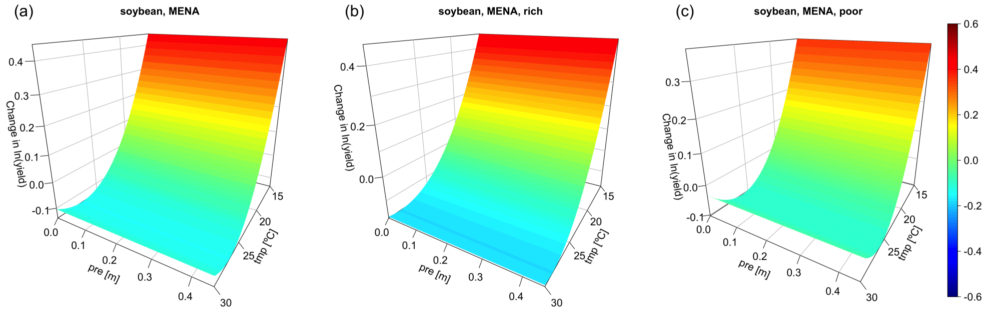

Fig. 4.5 Regional response surface for MENA. (a) is obtained from Table 4.5 model (3), (b) is obtained from model (4)-rich, (c) is obtained from model (4)-poor.

Marginal Effects

We examine here the marginal effects, that is estimating the change of crop yields from one unit's increase of climate variables. Based on the alternative model robustness check in the previous section, model (3) shows largely stability and robustness. We therefore focus on model (3) in the following analysis. Given a linear specification of diurnal temperature range, its marginal effect is just the coefficient on the variable. On a global level, one degree's increase of diurnal temperature change will result in a reduction of soybean yield growth by 4.16 percentage points (the last row of Table 4.4). In other words, if the maximum temperature increases faster than the minimum temperature, it will be significantly detrimental to soybean growth; conversely, i.e., maximum temperature increases at a slower rate, the negative effects from the rise of average temperature will be elevated.

On the other hand, we have non-linear specifications for temperature and precipitation, which means the marginal effects are a function of the climate variables. In particular the marginal effect for SEAS (the reference level) at some temperature T^* is $\beta_1 + 2\beta_2 T^*$. The marginal effects of other regions will need to aggregate the coefficients of the reference level with those of the regional interaction terms. For example, the marginal effect at temperature T^* for MENA is $\beta_1 + \beta_{1,MENA} + 2(\beta_2 + \beta_{2,MENA})T^*$. The same principle applies to precipitation. Figure 4.6 displays the effects of $1°C$ warming, using model (3). Transparent countries are not producing soybeans. White color mean the temperature is not a significant factor to soybean production in the countries. According to the result in Table 4.5, countries in SSAF, EECA, and WEOFF are not affected by temperature and thereby shown in white in the map. SEAS, except China, is estimated to be negatively affected by the warming. Actually, China will benefit the most given an increase of temperature. LAC countries differ in the responses of warming. In particular, Brazil, Paraguay, and Mexico will benefit from warming, while Columbia, Peru, Chile, and Argentina will be adversely affected by a rise of temperature.

Figure 4.7 shows the marginal effects resulting from an increase of growing season average monthly precipitation of 10 mm. We see that all countries in EECA and SSAF will benefit from additional precipitation, among which, EECA countries will benefit the most if they get wetter in the future. SEAS countries have various responses from extra precipitation—China and Pakistan will benefit, whereas Pacific island countries will be harmed.

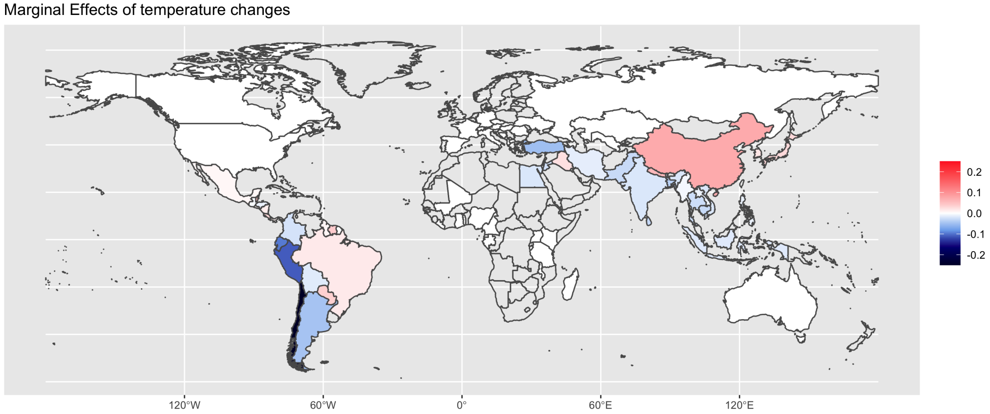

Fig. 4.6 Marginal effects of 1°C warming on soybean yields. Base temperature is the mean of the period 1961-2018 for each country. Note that the marginal effect is applied to annual growth rates. For example, a marginal effect of -0.02 means that a country growing at 3% yr^{-1} is projected to increase at 1% yr^{-1} with 1 °C warming compared to the base period.

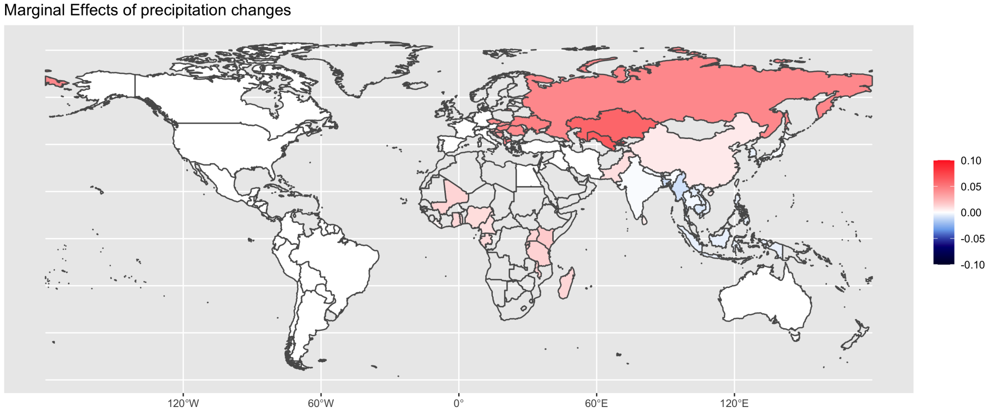

Fig. 4.7 Marginal effects of 10mm increase of annual average precipitation on soybean yields. Base precipitation is the mean of the period 1961-2018 for each country.

4.4 Discussion

This paper investigates how climate change affects soybean yields based on a panel data analysis over the period 1961-2018. We show non-linear effects of temperature and precipitation on crop yields, and a negative linear relationship for diurnal temperature range (*dtr* is the difference between maximum temperature and minimum temperature). The effects of diurnal temperature range are straightforward. On a global level an increase of $1°C$ in diurnal temperature range will reduce annual soybean yield growth by 4.1 percentage points. An increase in diurnal temperature could imply the occurrences of heat stress, where maximum temperature has increased considerably and the increment of which is larger than the rise in minimum temperature. Alternatively, the occurrences of cold stress could result in an increase of diurnal temperature as well, where minimum temperature has decreased significantly.

This paper examines the heterogeneous responses of soybean yields to changes in temperature and precipitation from two aspects: regional heterogeneity and wealth heterogeneity. We show that a global response function under a homogeneous assumption is not sophisticated enough to capture each region's distinct response to climate change because regions might have highly contrasting responses to climate change. For instance, the temperature response function in Southeast Asia is an downward open parabola and of opposite direction with that of Middle East & North Africa and Latin America. The heterogeneity among regions makes it impossible to have one global response function that is representative of all regions. We therefore incorporate regional heterogeneous parameters in our model and generate a region-specific response function for each region.

Our regional response functions show (1) Soybean yields in Southeast Asia (SEAS) are responsive to both temperature and precipitation variations. The response function of temperature is a downward open curve; before reaching an optimal growing season average temperature of $25.00°C$, an increase of temperature is increasingly beneficial to yield growth. Above the optimal level, a continual increase of temperature is less helpful to yield growth and can be even detrimental when the temperature reaches a very high level. Response function of precipitation is also a downward open curve with an optimal value of 179 mm. (2) Soybean yields in Middle East & North Africa countries (MENA) are only sensitive to changes in temperature. Its response function is an upward open quadratic curve with an optimal value of $27.03°C$. It shows the damage reaches the highest at $27.03°C$; above that, an continual warming is less harmful, probably due to the adaption of local soybean variety. Precipitation is not a significant factor to soybean growth in MENA. One possible explanation could be local agriculture is dependent on irrigation technology rather than on natural precipitation which is too low to afford the amount required for crop growing. (3) Soybean yields in Latin American countries (LAC) have similar response as MENA, with an upward open quadratic response function to temperature and are insensitive to changes in precipitation. (4) Soybean yields in Sub-Saharan Africa (SSAF) and Eastern Europe & Central Asia (EECA) are only responsive to changes in precipitation. SSAF shows an upward open curve with an optimal growing season precipitation level of 404 mm which is far greater than the common level of precipitation in the region. Therefore, an increase of precipitation will be continually beneficial before the optimum. EECA has a positive linear relationship between precipitation and crop yields. (5) Western Europe & Off Shores (WEOFF) shows non-significance to either temperature or precipitation.

At last, we explored wealth heterogeneity in our model, which shows statistically indistinguishable difference in the shape of response function between rich and poor countries. We suggest that the difference in the responses between rich and poor countries is determined by their different initial values of temperature and precipitation.

The current paper investigates the regional heterogeneity in the effects of climate change on soybean yields. We highlight that crop sensitivities to climate change are highly different, which means a global response function cannot reliably predict responses at a regional level. By interacting climate variables with regional dummies, we construct regional response functions which are able to capture local climate-agriculture dynamics. However, theses regional models should be applied with caution. For example, they are calibrated in a setting of normal climate situations in individual regions, therefore, they cannot be used to simulate future yield responses for ranges far exceeding the "normal" status. Nonetheless, this study evaluates responses of crop yields to climate change on a regional scale and provides insight to region-specific adaptation strategies to ensure food security for a growing population. One of the extensions of this study could be crop yield projection under simulated climate pathways.

Table 4.4 Regression estimate results

	(1)	(2)	(3)	(4)	(5)	(6)
Temperature	-0.1396***	0.2282**	0.2275**	0.2587**	0.3017**	0.3581**
	(0.0493)	(0.1156)	(0.1100)	(0.1174)	(0.1181)	(0.1469)
Temp. interacted with regions						
MENA		-0.3970***	-0.4465***	-0.4556***	-0.2335*	-0.2237
		(0.1194)	(0.1330)	(0.1280)	(0.1405)	(0.1873)
LAC		-0.8169***	-0.8066***	-0.8403***	-0.7197***	-0.8164***
		(0.1666)	(0.1641)	(0.1756)	(0.2168)	(0.2628)
SSAF		-0.3460	-0.3633	-0.3897*	-0.3588	-0.2748
		(0.2282)	(0.2247)	(0.2317)	(0.2290)	(0.2576)
EECA		-0.4906	-0.4431	-0.4561	-0.6013*	-0.5802
		(0.3331)	(0.3289)	(0.3329)	(0.3339)	(0.3803)
WEOFF		-0.1513	-0.1387	-0.1721	-0.1606	-0.2251
		(0.1478)	(0.1422)	(0.1487)	(0.1440)	(0.1662)
Temp. interacted with wealth indicator						
Poor country dummy				-0.0145		
				(0.0102)		
Temperature sq.	0.0028**	-0.0046**	-0.0047**	-0.0055**	-0.0066***	-0.0081***
	(0.0011)	(0.0023)	(0.0022)	(0.0024)	(0.0024)	(0.0031)
Temp. sq. interacted with regions						
MENA		0.0076***	0.0087***	0.0090***	0.0050*	0.0050
		(0.0024)	(0.0026)	(0.0025)	(0.0028)	(0.0038)
LAC		0.0167***	0.0165***	0.0173***	0.0147***	0.0166***
		(0.0034)	(0.0033)	(0.0036)	(0.0045)	(0.0056)
SSAF		0.0076	0.0082*	0.0086*	0.0076	0.0064
		(0.0050)	(0.0050)	(0.0051)	(0.0050)	(0.0057)
EECA		0.0101	0.0097	0.0099	0.0147	0.0139
		(0.0092)	(0.0090)	(0.0092)	(0.0089)	(0.0102)
WEOFF		0.0010	0.0007	0.0016	0.0017	0.0036
		(0.0037)	(0.0036)	(0.0038)	(0.0037)	(0.0041)
Temp. sq. interacted with wealth indicator						
Poor country dummy				0.0007		
				(0.0005)		
Precipitation	1.6629***	1.6703***	1.3111**	1.5153	1.2890*	1.0296
	(0.5668)	(0.5213)	(0.6072)	(1.061)	(0.7461)	(0.7697)
Precip. interacted with regions						
MENA			4.0069	0.8183	9.7328	10.7248
			(4.9513)	(9.1777)	(8.0117)	(8.3110)
LAC			-0.2644	-0.2580	-0.8283	-0.5237
			(1.0587)	(1.0548)	(1.1012)	(1.1784)
SSAF			0.5867	0.5833	0.5003	0.8150
			(0.9008)	(0.9030)	(1.1094)	(1.2708)
EECA			5.8439	5.5994	6.6400*	7.0146**
			(3.9724)	(3.9199)	(3.5694)	(3.4804)
WEOFF			-1.6633	-1.8245	-0.9620	0.7118
			(1.7000)	(1.9023)	(2.1682)	(1.6807)
Precip. interacted with wealth indicator						
Poor country dummy				-0.1657		
				(0.9601)		
Precipitation sq.	-3.9417***	-3.7974***	-3.6635***	-4.3351**	-3.3159**	-2.8125**
	(1.0455)	(0.9806)	(1.0798)	(2.2008)	(1.3563)	(1.3507)
Precip. sq. interacted with regions						
MENA			-105.5973	-52.3802	-140.3026	-188.8467
			(83.6933)	(155.9143)	(134.3376)	(136.4317)
LAC			1.0621	1.0413	2.0815	1.8493
			(1.9643)	(1.9961)	(2.0239)	(2.1264)
SSAF			1.3133	1.1965	1.2448	0.6111
			(1.5034)	(1.5186)	(1.9045)	(2.1070)
EECA			-17.5161	-16.3583	-12.7286	-16.7581
			(14.8302)	(14.6370)	(14.1649)	(13.6104)
WEOFF			9.7483	10.2720	6.8844	1.6497
			(7.4054)	(7.7373)	(8.9362)	(7.0024)
Precip. sq. interacted with wealth indicator						
Poor country dummy				0.7356		
				(2.1986)		
Diurnal temperature range	-0.0482***	-0.0445***	-0.0418***	-0.0409***	-0.0341**	-0.0324**
	(0.0147)	(0.0146)	(0.0141)	(0.0143)	(0.0134)	(0.0141)
Observations	2844	2844	2844	2844	2690	2454
R squared	0.2	0.21	0.22	0.22	0.23	0.23

All models include country fixed effects, year fixed effects, and quadratic time trends. Temperature is measured in °C and precipitation in metres, expressed as average values on growing seasons of soybeans. Dependent variable is log difference of crop yields. Columns: (1) homogeneous specification as baseline regression, (2) baseline plus regional heterogeneity for temperature, (3) baseline plus regional heterogeneity for temperature and precipitation, (4) as in column 3 but adding wealth heterogeneity, (5) as in column 3 but adding 1 lag of dependent variable, (6) as in column 3 but adding 3 lags of dependent variable. Asterisks indicate significance at 1%(***), 5%(**), and 10%(*).

Table 4.5 Climate Effects based on regional heterogeneity.

Region	Term	(2)	(3)	(4)-rich	(4)-poor
SEAS	Temp.	0.2282**	0.2275**	0.2587***	0.2442**
		(0.1156)	(0.1100)	(0.1174)	(0.1136)
	Temp. sq.	-0.0046**	-0.0047**	-0.0055**	-0.0049**
		(0.0023)	(0.0022)	(0.0024)	(0.0023)
	Optimal Temp.	25.00	24.23	23.42	25.07
	Precip.		1.3111**	1.5153	1.3497**
			(0.6072)	(1.0610)	(0.5977)
	Precip. sq.		-3.6635***	-4.3351**	-3.5995***
			(1.0798)	(2.2008)	(1.0658)
	Optimal Precip.		0.179	0.175	0.187
MENA	Temp.	-0.1688***	-0.219***	-0.1969***	-0.2114***
		(0.0397)	(0.0690)	(0.0712)	(0.0666)
	Temp. sq.	0.0031***	0.0041***	0.0034 **	0.0041***
		(0.0008)	(0.0013)	(0.0015)	(0.0012)
	Optimal Temp.	27.41	27.03	28.68	25.86
	Precip.		5.3181	2.3336	2.1679
			(4.9771)	(8.7574)	(9.3176)
	Precip. sq.		-109.2607	-56.7152	-55.9796
			(83.7818)	(155.1197)	(156.2028)
LAC	Temp.	-0.5887***	-0.5791***	-0.5816***	-0.5961***
		(0.1199)	(0.1192)	(0.1196)	(0.1201)
	Temp. sq.	0.0121***	0.0118***	0.0117***	0.0124***
		(0.0024)	(0.0024)	(0.0024)	(0.0024)
	Optimal Temp.	24.34	24.52	24.79	24.07
	Precip.		1.0467	1.2573	1.0917
			(0.8783)	(1.3750)	(0.8980)
	Precip. sq.		-2.6014	-3.2938	-2.5582
			(1.6788)	(3.0679)	(1.6303)
SSAF	Temp.	-0.1178	-0.1359	-0.131	-0.1455
		(0.1972)	(0.1965)	(0.2034)	(0.2027)
	Temp. sq.	0.003	0.0035	0.0031	0.0037
		(0.0045)	(0.0045)	(0.0047)	(0.0046)
	Precip.		1.8978***	2.0986*	1.9329***
			(0.6632)	(1.1778)	(0.6699)
	Precip. sq.		-2.3501**	-3.1385	-2.403***
			(1.0303)	(2.4787)	(1.0416)
	Optimal Precip.		0.404	0.334	0.402
EECA	Temp.	-0.2624	-0.2156	-0.1974	-0.2119
		(0.3134)	(0.3114)	(0.3192)	(0.3187)
	Temp. sq.	0.0055	0.005	0.0044	0.0051
		(0.0089)	(0.0088)	(0.0090)	(0.0090)
	Precip.		7.155*	7.1148*	6.9491*
			(3.9246)	(3.9782)	(3.8500)
	Precip. sq.		-21.1796	-20.6933	-19.9577
			(14.7866)	(14.8264)	(14.5611)
WEOFF	Temp.	0.0769	0.0887	0.0866	0.0721
		(0.0869)	(0.0859)	(0.0857)	(0.0862)
	Temp. sq.	-0.0036	-0.004	-0.0039	-0.0033
		(0.0027)	(0.0027)	(0.0027)	(0.0028)
	Precip.		-0.3521	-0.3092	-0.4749
			(1.5970)	(1.6027)	(1.8406)
	Precip. sq.		6.0849	5.937	6.6725
			(7.3048)	(7.3347)	(7.7207)

This table aggregates climate-region and climate-wealth interaction terms based on model specifications in Table 4.4. Temperature is measured in °C and precipitation in metres, expressed as average values on growing seasons of soybeans. Asterisks indicate significance at 1%(***), 5%(**), and 10%(*).

References

Burke, M., Hsiang, S. M., and Miguel, E. (2015). Global non-linear effect of temperature on economic production. *Nature*, 527(7577):235–239.

Carleton, T. A. and Hsiang, S. M. (2016). Social and economic impacts of climate.

Dell, M., Jones, B. F., and Olken, B. A. (2012). Temperature shocks and economic growth: Evidence from the last half century. *American Economic Journal: Macroeconomics*, 4(3):66–95.

Diffenbaugh, N. S. and Burke, M. (2019). Global warming has increased global economic inequality. *Proceedings of the National Academy of Sciences of the United States of America*, 116(20):9808–9813.

Harris, I., Osborn, T. J., Jones, P., and Lister, D. (2020). Version 4 of the CRU TS monthly high-resolution gridded multivariate climate dataset. *Scientific Data*, 7(1).

IPCC AR5 (2014). AR5 Climate Change 2014: Impacts, Adaptation, and Vulnerability. *Fifth Assessment Report of the Intergovernmental Panel on Climate Change.*

Liu, B., Asseng, S., Müller, C., Ewert, F., Elliott, J., Lobell, D. B., Martre, P., Ruane, A. C., Wallach, D., Jones, J. W., Rosenzweig, C., Aggarwal, P. K., Alderman, P. D., Anothai, J., Basso, B., Biernath, C., Cammarano, D., Challinor, A., Deryng, D., De Sanctis, G., Doltra, J., Fereres, E., Folberth, C., Garcia-Vila, M., Gayler, S., Hoogenboom, G., Hunt, L. A., Izaurralde, R. C., Jabloun, M., Jones, C. D., Kersebaum, K. C., Kimball, B. A., Koehler, A. K., Kumar, S. N., Nendel, C., O'Leary, G. J., Olesen, J. E., Ottman, M. J., Palosuo, T., Prasad, P. V., Priesack, E., Pugh, T. A., Reynolds, M., Rezaei, E. E., Rötter, R. P., Schmid, E., Semenov, M. A., Shcherbak, I., Stehfest, E., Stöckle, C. O., Stratonovitch, P., Streck, T., Supit, I., Tao, F., Thorburn, P., Waha, K., Wall, G. W., Wang, E., White, J. W., Wolf, J., Zhao, Z., and Zhu, Y. (2016). Similar estimates of temperature impacts on global wheat yield by three independent methods. *Nature Climate Change*, 6(12):1130–1136.

Lobell, D. B. and Asseng, S. (2017). Comparing estimates of climate change impacts from process-based and statistical crop models. *Environmental Research Letters*, 12(1):15001.

Lobell, D. B. and Burke, M. B. (2010). On the use of statistical models to predict crop yield responses to climate change. *Agricultural and Forest Meteorology*, 150(11):1443–1452.

Lobell, D. B., Burke, M. B., Tebaldi, C., Mastrandrea, M. D., Falcon, W. P., and Naylor, R. L. (2008). Prioritizing climate change adaptation needs for food security in 2030. *Science*, 319(5863):607–610.

Lobell, D. B. and Field, C. B. (2007). Global scale climate-crop yield relationships and the impacts of recent warming. *Environmental Research Letters*, 2(1):14002–14009.

Monfreda, C., Ramankutty, N., and Foley, J. A. (2008). Farming the planet: 2. Geographic distribution of crop areas, yields, physiological types, and net primary production in the year 2000. *Global Biogeochemical Cycles*, 22(1).

Rosenzweig, C., Jones, J. W., Hatfield, J. L., Ruane, A. C., Boote, K. J., Thorburn, P., Antle, J. M., Nelson, G. C., Porter, C., Janssen, S., Asseng, S., Basso, B., Ewert, F., Wallach, D., Baigorria, G., and Winter, J. M. (2013). The Agricultural Model Intercomparison and Improvement Project (AgMIP): Protocols and pilot studies. *Agricultural and Forest Meteorology*, 170:166–182.

Sacks, W. J., Deryng, D., Foley, J. A., and Ramankutty, N. (2010). Crop planting dates: An analysis of global patterns. *Global Ecology and Biogeography*, 19(5):607–620.

Zhang, Z., Wang, P., Chen, Y., Song, X., Wei, X., and Shi, P. (2014). Global warming over 1960-2009 did increase heat stress and reduce cold stress in the major rice-planting areas across China. *European Journal of Agronomy*, 59:49–56.

Zhao, C., Liu, B., Piao, S., Wang, X., Lobell, D. B., Huang, Y., Huang, M., Yao, Y., Bassu, S., Ciais, P., Durand, J. L., Elliott, J., Ewert, F., Janssens, I. A., Li, T., Lin, E., Liu, Q., Martre, P., Müller, C., Peng, S., Peñuelas, J., Ruane, A. C., Wallach, D., Wang, T., Wu, D., Liu, Z., Zhu, Y., Zhu, Z., and Asseng, S. (2017). Temperature increase reduces global yields of major crops in four independent estimates. *Proceedings of the National Academy of Sciences of the United States of America*, 114(35):9326–9331.

CHAPTER 5

The Relative Role of Temperature and Precipitation in Global Economic Growth

Working Paper with Thomas Leirvik[1] and Hande Karabiyik[2]

[1] *Nord University Business School, Norway*
[2] *Vrije Universiteit Amsterdam, Netherlands*

Abstract

Global warming has slowed economic growth and aggravated global economic inequality, affecting individual wellbeing in a wide range of aspects. Quantifying these historical impacts is critical for informing climate change mitigation and adaptation and achieving a more equitable economic development. This paper extends existing literature by exploring the effects of precipitation on economic growth. Based on a panel of 169 countries over the period 1961-2019, we demonstrate a statistically significant non-linear effect of precipitation on economic growth, such that output is maximized at around 2.03 metres of annual total precipitation. Despite of the significant sensitivity of precipitation, we find its impacts are relatively small and are completely overwhelmed by the effects of temperature. We examine the historical marginal effects of climate change and find realized temperature has lowered the annual global growth rate by 0.31 percentage points year^{-1} on average, while realized precipitation has increased the annual economic growth by roughly 0.01 percentage points year^{-1}. Furthermore, we highlight that countries endowed with different climate conditions exhibit considerably different responses to historical climate change. For example, European and Central Asian countries have benefited both from temperature rising and precipitation fluctuations; while adverse impacts have been observed for both factors in African countries where climate has been warmer and dryer. Theses findings suggest the importance of precipitation for countries with vulnerable ecosystems and inform the possibility of incorporating precipitation in economic development projections under future climate trajectories.

5.1 Introduction

Global warming due to greenhouse gas emissions are well-documented and predicted to be persistent until middle of the century under an intermediate emission mitigation pathway which aims to stabilize global temperature change below $2°C$ (or RCP 4.5 by IPCC AR5, 2014). Growing evidence has demonstrated that a rising of global average temperature has wide-ranging impacts on human societies, including agricultural, industrial output, ecosystem, public health, etc. (see e.g., Dell et al., 2014; Carleton and Hsiang, 2016; Auffhammer, 2018). Predominantly negative impacts have been documented, and even larger impacts are predicted for the future. In this paper, we focus on the effects of climate change on aggregate economic output, which measures the overall productivity in a society and has a direct impact on individual well-being. Measuring and quantifying theses historical impacts is of critical importance for planning economic adaptation and climate mitigation.

In recent studies, panel data analyses are extensively employed for estimating economic damages associated with climate change. Panel approaches have significant advantages over cross-section analyses not only because they allow data to expand both in countries and in time but also the individual fixed effects are able to control for time-invariant national characteristics such as history, culture, topography, institutional qualities, etc. On the other hand, cross-section analyses use only contemporary country data to examine the relationship between temperature and economic outcomes. Given that hot countries tend to be poor and cold countries tend to be rich, many argues that the temperature-economic growth relationship revealed by cross-section analyses are spurious because temperature is associated with certain country characteristics, such as wealth level (e.g., Rodrik et al., 2004; Dell et al., 2012). We here combine historical observations of climate variables and economic outputs for 169 countries over the period 1961-2019. Based on the constructed panel, we estimate and make inference of economic responses to historical climate change.

The fixed country and year effects panel model is most applied in literature (e.g., Lobell and Burke, 2010; Burke et al., 2015; Diffenbaugh and Burke, 2019), with country-specific effects representing time-invariant factors that influence economic growth, and year-specific effects representing abrupt global shocks, such as global recessions or financial crises. Furthermore, prevailing studies assume independence between country-specific and year-specific effects, which can be estimated by an additive fixed effects model. However, there is evidence to believe that the extent to which the individuals are affected by the common global shocks can be different. For example, shocks to energy market can be more influential to economic growth in resource-based countries, such as Saudi Arabia, Kuwait, the economies of which are highly dependent on exporting oil and gas. In this paper, in addition to the additive fixed effects model, we also apply a novel statistical model—interactive fixed effects model, which allows heterogeneity to enter the model in a multiplicative way. We compare the estimation results under the two models and inform how economies are impacted by historical climate change.

Although the effects of temperature have been extensively investigated in the literature, the role of precipitation has been overlooked and rarely discussed. The effects of precipitation remain unclear because unlike the consistent and ubiquitous global warming, precipitation has been highly volatile and found no evidence of pervasive long-term trends globally (Dell et al., 2012; Burke et al., 2015). Among the few literature that considered the effects of precipitation, Dell et al. (2012) claimed significant precipitation sensitivity for rich countries but found no sensitivity for poor countries. Burke et al. (2015) further reported no significance of precipitation in a global homogeneous response function. However, by implementing a time-series unit root test, we retain only countries with stationary GDP growth, and based on the stationary panel, we find statistically significant non-linear relationship between precipitation and economic growth. Our framework enables a three-dimensional response surface of economic growth, that is, economic growth varies as temperature and precipitation change. Furthermore, we estimate historical influence of evolution of temperature and precipitation on a country level and find differing results worldwide. For instance European and Central Asian countries have benefited from both the temperature and precipitation trends, while a double whammy, i.e. damages from both temperature and precipitation variation, has been observed in Africa.

This paper proceeds as follows. Section 2 describes the data and model applied in the paper. Section 3 summarizes empirical results from panel regressions. Section 4 discusses results.

5.2 Data and Method

5.2.1 Data

Temperature and precipitation data are obtained from Climate Research Unit Time Series (CRU-TS V4.0, Harris et al., 2020), which provides monthly average temperature and total precipitation data for each 0.5° × 0.5° cell on the globe over the period 1900-2019. We aggregate the 0.5° grid cell climate estimates to country level, weighting by population density in year 2000 using data from the Gridded Population of the World (CIESIN, 2000).

GDP per capita data are available from the World Bank's World Development Indicators dataset (WDI, 2020), which contains worldwide country level economic development measures between the years 1961-2019. To ensure comparability of the values of economic outcomes in the history, we use constant 2010 US$ GDP per capita. Our full dataset is comprised of 8055 country-year observations over the period 1961-2019.

5.2.2 Econometric Model

Suppose that we have the panel data variable $y_{i,t}$ that follows the DGP,

$$y_{i,t} = \boldsymbol{\beta}'\mathbf{x}_{i,t} + u_{i,t}, \tag{5.1}$$

where $\mathbf{x}_{i,t}$ is a $k-$vector of variables and $\boldsymbol{\beta}$ is a $k-$vector of coefficients. This is a homogeneous panel data model. The assumptions we make about $u_{i,t}$ will determine the presence and the nature of unobserved heterogeneity that is allowed.

FE. Individual and time fixed effects.

$$u_{i,t} = \mu_i + \nu_t + \varepsilon_{i,t}. \tag{5.2}$$

Here μ_i is the individual fixed effects term that represent the unobserved heterogeneity across cross-section units and ν_t is the fixed time effects that represent the unobserved heterogeneity across time. The term ν_t stands for the shocks that are fixed across cross-section units. In this assumption, we allow the terms that represent unobserved heterogeneity to enter the model in a additive way. For this reason, Bai (2009) called this model "additive effects model".

IE. Interactive fixed effects.

$$u_{i,t} = \boldsymbol{\lambda}_i'\mathbf{f}_t + \varepsilon_{i,t}. \tag{5.3}$$

Here $\mathbf{f}_t$ are $r-$vector of common global shocks that might affect all countries and the $r-$vector λ_i are the individual specific loadings. They represent the extent to which the individuals are affected by the common global shocks. This assumptions is more general than the FE assumption and it allows the unobserved heterogeneity to enter the model in a multiplicative way. Note that by restricting $\boldsymbol{\lambda}_i = (1, \mu_i)'$ and $\mathbf{f}_t = (\nu_t, 1)'$, we can obtain the FE model back.

Accurate estimation and inference of $\boldsymbol{\beta}$ in (5.1) depends on what we assume about $u_{i,t}$. If we assume FE, then we can use classical methods to estimate the (5.1). For instance, we can define

$$\overline{y}_{i,.} = \frac{1}{T}\sum_{t=1}^{T} y_{i,t}, \quad \overline{y}_{.,t} = \frac{1}{N}\sum_{i=1}^{N} y_{i,t}, \quad \overline{y}_{.,.} = \frac{1}{NT}\sum_{i=1}^{N}\sum_{t=1}^{T} y_{i,t}$$

and let

$$\tilde{y}_{i,t} = y_{i,t} - \overline{y}_{i,.} - \overline{y}_{.,t} + \overline{y}_{.,.}.$$

We can rewrite (5.1)-(5.2)

$$\tilde{y}_{i,t} = \boldsymbol{\beta}'\tilde{\mathbf{x}}_{i,t} + \tilde{\varepsilon}_{i,t}, \tag{5.4}$$

where $\tilde{\mathbf{x}}_{i,t}$ and $\tilde{\varepsilon}_{i,t}$ are defined similarly to $\tilde{y}_{i,t}$. This transformation of the model eliminated the fixed effects from the model. We can estimate (5.4) by pooled OLS. This is called the within estimator.

An accurate estimation method under the assumption IE is proposed by Bai (2009). The difficulty comes from the fact that both $\mathbf{f}_t$ and $\boldsymbol{\lambda}_i$ are unobserved and cannot be eliminated from the model by transformations of the variables alone. Hence the component $\boldsymbol{\lambda}_i'\mathbf{f}_t$ needs to be estimated. Bai (2009) proposes an iterative principal components based approach. Given an initial estimate for $\boldsymbol{\beta}$, say $\widehat{\boldsymbol{\beta}}$, we can write

$$\widehat{u}_{i,t} = y_{i,t} - \widehat{\boldsymbol{\beta}}'\mathbf{x}_{i,t}$$

we and initial estimate of $\mathbf{f}_t$, say $\widehat{\mathbf{f}}_t$ can be taken as the r largest eigenvectors of $\sum_{i=1}^{N} \widehat{\mathbf{U}}_i\widehat{\mathbf{U}}_i'$, where $\widehat{\mathbf{U}}_i = (u_{i,1}, \ldots, u_{i,T})'$ is the $T-$ vector of residuals. An initial estimator for the loadings can be obtained by

$$\widehat{\lambda}_i = T^{-1}\widehat{\mathbf{F}}'(\mathbf{Y} - \mathbf{X}\widehat{\boldsymbol{\beta}})$$

with obvious definitions for $\widehat{\mathbf{F}}$, $\mathbf{Y}$ and $\mathbf{X}$. Once $\widehat{\mathbf{f}}_t$ and $\widehat{\lambda}_i$ are obtained, a second step estimator for $\widehat{\boldsymbol{\beta}}$ can be obtained by estimating

$$y_{i,t} = \boldsymbol{\beta}'\mathbf{x}_{i,t} + \widehat{\lambda}_i'\widehat{\mathbf{f}}_t + error \tag{5.5}$$

Then a second step of residuals can be obtained, which can be used again to obtain second set of estimators for $\mathbf{f}_t$ and $\boldsymbol{\lambda}_i$. This process continues until convergence. The resulting estimator for $\boldsymbol{\beta}$ has very good properties under certain assumptions. This procedure is explained in detail in Bai (2009).

5.3 Empirical Results

5.3.1 Dataset description

Figure 5.1 shows the level and variability of temperature and precipitation over the period 1961-2019. The average values for three decades are shown in circles with different colors: 1966-1975 in red, 1986-1995 in green, and 2006-2015 in blue. The grey lines indicate the range of annual temperature/precipitation over the whole period 1961-2019. Panel (a) shows pervasive warming trends of temperature; moreover, a large part of the countries show a rising of temperature at accelerating rates. In other words, for each country the three circles are ordered chronologically, and in an accelerated warming situation the green circle (mean of 1986-1995) is closer to the red circle (mean of 1966-1975). For instance, the green and red circle actually overlap for Greenland (GRL), which means although temperature barely changed during 1966-1995, temperature has increased sharply since 1995. There also exist a few countries with a slow down of warming, such as Zambia (ZMB) and Honduras (HND), the green circles of which are closer to the blue circles. The figure further shows the cooler countries exhibit larger magnitude of the rise of temperature and larger variability than warmer countries. Panel (a) suggests a probably negative relationship between the level of annual temperature and the level of GDP per capita. If disregarding the oil-based countries in the Middle East, such as United Arab Emirates, United Arab Emirates, United Arab Emirates, the wealthiest countries tend to be located in Western Europe and are cooler than the poorest countries which are clustered in Africa.

Panel (b) shows no evident long-term trends of precipitation, and precipitation varies largely across the years especially for countries with large precipitation. We cannot conclude any clear relationship between the level of precipitation and the level of per capita income in 2015.

5.3.2 Empirical Estimation

We apply the specification in Burke et al. (2015) as a baseline for the additive effects model:

$$\Delta \log y_{i,t} = \beta_1 T_{i,t} + \beta_2 T_{i,t}^2 + \gamma_1 P_{i,t} + \gamma_2 P_{i,t}^2 + \theta_{1,i} t + \theta_{2,i} t^2 + \mu_i + \nu_t + \varepsilon_{i,t}, \quad (5.6)$$

where T is temperature and P is precipitation and y is GDP per capita. This model assumes an additive model for the error component (See previous section) and can be estimated by using a within estimator.

There are reasons to believe that an additive structure might not be able to explain fully the unobserved heterogeneity. For this reason we allow for

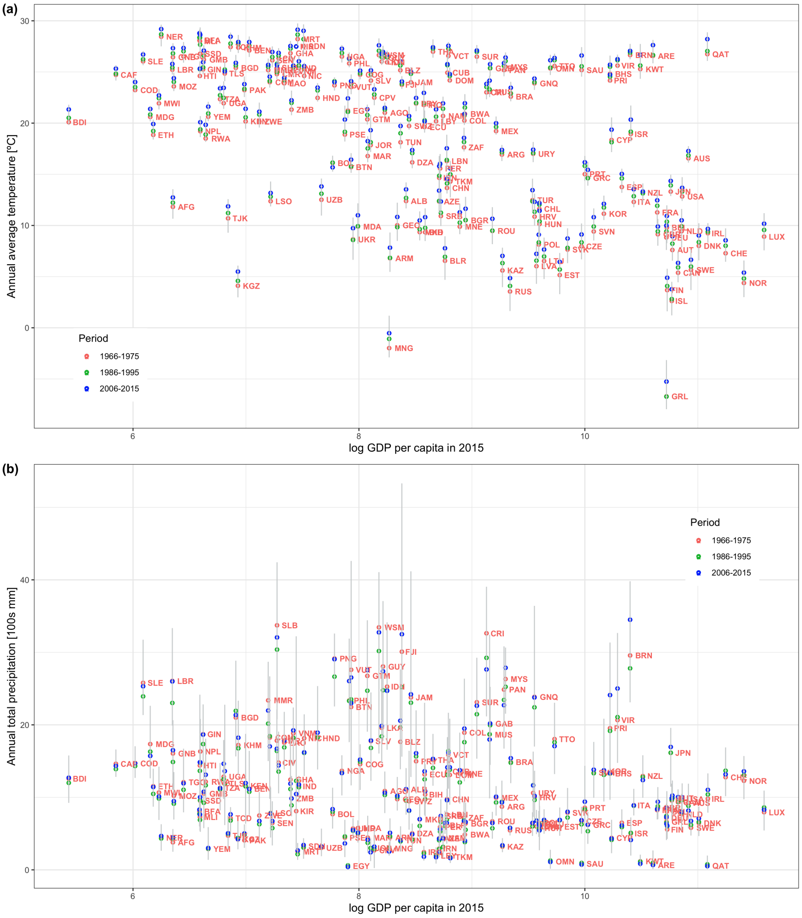

Fig. 5.1 Changes in temperature and precipitation.

interactive fixed effects in the model and consider

$$\Delta \log y_{i,t} = \beta_1 T_{i,t} + \beta_2 T_{i,t}^2 + \lambda_1 P_{i,t} + \lambda_2 P_{i,t}^2 + \theta_{1,i} t + \theta_{2,i} t^2 + + \boldsymbol{\lambda}_i' \mathbf{f}_t + \varepsilon_{i,t}. \quad (5.7)$$

The only difference here compared to (5.6) is the additional term $\boldsymbol{\lambda}_i' \mathbf{f}_t$. We can estimated this model by the method proposed by Bai (2009). This method requires an estimation of the number of factors, r. There are methods to estimate the number of factors. For now, we assume $r = 4$.

Stationary test

A stationary panel is essential to ensure a standard limiting distribution and therefore a robust inference for parameters. Panel test for unit roots are more powerful than the time series unit root tests. However, they take the panel as a whole and do not distinguish between the stationary and non-stationary time series within the panel. In this section, we investigate the unit root and trend properties of the variables.

GDP growth is often assumed to be stationary. A graphical investigation of the GDP growths of the countries that we have in our panel shows that most countries are affected by global financial economic crises and/or local political instabilities. These lead to structural breaks in the GDP growth series. Table 5.1 summarizes the time-series unit root test results. When we employ Phillips-Perron unit root test we find that 13 countries are trend stationary, 110 countries are stationary. The remaining 46 countries exhibit non-stationary GDP growth. This is unexpected and probably due to the short T dimension. This can also be because of the unaccounted structural breaks in the series. Indeed, when we employ Zivot-Andrews unit root test that allows for one structural break in the series to these 46 series, we find that we reject the null of unit root for 19 of these 46 series. The remaining 27 series still do not provide enough evidence to conclude stationarity. Temperature series are dominantly stationary, 149 trend stationary series and 15 stationary series. Precipitation series looks less persistent, with 6 trend stationary and 163 stationary and no non-stationary series.

Table 5.1 Unit root test for country time series. This table summarizes the number of countries passing various types of time series unit root tests.

	Phillips-Perron test			Zivot-Andrews test
	Trend Stationary	Stationary	Non-stationary	Non-stationary
GDP per capita	13	110	46	27
Temperature	149	15	5	1
Precipitation	6	163	0	0

Panel unit root tests are more powerful than time-series unit root test. Which means they have better ability to reject a null hypothesis when the null hypothesis is not correct. However, we can only draw one conclusion from panel unit root test: either the whole panel is non-stationary or the whole panel is stationary. We employ the CIPS test of Pesaran, which allows for cross-sectional dependence. Table 5.2 shows the test rejects the null hypothesis, indicating a stationary panel.

Table 5.2 Panel unit root test for the full dataset

	IPS test			CIPS test		
	None	Drift	Trend	None	Drift	Trend
GDP per capita	−2.563	−3.315	−3.557	−2.951	−3.235	−0.542
Temperature	0.382	−2.454	−4.828	−1.877	−3.250	−3.314
Precipitation	−0.509	−5.908	−5.238	−4.829	−4.977	−5.121

Notes: The IPS and CIPS tests are conducted by using a lag order of 2. IPS test is the Im-Pesaran-Shin test that does not allow for cross-sectional dependence. CIPS test allows for cross-sectional dependence. The numbers given in the table are test statistics. Critical values are tabulated in the corresponding papers. "None" is for the model $y_t = \rho_1 y_{t1} + \rho_2 y_{t2} + u_t$, "Drift" is for the model $y_t = \mu + \rho_1 y_{t1} + \rho_2 y_{t2} + u_t$ and "Trend" is for the model $y_t = \mu + \delta t + \rho_1 y_{t1} + \rho_2 y_{t2} + u_t$.

Panel results

The panel unit root tests allow us to conclude stationarity. However from the time series unit root tests, we see that we do not have enough evidence to reject the null hypothesis of unit root in the GDP growth for some countries. In order to see if this finding effects our regression estimation results, we group the countries into two: (i) countries with stationary of trend stationary GDP growths, (ii) countries with unit root GDP growths. We estimate the regression model for these two groups separately. Table 5.3 and Table 5.4 show strikingly different estimation results for countries with stationary and non-stationary GDP growth.

Countries with stationary GDP growth show statistically significant non-linear sensitivities to temperature and precipitation (Table 5.3). Both temperature and precipitation show a downward open parabolic relationship with GDP growth. It indicates that before reaching the optimal value of climate variables, an increase of temperature/precipitation is beneficial to economic development; beyond the optimal level, a continual increase is detrimental. The estimates from additive fixed effects (FE) and interactive fixed effects

(IE) are similar, while the FE model has a more concave response surface to climate change (the FE model has larger sensitivitives to the squared terms of temperature and precipitation). Moreover, the IE model reveals more optimistic (larger) optimums for temperature and precipitation: 14.74 vs. $13.34^{\circ}C$ (IE vs. FE) and 2.025 vs. 2.022 metres (IE vs. FE). Figure 5.2 further confirms that the prospect under an extreme warming scenario is less pessimistic for the IE model (panel (b)) than that of the FE model (panel (a)). The FE model predicts substantial decreasing of GDP growth rates when the annual average temperature rises to $25^{\circ}C$ and beyond. The figure also shows that compared to precipitation, temperature is the dominant factor affecting GDP growth.

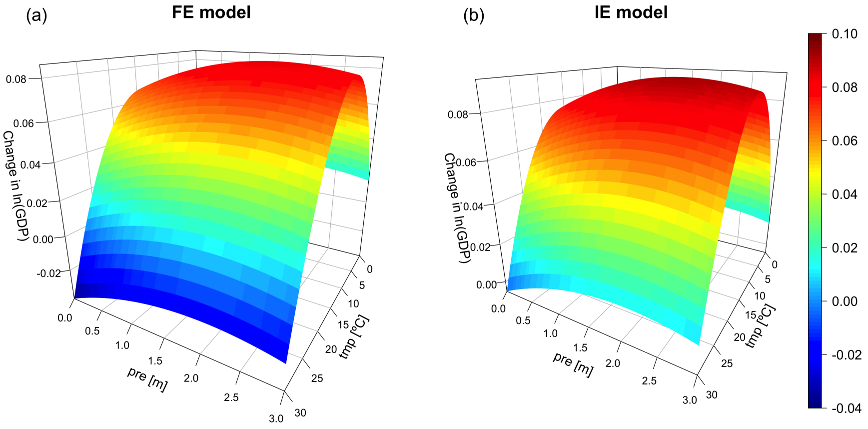

Fig. 5.2 Changes in $\log(GDP)$ with respect to changes in annual average temperature (in $^{\circ}C$) and annual total precipitation (in metres).

On the other hand, Table 5.4 shows a linear relationship between temperature and GDP growth for the non-stationary countries. However, since OLS estimation is spurious for a non-stationary panel, we cannot conclude the deterministic role of temperature.

Based on the estimation results of the stationary panel, we calculate realized impacts of historical temperature change, precipitation change, and the sum of both changes for each country over the period 1961-2019. Denote $T_{i,\overline{1961}}$ as the average temperature in country i between 1961-1970 (the first decade in the panel), and $T_{i,\overline{2019}}$ as the average temperature over 2010-2019 (the last decade

Table 5.3 Stationary GDP growth

	Coefficient	Std error	T-value	P-value	Sigfn
	Additive fixed effects				
temperature	0.01014	0.00258	3.93080	0.00009	***
temperature sq.	-0.00038	0.00010	-3.93550	0.00008	***
precipitation	0.01804	0.00781	2.31090	0.02087	**
precipitation sq.	-0.00446	0.00150	-2.97810	0.00291	***
	Interactive fixed effects				
temperature	0.01032	0.00239	4.32454	0.00001	***
temperature sq.	-0.00035	0.00009	-3.95599	0.00004	***
precipitation	0.01705	0.00708	2.40652	0.00805	***
precipitation sq.	-0.00421	0.00159	-2.65389	0.00398	***

[a] Asterisks indicate significance at 1%(***), 5%(**), and 10%(*).

[b] Temperature is measured in °C, representing for annual average temperature. Precipitation is measured in metres, standing for annual total precipitation.

Table 5.4 Non-stationary GDP growth

	Coefficient	Std error	T-value	P-value	Sigfn
	Additive fixed effects				
temperature	0.03313	0.01616	2.05000	0.04056	**
temperature sq.	-0.00080	0.00053	-1.51600	0.12974	
precipitation	-0.00605	0.01977	-0.30630	0.75939	
precipitation sq.	0.00002	0.00491	0.00430	0.99657	
	Interactive fixed effects				
temperature	0.00884	0.00757	1.16674	0.12166	
temperature sq.	-0.00029	0.00026	-1.10432	0.13473	
precipitation	-0.00474	0.02476	-0.19151	0.42406	
precipitation sq.	0.00007	0.00600	0.01181	0.49529	

in the panel). The realized impacts can be estimated as

$$\begin{aligned}\delta_{i,T} &= \beta_1(T_{i,\overline{2019}} - T_{i,\overline{1961}}) + \beta_2(T^2_{i,\overline{2019}} - T^2_{i,\overline{1961}}) \\ \delta_{i,P} &= \beta_1(P_{i,\overline{2019}} - P_{i,\overline{1961}}) + \beta_2(P^2_{i,\overline{2019}} - P^2_{i,\overline{1961}})\end{aligned} \tag{5.8}$$

where $\delta_{i,T}$ and $\delta_{i,P}$ represent additional impacts of temperature and precipitation on annual GDP growth, respectively. The total effects of temperature and precipitation are the sum of $\delta_{i,T}$ and $\delta_{i,P}$.

Figure 5.3 displays the accumulated economic effects of historical temperature/precipitation over the period 1961-2019 and the total effects of both changes

(a) FE-temperature effects **(b)** IE-temperature effects

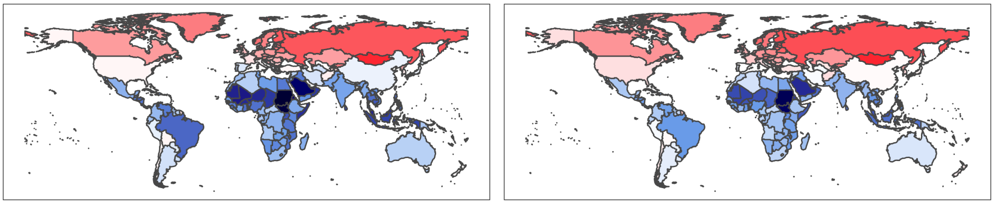

(c) FE-precipitation effects **(d)** IE-precipitation effects

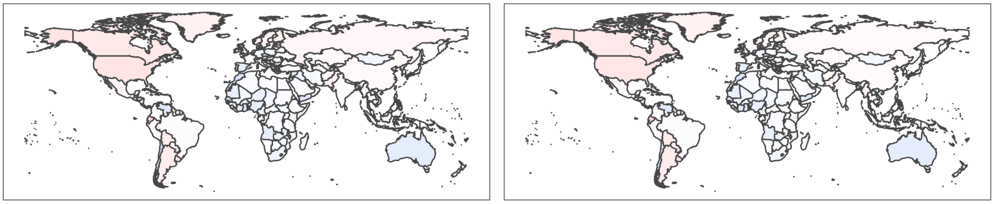

(e) FE-total effects **(f)** IE-total effects

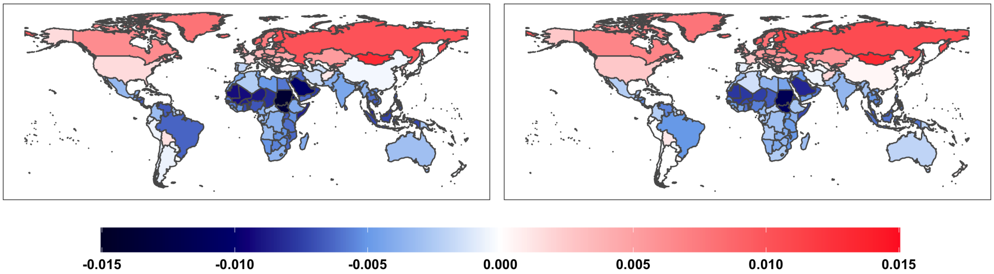

Fig. 5.3 Historical impacts of climate change over the period 1961-2019. The values indicate additional impacts on GDP growth. For instance, a value of 0.01 means that a country's GDP growth rate has increased by 1 percentage point over the period 1961-2019 due to historical climate change. In other words, a country with a growth rate of 3% year^{-1} at 2019 would have a growth rate of 2% year^{-1} if the effects of historical climate change were removed. The left panel shows the results of the additive fixed effects model (FE) and the right panel shows the results of the interactive fixed effects model (IE). The first row shows the impacts of historical temperature change; the second row reflects the impacts of precipitation change; the last row represents the sum of the effects of temperature and precipitation.

under the FE model (left panel) and IE model (right panel). The two models show highly consistent estimation of historical impacts of climate change. The estimation of the signs of impacts is identical for the FE and IE model, while the IE model has more optimistic estimation of positive climate impacts and less pessimistic estimation of negative values. The first row shows that mid- and high-latitude countries at Northern Hemisphere have benefited from historical warming. In general, the benefits are strengthened as latitude increases. The largest benefit is observed in Mongolia, which is the second coldest country next to Greenland. Since we assume global homogeneous sensitivity (β_1 and β_2 are the same for countries worldwide) in our theoretical framework, and given the fact that Greenland is colder than Mongolia, the economic effects of Greenland should be larger than that of Mongolia if two countries experience the same increment of temperature. However, a larger impact is found in Mongolia, which implies that the temperature of which has increased more than that of Greenland (1.36 vs. 0.88 $°C$ warming over 1961-2019 for Mongolia and Greenland, respectively).

Tropical and subtropical countries are harmed most by the rising of temperature, especially countries in northern Sub-Saharan Africa, and Saudi Arabia. A rise of temperature is especially damaging in theses countries because they are hot and have temperatures far greater than the optimal value of $14.74°C$. The most affected countries tend to associate with a relatively large increase of temperature. In particular, the temperatures in Sudan and South Sudan have increased by 1.67 and 1.69 $°C$ over 1961-2019, respectively. In conjunction with their high temperatures at the first place, it is not surprising to observe that their economies have been hit the most by historical warming.

Comparing to the impacts of temperature, precipitation has smaller effects and shows no association with latitude (Figure 5.3(c)(d)). The smaller magnitude could be due to the lack of persistent trends of precipitation. Positive impacts of precipitation are observed in Canada, the US, Argentina, Russia, etc. Negative impacts are found in African countries, Australia, etc. The third row (Figure 5.3(e)(f)) shows the total effects by adding the impacts of temperature and precipitation. Given the larger magnitude of temperature impacts, it is natural to find the total effects are dominated by the temperature effects.

In order to show the difference between the FE and IE model more clearly, Figure 5.4 plots the difference between the accumulated effects indicated by the FE and the IE model. Except for Greenland and Bolivia, the IE model tends to have more positive estimations for benefits caused by historical temperature change and more negative estimations for damages resulting from temperature rising.

Table 5.5 summarizes the historical effects of climate change on a regional basis. The upper panel shows the results for the additive fixed effects model (FE model). Eastern Europe and Central Asia (EECA) and Western Europe and Offshores (WEOFF) benefit both from the historical temperature and precipitation evolution, resulting in a population-weighted regional average increase of GDP growth by 0.73 and 0.29 percentage points, respectively. Latin America is harmed by warming but benefit from precipitation variation. Given the dominant role of temperature, the overall effect is a reduction of 0.47 percentage points on GDP growth. Southeast Asia has the similar situation, the temperature trends are detrimental while the precipitation evolution is beneficial for local economies. On the other hand, a double whammy of warming and precipitation variation is observed in Africa. In fact, Sub-Saharan Africa is negatively affected the most, with a substantial reduction of 0.73 percentage points on GDP growth. Globally speaking, the average global income growth was reduced by 0.30 percentage points under the FE model.

The results for the interactive fixed effects model (IE model, lower panel in Table 5.5, column 4) indicate less negative effects for regions harmed by total climate change, but more positive estimates for regions benefiting from historical climate evolution. Under the IE model, the estimation shows the GDP growth has increased by 0.77 percentage points for Eastern Europe and Central Asia, as compared to 0.73 percentage points under the FE model. The damage is estimated to be less severe. A reduction of 0.58 percentage points to GDP growth in Sub-Saharan is estimated from the IE model, as compared to the estimate of 0.73 percentage points under the FE model. The IE model also reports a smaller magnitude of global reduction of GDP growth, 0.108 vs. 0.30 percentage points (IE vs. FE).

5.4 Discussion

This paper examines the historical impacts of temperature and precipitation fluctuations on economic growth. Both temperature and precipitation show statistically significant non-linear effects to GDP growth. It means that before reaching an optimal value, an increase of temperature and precipitation is

(a) DIFF-temperature effects

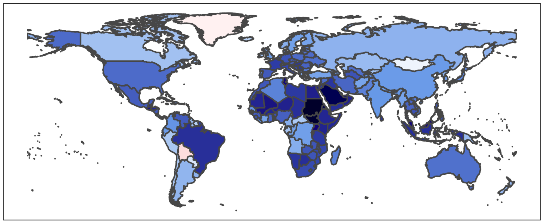

(b) DIFF-precipitation effects

(c) DIFF-total effects

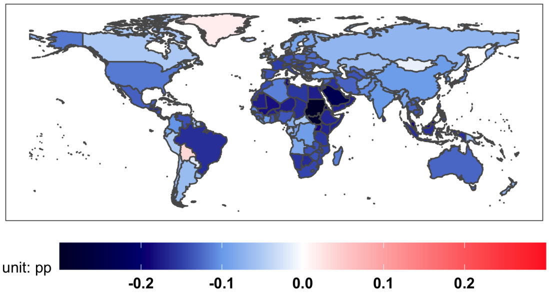

Fig. 5.4 Difference between the FE and IE estimation of historical impacts of climate change over the period 1961-2019. The values are in percentage point, showing the difference between the left panel and right panel in Figure 5.3.

beneficial to economic growth; beyond the optimal climate level, a continual increase will become damaging to economy. We employed two empirical models, the additive fixed effects model (FE model) and the interactive fixed effects model (IE model), to our global panel. The two models have highly similar shapes of response surfaces, with the FE model having slightly larger sensitivities to the quadratic terms of temperature and precipitation. In other words, the FE model has a more concave response surface, indicating more drastic responses to extreme climate conditions. For example, we show that under the FE model Sub-Saharan Africa has experienced an average 0.73 percentage points reduction on GDP growth over the period 1961-2019; while a reduction of 0.58 percentage

Table 5.5 Regional summary of historical climate change effects on GDP growth. The values show the population-weighted average effects on GDP growth, shown in percentage point, corresponding to the historical effects shown in Figure 5.3.

Region[a]	Temp Effects	Precip Effects	Total Effects
	Additive fixed effects		
EECA	0.714	0.012	0.727
LAC	−0.495	0.026	−0.470
MENA	−0.481	−0.029	−0.511
SEAS	−0.367	0.013	−0.354
SSAF	−0.702	−0.027	−0.729
WEOFF	0.235	0.054	0.289
Global Avg.	−0.305	0.010	−0.296
	Interactive fixed effects		
EECA	0.759	0.008	0.768
LAC	−0.396	0.021	−0.376
MENA	−0.308	−0.035	−0.344
SEAS	−0.259	0.015	−0.244
SSAF	−0.542	−0.041	−0.582
WEOFF	0.314	0.049	0.363
Global Avg.	−0.193	0.008	−0.185

[a] Refer to Figure S5.1 for the region definition in detail. EECA represents Eastern Europe and Central Asia, LAC for Eastern Europe and Central Asia, MENA for Middle East and Northern Africa, SEAS for Southeast Asia, SSAF for Sub-Suharan Africa, WEOFF for West Europe and Offshores.

points is found using the IE model. Moreover, the FE model also indicates a more negative impact on global economic growth. The global average historical impacts of climate change on GDP growth are reported as −0.30 percentage points and −0.19 percentage points for the FE and IE model, respectively.

Our results also show that countries have responded considerably differently to historical climate change. In particular, Europe and central Asia have benefited from both the historical temperature and precipitation effects, while a double whammy is observed in Africa, where countries' economic growth has been damaged by both factors.

Our findings in this paper provide insight into the role of temperature and precipitation in historical global economic growth. Understanding the impacts of climate change allows us to project future economic development under simulated climate pathways and thereby illuminating the prospect of economies we will face. Finally, the empirically estimated economic growth sensitivities to climate change in our paper can be further applied as inputs to “damage functions”, which are frequently applied by policy makers to translate climate change into social and economic losses.

Appendix

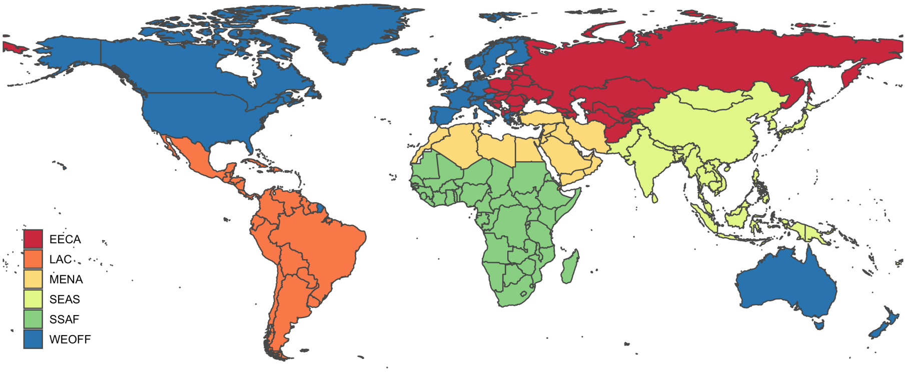

Fig. S5.1 Region definition.

References

Auffhammer, M. (2018). Quantifying economic damages from climate change. In *Journal of Economic Perspectives*, volume 32, pages 33–52. American Economic Association.

Bai, J. (2009). Panel data models with interactive fixed effects. *Econometrica*, 77(4):1229–1279.

Burke, M., Hsiang, S. M., and Miguel, E. (2015). Global non-linear effect of temperature on economic production. *Nature*, 527(7577):235–239.

Carleton, T. A. and Hsiang, S. M. (2016). Social and economic impacts of climate.

CIESIN (2000). Gridded Population of the World (GPW), v4.

Dell, M., Jones, B. F., and Olken, B. A. (2012). Temperature shocks and economic growth: Evidence from the last half century. *American Economic Journal: Macroeconomics*, 4(3):66–95.

Dell, M., Jones, B. F., and Olken, B. A. (2014). What do we learn from the weather? The new climate-economy literature.

Diffenbaugh, N. S. and Burke, M. (2019). Global warming has increased global economic inequality. *Proceedings of the National Academy of Sciences of the United States of America*, 116(20):9808–9813.

Harris, I., Osborn, T. J., Jones, P., and Lister, D. (2020). Version 4 of the CRU TS monthly high-resolution gridded multivariate climate dataset. *Scientific Data*, 7(1).

IPCC AR5 (2014). AR5 Climate Change 2014: Impacts, Adaptation, and Vulnerability. *Fifth Assessment Report of the Intergovernmental Panel on Climate Change.*

Lobell, D. B. and Burke, M. B. (2010). On the use of statistical models to predict crop yield responses to climate change. *Agricultural and Forest Meteorology*, 150(11):1443–1452.

Rodrik, D., Subramanian, A., and Trebbi, F. (2004). Institutions rule: The primacy of institutions over geography and integration in economic development. *Journal of Economic Growth*, 9(2):131–165.

WDI (2020). Word Development Indicators.

Appendices

APPENDIX A

Supporting Information for Paper 1

A.1 Dataset Description

Figure A.1 shows a map of the distribution of GEBA stations.

A.2 RF model Parameter Tuning

The tuning of the number of bootstraps is shown in Figure A.2. We choose the parameter value, 700, that the R^2 reach a high level and are relatively stable. Likewise, the number of candidate independent variables is set to 8 (Figure A.3).

A.3 Results

A.3.1 Model Evaluation

Figure A.4 shows a scatter plot of predicted values against observed values for each continent respectively. We see that the regression coefficients of the regression lines are reasonably close to 1 and the intercept terms are relatively small compared to the magnitude of average SSR levels. Although the models perform differently among the continents (e.g., better performance in North America and Europe, less ideal performance in South America and Africa), in general, the models are able to capture the variation of SSR. Caution needs to be taken when interpreting the high levels of R^2. Because the R^2 are calculated based on raw values of SSR, they might have a systematic bias toward large values caused by the strong seasonality of monthly SSR.

A.3.2 Continental Average Trend Analysis

When calculating the global/continental average SSR of month t ($\bar{R}_t$), each grid ($R_{i,t}$) is weighted by the *cosine* of the latitude, which is given by:

$$\bar{R}_t = \sum_{i=1}^{N} w_i R_{i,t} \tag{A.1}$$

where

$$w_i = \frac{\cos(latitude_i)}{\sum_i \cos(latitude_i)},\ latitude_i \in [-\frac{\pi}{2}, \frac{\pi}{2}] \tag{A.2}$$

The weighting procedure is to account for that the areas of grid boxes reduce with increasing latitude. By using the weight of *cosine* of latitude, it means to apply a weight of one for grid cells at the equator (which have $0\,rad$ latitude, and therefore assigned a weight of $cos(0) = 1$), and to apply a weight of zero for grid cells at the poles (which have $\frac{\pi}{2}\,rad$ latitude, and a weight of $cos(\frac{\pi}{2}) = 0$).

For the entire globe as well as each continent, monthly anomalies of global/continental average SSR are calculated and visualized in figures. Also shown are the regression lines for the entire period 1961-2019 and for the sub-segments separated by the detected breakpoints (refer to main paper Table 4 for the breakpoints as well as the slope coefficients).

Figure A.5—Figure A.11 show the monthly anomaly figures in what follows.

World

Monthly anomalies Figure A.5

Europe

Monthly anomalies Figure A.6

Africa

Monthly anomalies Figure A.7

Asia

Monthly anomalies Figure A.8

Oceania

Monthly anomalies Figure A.9

North America

Monthly anomalies Figure A.10

South America

Monthly anomalies Figure A.11

List of Figures

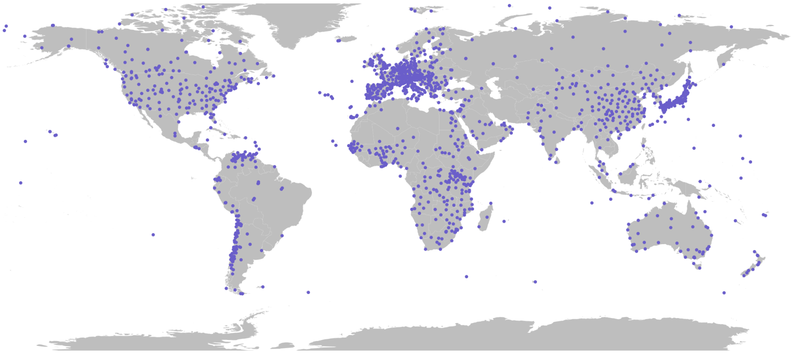

Fig. A.1 Station distribution in the GEBA dataset

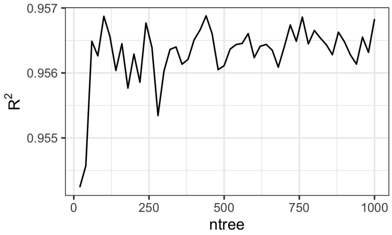

Fig. A.2 R^2 changing with the number of decision trees

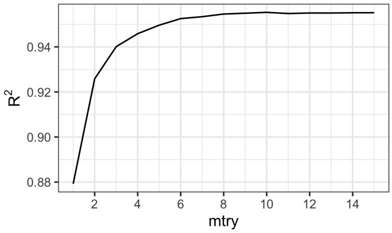

Fig. A.3 R^2 changing with the number of randomly preselected predictor variables

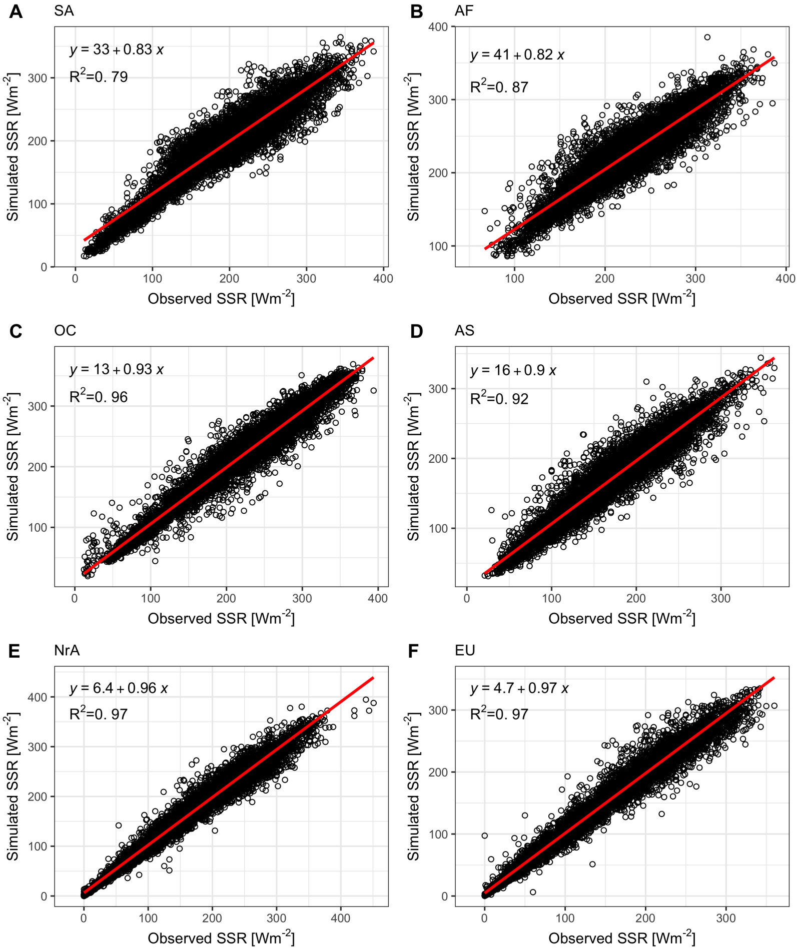

Fig. A.4 Simulation against observation raw values of SSR. The red line is obtained by regressing simulated SSR on observed SSR, also shown in each panel are the corresponding equation and R squared.

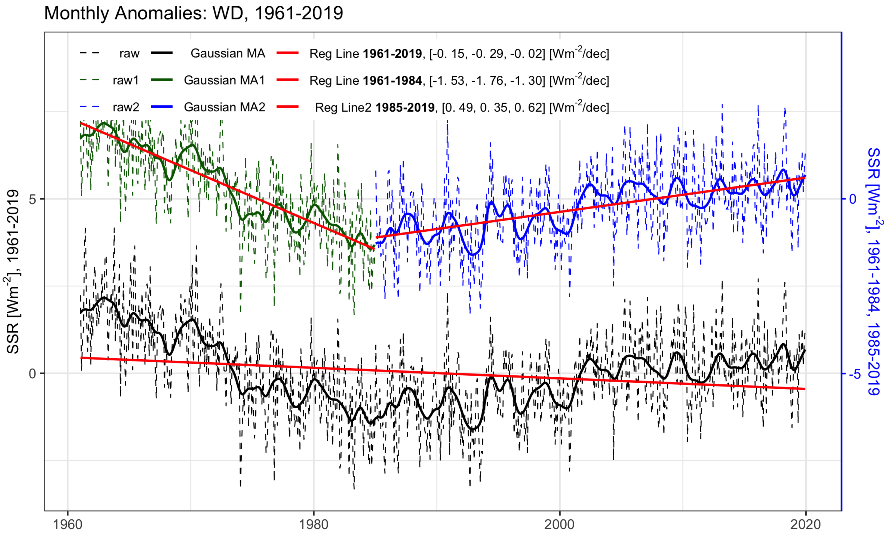

Fig. A.5 SSR global monthly anomalies over the time period 1961-2019 (left axis, lower black lines), and over segments divided by its breakpoint at 1984 (right axis, upper lines), namely, the first segment over 1961-1984 (dark green lines), and the second segment over 1985-2019 (blue lines). Raw monthly anomaly series are shown by the dashed lines, expressed as anomalies from the mean over the entire period. Additionally shown are the smoothed series by 12-month Gaussian filter (solid lines) and the linear decadal regression lines (red solid lines). The values in the brackets show the mean trend, lower 95% percentile, and upper 95% percentile, respectively. Note that the right axis is shifted by +5 Wm^{-2} from the left axis in order to separate the two series.

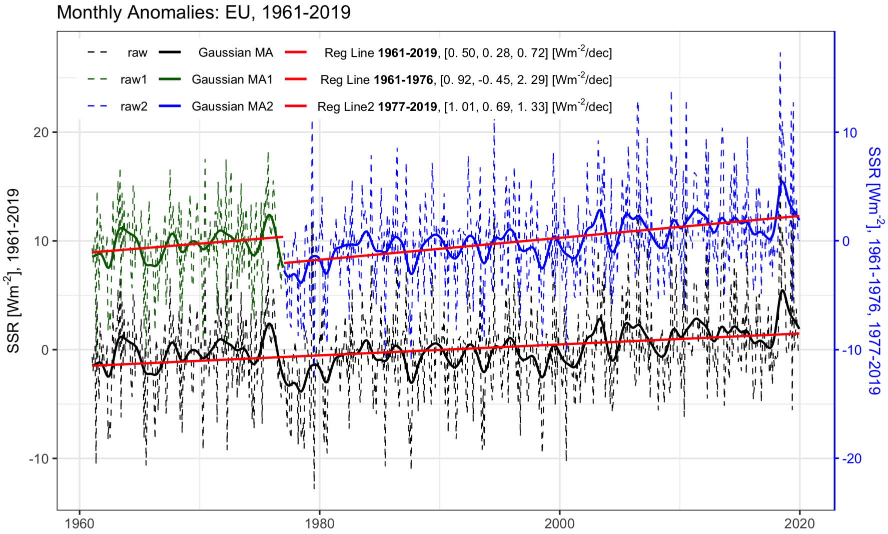

Fig. A.6 SSR monthly anomalies for Europe. Legends are the same as those of Figure A.5, though two time segments here are 1961-1976 and 1977-2019.

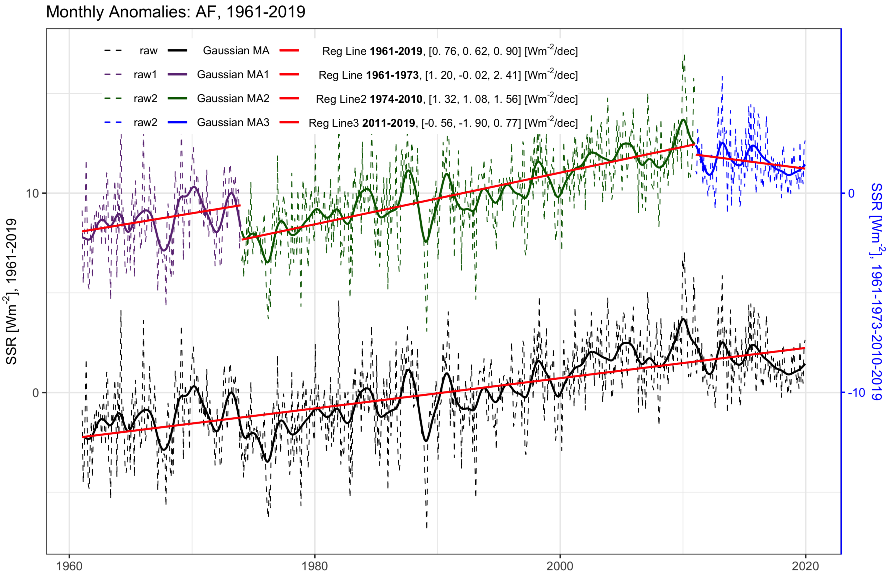

Fig. A.7 SSR monthly anomalies for Africa.

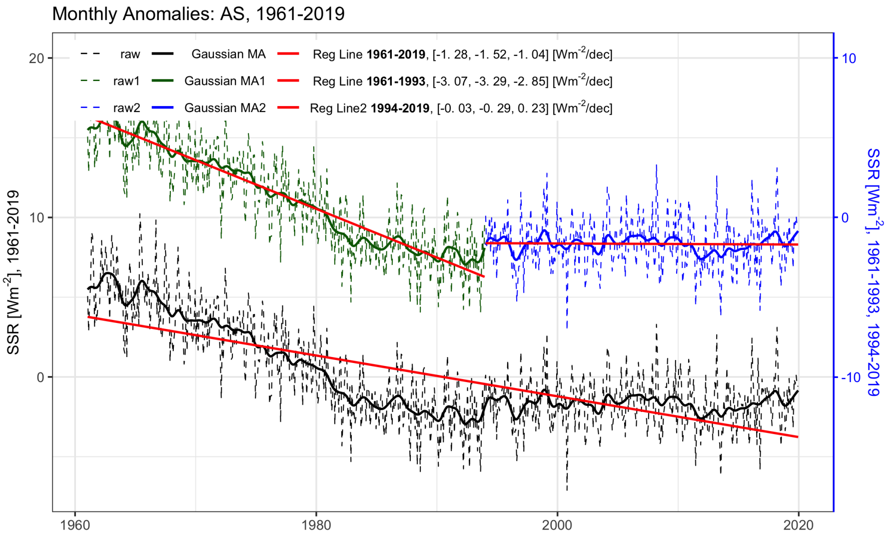

Fig. A.8 SSR monthly anomalies for Asia.

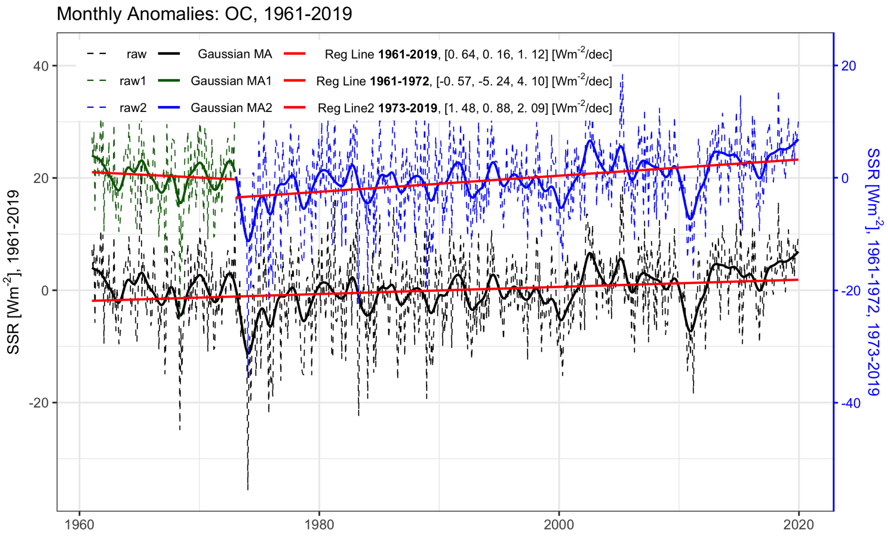

Fig. A.9 SSR monthly anomalies for Oceania.

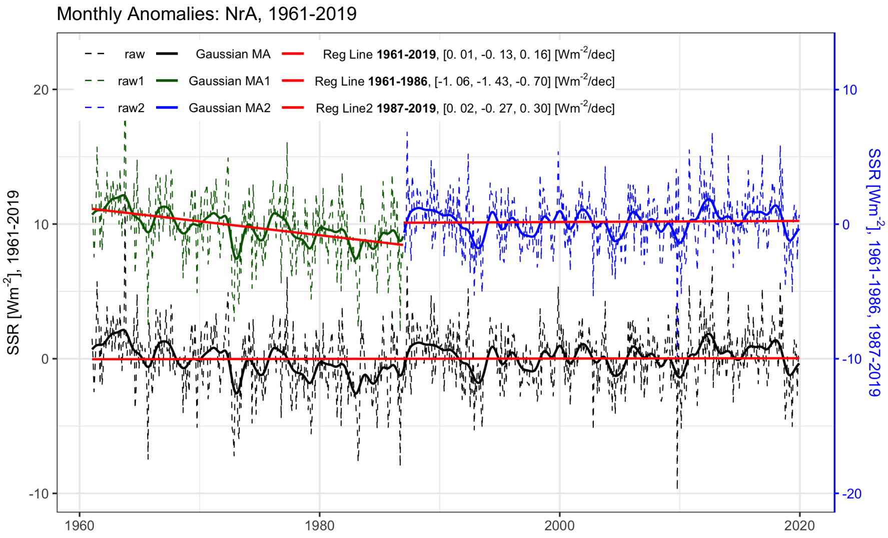

Fig. A.10 SSR monthly anomalies for North America.

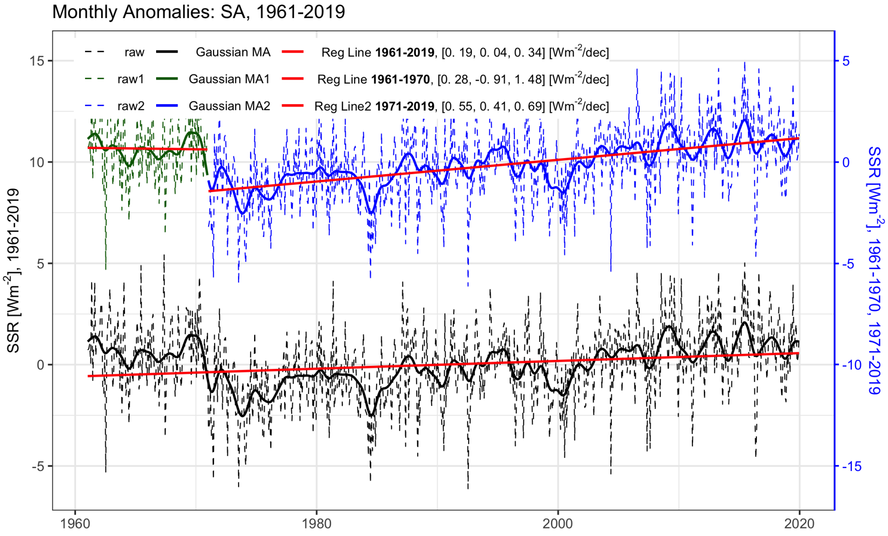

Fig. A.11 SSR monthly anomalies for South America.

APPENDIX B

Supporting Information for Paper 2

B.1 Econometric Framework

B.1.1 Model Description

We use a panel econometric framework for TCR estimation that relates local (station cell i) temperature at time $t+1$ ($T_{i,t+1}$) to local temperature ($T_{i,t}$), surface solar radiation ($R_{i,t}$), and global factors (λ_t), all at time t in the following system

$$\begin{aligned} T_{i,t+1} &= \alpha_i + \beta_1 T_{i,t} + \beta_2 R_{i,t} + \phi_i \lambda_t + u_{i,t+1}, && \text{(B.1a)} \\ \lambda_t &= \gamma_0 + \gamma_1 \bar{T}_t + \gamma_2 \bar{R}_t + \gamma_3 \ln(CO_{2,t}), && \text{(B.1b)} \\ i &= 1, \cdots, N \text{ and } t = 1, \cdots, n \end{aligned}$$

where the α_i are individual effects representing the idiosyncratic characteristics at a particular location i. The component λ_t in (B.1b) is a time specific effect representing global energy influences determined by past global mean temperature ($\bar{T}_t$) and radiation ($\bar{R}_t$), measured by the weighted averages

$$\bar{T}_t = \sum_{i=1}^{N} w_i T_{i,t}, \quad \bar{R}_t = \sum_{i=1}^{N} w_i R_{i,t}, \tag{B.2}$$

and the logarithm of CO_2 equivalent emissions ($ln(CO_{2,t})$). In the case where point data are used the global averages are simple averages over the sampled locations (i.e., $w_i = N^{-1}$). Otherwise when grid data are employed, global averages are computed by weighting to scale for latitude using the following weights

$$w_i = \frac{\cos(latitude_i)}{\sum_{i=1}^{N}\cos(latitude_i)}, \quad latitude_i \in [-\frac{\pi}{2}, \frac{\pi}{2}]. \tag{B.3}$$

The weighting procedure (B.3) accounts for the areas of gridboxes reduce with increasing latitude. The use of cosine of latitude weights implies a unit weight for grid cells at the equator (with $0\,rad$ latitude and weight $cos(0) = 1$) and a zero weight for grid cells at the poles (with $\pm\frac{\pi}{2}\,rad$ latitude and weight $cos(\pm\frac{\pi}{2}) = 0$).

The model (B.1a) and (B.1b) can be used to estimate a parametric representation of Earth's Transient Climate Response (TCR), which measures the global mean surface air temperature change resulting from a doubling of atmospheric CO_2 at that time that doubling occurs. In particular, aggregating (B.1a) and substituting (B.1b) gives the global relationship

$$\bar{T}_{t+1} = \gamma_0 + \theta_1\bar{T}_t + \theta_2\bar{R}_t + \gamma_3\ln(CO_{2,t}) + \bar{u}_{\cdot t+1} \tag{B.4}$$

where $\theta_1 = \beta_1 + \gamma_1$, $\theta_2 = \beta_2 + \gamma_2$, and $\bar{u}_{\cdot t+1} = N^{-1}\sum_{i=1}^{N} u_{i,t+1}$. Solving (B.4) and taking account of the trend in $\ln(CO_{2,t})$ leads to a long-run (called 'cointegrating') equilibrium relationship among the variables $\big(\bar{T}_t, \bar{R}_t, \ln(CO_{2,t})\big)$ of the form (see Phillips et al. (2020) for details and discussion)

$$\bar{T}_t = \frac{\theta_2}{1-\theta_1}\bar{R}_t + \frac{\gamma_3}{1-\theta_1}\ln(CO_{2,t}) + \frac{\mu}{1-\theta_1} + \frac{1}{1-\theta_1}\xi_t, \tag{B.5}$$

for some constant μ and stationary process ξ_t. The equation (B.5) reveals the long-run impact of $\ln(CO_2)$ on global temperature. The required parametric measure of the TCR is then obtained by scaling the coefficient of $\ln(CO_2)$ by $\ln(2)$ to account for a doubling of atmospheric CO_2, viz.,

$$TCR = \frac{\gamma_3}{1-\theta_1} \times \ln(2) = \frac{\gamma_3}{1-\beta_1-\gamma_1} \times \ln(2) \tag{B.6}$$

This formulation makes it possible to estimate TCR using (B.5) with observed global data for $\big(\bar{T}_t, \bar{R}_t, \ln(CO_{2,t})\big)$.

B.1.2 Estimation Method

Since the global variables $\left(\bar{T}_t, \bar{R}_t, \ln(CO_{2,t})\right)$ have nonstationary features involving both deterministic and stochastic trends (Phillips et al., 2020), equation (B.5) provides a balancing structural relationship among them that can be estimated conveniently by regression methods modified to take into account their trending nature. Asymptotically efficient estimates of the coefficients in equation (B.5) under general assumptions on the errors ξ_t can be obtained by fully modified least squares (FM-OLS, Phillips and Hansen, 1990). This approach has the advantage of allowing for both cross section and time series dependency in the original panel observations $(T_{i,t}, R_{i,t})$ as well as trending characteristics in the two regressors $\ln(CO_{2,t})$ and $\bar{R}_t$.

Rewrite (B.5) as

$$\bar{T}_t = d_0 + d_1\bar{R}_t + d_2\ln(CO_{2,t}) + \xi_{d,t} =: d_0 + d'x_t + \xi_{d,t}, \tag{B.7}$$

where $d_0 = \frac{u}{1-\theta_1}$, $d_1 = \frac{\theta_2}{1-\theta_1}$, $d_2 = \frac{\gamma_3}{1-\theta_1}$, and $\xi_{d,t} = \frac{1}{1-\theta_1}\xi_t$. Here, the coefficient vector d is the primary model parameter of interest and $x_t = \left(\bar{R}_t, ln(CO_2)\right)'$ is the vector of regressors. The FM-OLS estimator of the parameter vector d has the explicit form

$$\hat{d}^+ = \left(\tilde{X}'\tilde{X}\right)^{-1}\left(\tilde{X}'\widehat{\tilde{T}^+} - n\hat{\Delta}^+_{x\xi}\right). \tag{B.8}$$

The estimation method is analogous to least squares regression but incorporates modifications that take account of endogeneity (or joint determination) of the variables $\left(\bar{T}_t, \bar{R}_t, \ln(CO_{2,t})\right)$ and the presence of trends and serial dependence in their generating mechanism. In (B.8) the tilde affixes denote demeaned variables, $\widehat{\tilde{T}^+}$ is the observation vector of endogeneity-corrected and demeaned dependent variables $\bar{T}_t$, $\hat{\Delta}^+_{x\xi}$ is a second-order bias correction term employed to validate conventional methods of inference, and $\tilde{X}$ is the observation matrix of the regressor variables $\left(\bar{R}_t, \ln(CO_{2,t})\right)$. Details of the construction of the FM-OLS estimator and its asymptotic properties are given in Phillips and Hansen (1990); Phillips (1995).

B.1.3 Conversion from Global TCR to Land TCR

Empirical estimation of TCR in the paper is based on land area and denoted TCR_L. To obtain a global estimate, denoted TCR_G, we use the following transformation

$$TCR_G = TCR_L \cdot \frac{A_L \cdot w_L + A_O \cdot w_O}{w_L} = TCR_L \cdot \left(A_L + A_O \cdot \frac{w_O}{w_L}\right) = TCR_L \cdot W_{trans}, \tag{B.9}$$

where A_L and A_O are Earth's land area and ocean area fractions which are set to 0.29 and 0.71, respectively. The fraction $\frac{w_O}{w_L}$ stands for the *ocean-land warming ratio*, where w_O denotes the warming rate over ocean and w_L over land. We can rewrite the conversion rate as one factor $W_{trans} = A_L + A_O \cdot \frac{w_O}{w_L}$.

However, instead of using the ocean-land warming ratio, a more commonly reported term in climate science is its inverse, the *land-ocean warming ratio*, which measures how much faster the warming is over land than over ocean (Wallace and Joshi, 2018). We therefore rewrite the conversion factor as

$$W_{tran} = A_L + A_O \cdot \frac{w_O}{w_L} = A_L + \frac{A_O}{WR} \tag{B.10}$$

where $WR = \frac{w_L}{w_O}$ is the *land-ocean warming ratio.*

Since data are readily available for land areas and for the globe, we calculate the land and global warming rate (w_l and w_G), and then back out the ocean warming rate using $w_O = (w_G - w_l \cdot A_L)/A_O$. The warming rate, w_l or w_G, is calculated as the least squares estimate of the slope coefficient from regressing land/global temperature on a linear time trend using the following equation

$$Temp = \beta_0 + \beta_1 t + \epsilon \tag{B.11}$$

where $Temp$ is a $T \times 1$ vector of annual average surface air temperature over land or the globe, T is the number of years for which the temperature data are available, t is a $T \times 1$ vector of years, and (β_0, β_1) are scalar coefficients. The slope coefficient β_1 is estimated by

$$\hat{\beta}_1 = (t't)^{-1}t'Temp \tag{B.12}$$

To account for the uncertainty from various ensemble members of each ESM, we add an amplifying factor of ±0.5 to $1/WR$. When calculating a confidence interval (CI) for TCR_G, we use (B.13) to obtain the lower and upper bound of the CI as follows

$$\begin{aligned} W^{-}_{trans} &= A_L + \frac{A_O}{WR} \cdot (1 - 0.05) \\ W^{+}_{trans} &= A_L + \frac{A_O}{WR} \cdot (1 + 0.05) \end{aligned} \tag{B.13}$$

This adjustment leads to a slightly wider uncertainty range than the 95% CI of TCR_G based on the transformation factor W_{trans} alone.

B.2 Data Availability

TCR estimation is implemented on both the observed and simulated climate datasets.

B.2.1 Climate Observations

Climate Research Unit Time Series (CRU TS4.00 http://data.ceda.ac.uk/)(Harris et al., 2020) provides monthly temperature data over all land areas, spanning 1901-2015, on a 0.5 by 0.5 degree grid. The dataset is produced and maintained by University of East Anglia. Surface solar radiation data used in this study are obtained and extrapolated from the Global Energy Balance Archive (GEBA http://www.geba.ethz.ch/)(Wild et al., 2017), which is maintained by the Institute for Climate and Atmospheric Science at ETH Zurich. The GEBA dataset collects observations from ∼2500 climate stations worldwide and it provides the longest record for monthly SSR starting from the early 1950s and up to 2015. In spite of its unparalleled spatial and temporal coverage, station data tend to cluster in developed regions which can provide the financial and technical support to maintain the devices, making it problematic to use the station data in regions where only few station facilities exist to represent adequately overall regional trends. We therefore use an interpolated GEBA dataset in our paper, which was constructed by Yuan et al. (2021).

To explain the SSR dataset used in the current paper we outline the specific Random Forest (RF) methodology used in its construction. RF is a regression tree algorithm for regression and classification. It constructs a forest of decision trees that operates as a predicting ensemble whose prediction accuracy is higher than that of any individual tree (Breiman, 2001). The effectiveness of using RF in predicting the SSR has been demonstrated in many studies (Sun et al., 2016; Zhou et al., 2017; Leirvik and Yuan, 2021). In the application of Yuan et al. 15 predictors are chosen for predicting the SSR, including 9 meteorological variables (cloud cover, maximum temperature, minimum temperature, diurnal temperature, precipitation, vapour pressure, number of ground frost days, number of rainy days), temporal stamp indicators (year and month of the observation) and geographical characteristics (longitude, latitude, elevation, and rural/urban designation). Performance evaluation by a 10-fold cross validation shows the RF model reproduces observations with a R^2 of 0.92 and a mean absolute error of 12.50 Wm^{-2}. The trained RF model was then applied to interpolate and generate a monthly gridded dataset over global land areas at 0.5° resolution and covering the period 1961-2019.

B.2.2 Climate Simulations

We used data from 22 Earth System Models (ESMs) from the Coupled Model Intercomparison Project - Phase 6 archive (CMIP6, Eyring et al., 2016) for temperature and radiation simulations, giving 'synthetic observations' for analysis by econometric methods to compare the findings with those from direct observational data. Data from historical experiments up to the final simulated year 2014 were employed in the exercise. The first realization is used when an ensemble of simulations is provided, with the variant label "r1i1p1f1". While the observational data cover all land areas, the ESMs have global spatial coverage, including both land and ocean areas. Accordingly, to match spatial coverage between the observational and synthetic data, the simulations over ocean areas in each ESM are masked, retaining only the data over land areas.

Due to the data availability of CMIP6 ESM simulations, we focus the TCR estimation on the specific time period 1964-2014 of this study.

B.2.3 CO_2 equivalent emissions

The National Oceanic and Atmospheric Administration (NOAA) Annual Greenhouse Gas Index (AGGI https://www.esrl.noaa.gov/gmd/aggi/) is a measurement of interannual time series variability of global forcing (also termed 'radiative forcing') resulting from changes in global atmospheric long-lived mixed greenhouse gases (Hofmann et al., 2006). Changes in component GHGs are converted to global forcing to provide an aggregate quantity of perturbation in Earth's radiative energy budget. CO_2 is by far the largest contributor to the abundance and changes of the index. Other major non-CO_2 GHGs, including carbon dioxide, methane, nitrous oxide, and halogenated compounds, are converted to global forcing measurements and aggregated with that of CO_2 to obtain an index of the total radiative forcing of the GHGs. This aggregation ensures that the index can be deemed an instrument of equivalent CO_2 concentration in the atmosphere.

B.2.4 Reported TCR

TCR was calculated as the change in global near surface temperature in a 20-year average around the time of CO_2 doubling (years 60-79 in simulations in which CO_2 was increased by 1% per year) as compared to the equivalent 20-year segment of each model's own pre-industrial control simulation. The equivalent time period was used to avoid influence from any drift due to remaining energy imbalance in the control. Confidence levels were found by bootstrapping the mean difference between the two 20-year segments with 10,000 realizations.

B.3 Empirical Results

B.3.1 Land-Ocean Warming Ratio

Table B.1 summarises the warming rates over the globe (w_G), land (w_L), and ocean areas (w_O), as well as the land-ocean warming ratios (WR) for the 22 ESMs. The warming ratios span from 1.29 (BCC-ESM1) to 2.02 (MIROC6), with an average of 1.63 and standard deviation of 0.20. For the observational data we use the conventional value 1.62 for WR and W_{trans} being 0.728, as below

$$W_{trans} = A_L + A_O/WR = 0.29 + 0.71/1.62 = 0.728. \tag{B.14}$$

Table B.1 ESM warming ratio and conversion factor. Warming over the globe ($\boldsymbol{w_G}$) is calculated using the complete ESM data; warming over land ($\boldsymbol{w_L}$) is obtained by masking the global ESM to retain only the land areas; and warming over ocean ($\boldsymbol{w_O}$) can be obtained using the formula in footnote [a]. $\boldsymbol{WR}$ is the land-ocean warming ratio; $\boldsymbol{W_{tran}}$ is the conversion factor transforming the land TCR to the global TCR.

Model	$\boldsymbol{w_G}$ $[°C/dec]$	$\boldsymbol{w_L}$ $[°C/dec]$	$\boldsymbol{w_O}$[a] $[°C/dec]$	$\boldsymbol{WR}$[b]	$\boldsymbol{W_{tran}}$[c]
BCC-CSM2-MR	0.14	0.21	0.12	1.83	0.68
BCC-ESM1	0.16	0.20	0.15	1.29	0.84
CAMS-CSM1-0	0.11	0.13	0.10	1.31	0.83
CanESM5	0.25	0.34	0.22	1.53	0.76
CESM2	0.21	0.29	0.17	1.69	0.71
CESM2-WACCM	0.20	0.28	0.17	1.65	0.72
CNRM-CM6-1	0.19	0.26	0.16	1.68	0.71
CNRM-ESM2-1	0.17	0.24	0.14	1.71	0.70
E3SM-1-0	0.20	0.29	0.16	1.85	0.67
EC-Earth3-Veg	0.23	0.32	0.19	1.68	0.71
GISS-E2-1-G	0.17	0.21	0.15	1.41	0.79
GISS-E2-1-H	0.22	0.27	0.20	1.36	0.81
HadGEM3-GC31-LL	0.23	0.30	0.20	1.46	0.78
IPSL-CM6A-LR	0.17	0.25	0.13	1.87	0.67
MIROC-ES2L	0.13	0.19	0.11	1.80	0.68
MIROC6	0.13	0.21	0.10	2.02	0.64
MPI-ESM-1-2-HR	0.14	0.17	0.13	1.35	0.82
MRI-ESM2	0.16	0.23	0.13	1.77	0.69
NESM3	0.17	0.24	0.14	1.67	0.71
NorESM2-LM	0.18	0.26	0.15	1.78	0.69
SAM0-UNICON	0.16	0.23	0.14	1.68	0.71
UKESM1-0-LL	0.26	0.33	0.23	1.47	0.77
ESM Mean	**0.18**	**0.25**	**0.15**	**1.63**	**0.73**
ESM St. Dev.	**0.04**	**0.05**	**0.04**	**0.20**	**0.06**

[a] $w_O = (w_G - w_l \cdot A_L)/A_O$

[b] (4)=(2)/(3)

[c] (5)=$A_L + A_O/(4)$.

B.3.2 TCR estimates

Table B.2 shows the parameter values that result from applying equation (B.7) to observations and ESM simulations. Land TCR is just the coefficient of $\ln(CO_2)$ scaled by $\ln(2)$, which is then converted to global TCR using equation (B.9). The global TCR estimates are reported in Table B.3. A scatter plot of warming ratios against estimated TCR_G for 22 ESMs (black solid points) and observations (red solid points) shows that ESMs tends to have higher WRs and smaller TCR than observations (Figure B.1). The largest concentration (10 models) falls within the second quadrant if we set observational WR and TCR as origin. There are four models falling within each of the remaining three quadrants.

Under this framework the observed continental temperature evolution can be reproduced reasonably well, resulting in a land average surface air temperature increase of approximately $1.1°C$ over the period from 1964 to 2014 (Figure B.2, green line). In order to separate out the individual contribution from radiation and CO_2, two scenarios are simulated based on the constant levels for each of the variables respectively. In the hypothetical case that CO_2 remained constant at its 1964 value, the temperature trend is dominated by the cooling effects resulting from the total aerosol effects, which are reflected in changes in surface solar radiation. The total average effect of aerosols is a temperature reduction of approximately $0.3°C$, with the strongest cooling effect found prior to 1990 (Figure B.2, red line), a finding that is consistent with that reported in previous studies (Wild et al., 2007; Storelvmo et al., 2016). Conversely, if surface solar radiation is kept constant at its 1964 level, corresponding to constant atmospheric aerosol concentrations, a substantial increase due to greenhouse gase warming of $1.5°C$ is predicted (Figure B.2, blue line). As compared to the usual scenario's warming of $1.1°C$, nearly one-fourth of the potential continental warming induced by increased greenhouse gas concentrations has been masked by the cooling effects of aerosol emissions during the time period. These findings substantially corroborate the masking effect reported in previous work (Storelvmo et al., 2016).

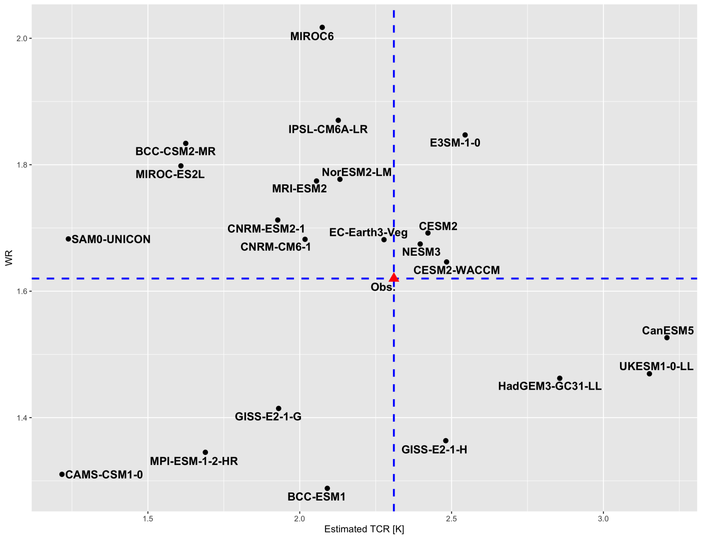

Fig. B.1 Warming ratios plotted against estimated TCR_G for 22 ESMs and observations. ESMs are denoted by the black dots, observations by the red triangle. The dashed lines represent x/y-axis if setting observations as origin.

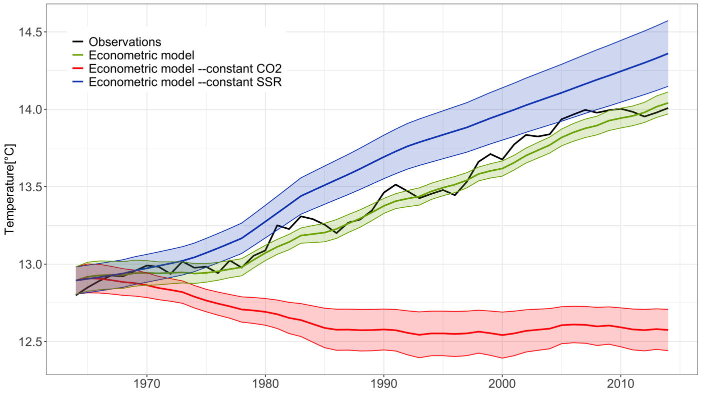

Fig. B.2 Global land average temperature as observed (black line) and as predicted with equation (B.7) (green line). Also shown is predicted temperature under the scenario of constant CO_2 levels at 1964 (red line), such that any changes in temperature are attributable to surface solar radiation variability. Likewise the constant surface solar radiation scenario is shown by the blue lines, such that trends in temperature are controlled by changes in CO_2. All series are shown as 5-year running means. Shadings represent the 95% confidence intervals from the regression.

Table B.2 Parameter values, standard errors and confidence intervals for the parameter of equation (B.7)

Model	Parameter	Value	St. Dev.	95% Confidence Interval
Observation	d1	0.0566	0.0154	(0.0264, 0.0868)
	d2	4.5799	0.2924	(4.0067, 5.1530)
BCC-CSM2-MR	d1	0.1975	0.0434	(0.1123, 0.2826)
	d2	3.4611	0.3820	(2.7124, 4.2098)
BCC-ESM1	d1	0.1189	0.0786	(-0.0351, 0.2729)
	d2	3.5860	0.4598	(2.6848, 4.4872)
CAMS-CSM1-0	d1	0.0315	0.0374	(-0.0419, 0.1049)
	d2	2.1108	0.3280	(1.4678, 2.7537)
CanESM5	d1	0.1331	0.0537	(0.0279, 0.2383)
	d2	6.1314	0.5992	(4.957, 7.3057)
CESM2	d1	0.1207	0.0515	(0.0198, 0.2215)
	d2	4.9244	0.4266	(4.0882, 5.7606)
CESM2-WACCM	d1	0.0922	0.0739	(-0.0526, 0.2370)
	d2	4.9677	0.6489	(3.6958, 6.2395)
CNRM-CM6-1	d1	0.0536	0.0412	(-0.0271, 0.1344)
	d2	4.0873	0.3395	(3.4220, 4.7527)
CNRM-ESM2-1	d1	0.0448	0.0808	(-0.1136, 0.2032)
	d2	3.9468	0.6374	(2.6975, 5.1961)
E3SM-1-0	d1	0.1853	0.1166	(-0.0432, 0.4139)
	d2	5.4436	0.8979	(3.6837, 7.2035)
EC-Earth3-Veg	d1	-0.0023	0.0501	(-0.1005, 0.0959)
	d2	4.6132	0.4745	(3.6833, 5.5432)
GISS-E2-1-G	d1	0.0282	0.0490	(-0.0678, 0.1243)
	d2	3.5169	0.6035	(2.3341, 4.6997)
GISS-E2-1-H	d1	0.0381	0.0298	(-0.0203, 0.0966)
	d2	4.4150	0.3816	(3.6671, 5.1628)
HadGEM3-GC31-LL	d1	0.2855	0.1119	(0.0661, 0.5049)
	d2	5.3133	0.7707	(3.8028, 6.8238)
IPSL-CM6A-LR	d1	0.1574	0.0711	(0.0181, 0.2967)
	d2	4.5824	0.5709	(3.4635, 5.7013)
MIROC-ES2L	d1	0.0812	0.0552	(-0.0270, 0.1893)
	d2	3.3888	0.3939	(2.6168, 4.1609)
MIROC6	d1	0.2127	0.0734	(0.0689, 0.3566)
	d2	4.6611	0.5701	(3.5437, 5.7786)
MPI-ESM-1-2-HR	d1	0.1531	0.0546	(0.0461, 0.2600)
	d2	2.9799	0.3974	(2.2010, 3.7589)
MRI-ESM2	d1	0.1611	0.0494	(0.0642, 0.2580)
	d2	4.2962	0.3633	(3.5841, 5.0083)
NESM3	d1	0.3038	0.0426	(0.2202, 0.3874)
	d2	4.8428	0.3772	(4.1035, 5.5821)
NorESM2-LM	d1	0.1668	0.0775	(0.0149, 0.3186)
	d2	4.4613	0.4879	(3.5050, 5.4176)
SAM0-UNICON	d1	-0.0798	0.1299	(-0.3345, 0.1748)
	d2	2.5089	0.8307	(0.8808, 4.1371)
UKESM1-0-LL	d1	0.2184	0.0606	(0.0995, 0.3372)
	d2	5.8804	0.4050	(5.0866, 6.6743)

The coefficient d_1 relates to global average radiation ($\bar{R}_t$), d_2 relates to $\ln(CO_2)$.

Table B.3 Reported and estimated global TCR

Model	Estimated TCR_G	Estimated 95% CI	Reported TCR_G	Reported 95% CI
Observation	2.31	(1.96, 2.68)	-	-
BCC-CSM2-MR	1.62	(1.24, 2.03)	1.36	(1.23, 1.45)
BCC-ESM1	2.09	(1.51, 2.70)	1.77	(1.65, 1.85)
CAMS-CSM1-0	1.22	(0.82, 1.64)	1.73	(1.63, 1.82)
CanESM5	3.21	(2.51, 3.94)	2.73	(2.54, 2.83)
CESM2	2.42	(1.95, 2.92)	2.00	(1.89, 2.07)
CESM2-WACCM	2.48	(1.79, 3.21)	1.93	(1.79, 2.03)
CNRM-CM6-1	2.02	(1.64, 2.42)	2.23	(2.08, 2.35)
CNRM-ESM2-1	1.93	(1.28, 2.61)	1.83	(1.71, 1.91)
E3SM-1-0	2.54	(1.67, 3.46)	2.90	(2.76, 2.99)
EC-Earth3-Veg	2.28	(1.76, 2.82)	2.65	(2.48, 2.75)
GISS-E2-1-G	1.93	(1.24, 2.66)	1.73	(1.60, 1.85)
GISS-E2-1-H	2.48	(1.99, 2.99)	1.86	(1.71, 1.95)
HadGEM3-GC31-LL	2.86	(1.98, 3.78)	2.48	(2.33, 2.60)
IPSL-CM6A-LR	2.13	(1.56, 2.72)	2.41	(2.28, 2.50)
MIROC-ES2L	1.61	(1.21, 2.03)	1.48	(1.34, 1.57)
MIROC6	2.07	(1.53, 2.64)	1.56	(1.46, 1.65)
MPI-ESM-1-2-HR	1.69	(1.21, 2.20)	1.63	(1.53, 1.70)
MRI-ESM2	2.06	(1.66, 2.47)	1.67	(1.56, 1.73)
NESM3	2.40	(1.97, 2.84)	2.72	(2.55, 2.84)
NorESM2-LM	2.13	(1.63, 2.66)	1.50	(1.39, 1.59)
SAM0-UNICON	1.24	(0.42, 2.10)	2.21	(2.09, 2.30)
UKESM1-0-LL	3.15	(2.64, 3.69)	2.79	(2.60, 2.91)

References

Breiman, L. (2001). Random forests. *Machine learning*, 45(1):5–32.

Eyring, V., Bony, S., Meehl, G. A., Senior, C. A., Stevens, B., Stouffer, R. J., and Taylor, K. E. (2016). Overview of the Coupled Model Intercomparison Project Phase 6 (CMIP6) experimental design and organization. *Geoscientific Model Development*, 9(5):1937–1958.

Harris, I., Osborn, T. J., Jones, P., and Lister, D. (2020). Version 4 of the CRU TS monthly high-resolution gridded multivariate climate dataset. *Scientific Data*, 7(1).

Hofmann, D. J., Butler, J. H., Dlugokencky, E. J., Elkins, J. W., Masarie, K., Montzka, S. A., and Tans, P. (2006). The role of carbon dioxide in climate forcing from 1979 to 2004: Introduction of the Annual Greenhouse Gas Index. In *Tellus, Series B: Chemical and Physical Meteorology*, volume 58, pages 614–619.

Leirvik, T. and Yuan, M. (2021). A Machine learning technique for spatial interpolation of solar radiation observations. *Earth and Space Science*, page e2020EA001527.

Phillips, P. C., Leirvik, T., and Storelvmo, T. (2020). Econometric estimates of Earth's transient climate sensitivity. *Journal of Econometrics*, 214(1):6–32.

Phillips, P. C. B. (1995). Fully Modified Least Squares and Vector Autoregression. *Econometrica*, 63(5):1023–78.

Phillips, P. C. B. and Hansen, B. E. (1990). Statistical Inference in Instrumental Variables Regression with I(1) Processes. *The Review of Economic Studies*, 57(1):99.

Storelvmo, T., Leirvik, T., Lohmann, U., Phillips, P. C. B., and Wild, M. (2016). Disentangling greenhouse warming and aerosol cooling to reveal Earth's climate sensitivity. *Nature Geoscience*, 9(4):286–289.

Sun, H., Gui, D., Yan, B., Liu, Y., Liao, W., Zhu, Y., Lu, C., and Zhao, N. (2016). Assessing the potential of random forest method for estimating solar radiation using air pollution index. *Energy Conversion and Management*, 119:121 – 129.

Wallace, C. J. J. and Joshi, M. (2018). Comparison of land-ocean warming ratios in updated observed records and CMIP5 climate models Comparison of land-ocean warming ratios in updated observed records and CMIP5 climate models. *Environmental Research Letters*, 13:114011.

Wild, M., Ohmura, A., and Makowski, K. (2007). Impact of global dimming and brightening on global warming. *Geophysical Research Letters*, 34(4).

Wild, M., Ohmura, A., Schär, C., Müller, G., Folini, D., Schwarz, M., Zyta Hakuba, M., and Sanchez-Lorenzo, A. (2017). The Global Energy Balance Archive (GEBA) version 2017: A database for worldwide measured surface energy fluxes. *Earth System Science Data*, 9(2):601–613.

Yuan, M., Leirvik, T., and Wild, M. (2021). Global trends in downward surface solar radiation from spatial interpolated ground observations during 1961-2019. *Under review.*

Zhou, Q., Flores, A., Glenn, N. F., Walters, R., and Han, B. (2017). A machine learning approach to estimation of downward solar radiation from satellite-derived data products: An application over a semi-arid ecosystem in the us. *PloS one*, 12(8):e0180239.

Utgitt i ph.d. serie ved Handelshøgskolen:

Nr. 1 – 2003	Lars Øystein Widding Bygging av kunnskapsreservoarer i teknologibaserte nyetableringer
Nr. 2 – 2005	Pawan Adhikari Government Accounting in Nepal: Tracing the Past and the Present
Nr. 3 – 2005	Tor Korneliussen The Relationship between Initation, Barriers, Product Quality and Internationalization
Nr. 4 – 2005	Bjørn Willy Åmo Employee innovation behavior
Nr. 5 – 2005	Odd Birger Hansen Regnskap og entreprenørskap. En fortolkende studie av hvordan to entreprenører bruker regnskap
Nr. 6 – 2006	Espen John Isaksen Early Business Performance - Initial factors effecting new business outcomes
Nr. 7 – 2006	Konstantin Timoshenko Russian Government Accounting: Changes at the Central level and at a University
Nr. 8 – 2006	Einar Rasmussen Facilitating university spin-off ventures -an entrepreneurship process perspective
Nr. 9 – 2007	Gry Agnete Alsos Portfolio Entrepreneurship - general and farm contexts
Nr. 10 – 2007	Elsa Solstad Tre sykehus - to verdener - en fusjon. En studie av reorganisering i et helseforetak
Nr. 11 – 2007	Levi Gårseth-Nesbakk Experimentation with accrual accounting at the central government level in Norway - how a global phenomenon becomes a local practice
Nr. 12 – 2007	Tatiana Iakovleva Factors Associated with new venture performance: The context of St. Petersburg

Nr. 13 – 2007	Einar Lier Madsen Utvikling av dynamiske kapabiliteter i små og mellomstore bedrifter
Nr. 14 – 2008	Anne Haugen Gausdal 'Network Reflection' – a road to regional learning, trust and innovation
Nr. 15 – 2008	Lars Rønning Social capital in farm-based entrepreneurship and rural development
Nr. 16 – 2008	Terje Andreas Mathisen Public Passenger Transport in Norway – Regulation, Operators' Cost Structure and Passengers' Travel Costs
Nr. 17 – 2008	Evgueni Vinogradov Immigrant Entrepreneurship in Norway
Nr. 18 – 2008	Elin Oftedal Legitimacy of Creative Destruction
Nr. 19 – 2009	Frode Kjærland Valuation of Generation Assets – a Real Option Approach
Nr. 20 – 2009	Tatiana Maximova-Mentzoni Marketization of the Russian University: Origins, Features and Outcomes
Nr. 21– 2009	Hugo Skålsvik Studies of Market led Processes influencing Service Performance: -Case Studies on the Norwegian Coastal Voyage
Nr. 22– 2009	Svein Oskar Lauvsnes Determinants of a shifting effective demand equilibrium. An explorative investigation of the interaction between psychological, financial and real factors
Nr. 23– 2010	Frode Fjelldal-Soelberg Entreprenøriell markedsføring. En studie av entreprenørskap og markedsføring som overlappende fenomen
Nr. 24– 2010	Heidi Rapp Nilsen From Weak to Strong Sustainable Development An analysis of Norwegian economic policy tools in mitigating climate change

Nr. 25– 2010	Gowindage Chamara Jayanath Kuruppu Development of Central Government Accounting in Sri Lanka: Three perspectives on the accounting changes
Nr. 26– 2010	Marina Z. Solesvik Interfirm collaboration: The context of shipbuilding.
Nr. 27– 2010	Jan Terje Henriksen Planning, Action and Outcome - Evaluation of the Norwegian Petroleum System: A Structuration Approach to Ripple Effect Studies
Nr. 28– 2010	May Kristin Vespestad Empowered by Natures – Nature-based High North Tourism Experiences in an International Context
Nr. 29– 2011	Andrei Mineev How has the petroleum supply industry developed in The Russian Barents Sea Region? Institutional and managerial aspects
Nr. 30– 2011	Jorunn Grande Entrepreneurship in small rural firms - the case of agriculture
Nr. 31– 2011	Thomas Johansen Paradigms in Environmental Management Research: Outline of an Ecosophical-Hermeneutic Alternative
Nr. 32– 2011	Elena Dybtsyna Accountant in Russia: changing times, changing roles.
Nr. 33– 2012	Harald Fardal Information Systems Strategy in Practice A Social Process Perspective
Nr. 34– 2012	Kristin Haugland Smith Hva er bedrifters samfunnsansvar? - En empirisk tilnærming av bedrifters ansvar overfor samfunnet
Nr. 35– 2012	Are Branstad The management of entrepreneurship support – Organisation and learning in corporate incubation, technology transfer and venture capital
Nr. 36– 2012	Victoria Konovalenko A “coordination kaleidoscope”: The role of a “Corporate University” as a coordinator of knowledge flows in a Russian transnational corporation

Nr. 37– 2012	Thor-Erik Sandberg Hanssen Essays in Transport Economics with application to Transport Policy
Nr. 38– 2013	Are Severin Ingulfsvann Verdiforskyvning i friluftslivet i lys av økologisk økonomi
Nr. 39– 2013	Natalia Andreassen Sustainability Reporting in a Large Russian Oil Corporation. Production Safety Issues
Nr. 40– 2013	Elena Panteleeva Contemporary Management Accounting Practices in Russia: The Case of a Subsidiary in a Russian Oil Company
Nr. 41– 2013	Thusitha S.L.W.Gunawardana Impact of Power Sources on Channel Members' Performance
Nr. 42– 2013	Nadezda Nazarova Mastering Nature and Managing Frictions: Institutional Work and Supply Chain Management in the High North
Nr. 43– 2013	Inge Hermanrud Managed Networks of Competence in Distributed Organizations - The role of ICT and Identity Construction in Knowledge Sharing
Nr. 44– 2013	Kari Djupdal Sustainable entrepreneurship: outcomes associated with an environmental certification resource
Nr. 45– 2013	Imtiaz Badshah Federal government accounting in The Islamic Republic of Pakistan
Nr. 46– 2014	Muhammad Arif Inter-organizational Exchange Relationships – Exchange Relationships between Local Service Suppliers and Tour Operators in the Tourism Distribution Channel
Nr. 47– 2014	Wondwesen Tafesse The Marketing Functions of the Trade Show System
Nr. 48– 2014	Fritz J. Nilssen Erfaringsutveksling som grunnlag for mestring og livskvalitet Diagnoseoverskridende samtalegrupper for familier med barn som har nedsatt funksjonsevne og eller kronisk sykdom.

Nr. 49– 2014	Ingebjørg Vestrum The Resource Mobilisation Process of Community Ventures -The Case of Cultural Events in Rural Communities
Nr. 50– 2014	Ragnhild Johnson The Practice of Project Management - A qualitative analysis of complex project-based organizations
Nr. 51– 2014	Ann Heidi Hansen Memorable moments Consumer immersion in nature-based tourist experiences
Nr. 52– 2014	June Borge Doornich Entry modes and organizational learning during internationalization An analysis of Norwegian supply companies’ entering and expanding in the Russian oil and gas sector
Nr. 53– 2014	Kjersti Karijord Smørvik Opplevelsesskaping i dynamiske opplevelsesrom: En studie av turisters opplevelser på Hurtigruten
Nr. 54– 2015	Marianne Terese Steinmo How Firms use University-Industry Collaboration to Innovate: The role and Development of Social Capital and Proximity Dimensions
Nr. 55– 2015	Eva J.B. Jørgensen Border Firms: Norway and Russia
Nr. 56– 2015	Krister Salamonsen Exogenous Shocks as Drivers of Growth in Peripheral Regions. - A Multilevel Approach to Regional Development
Nr. 57– 2015	Hindertje Hoarau Heemstra Practicing open innovation in experience-based tourism: the roles of knowledge, values and reflexivity
Nr. 58– 2015	Elena Zhurova Environmental Performance Reporting of Russian Oil and Gas Companies
Nr. 59– 2016	Siri Jakobsen Environmental innovation cooperation: The development of cooperative relationships between Norwegian firms
Nr. 60– 2016	Antonina Tsvetkova Supply Chain Management in the Russian Arctic: An institutional perspective

Nr. 61– 2017	Kjersti Granås Bardal Impact of Adverse Weather on Road Transport: Implications for Cost-Benefit Analysis
Nr. 62– 2017	Kristian Støre Methodological contributions and applications in real options analysis
Nr. 63– 2017	Thomas André Lauvås The dynamics of university-industry collaboration: A longitudinal case study of research centers
Nr. 64– 2017	Sølvi Solvoll Development of effectual and casual behaviors: Exploring new venture creation in the tourism industry
Nr. 65– 2017	Evgenii Aleksandrov The changing role of accounting from reformees' perspective: A study of public sector reforms in Russia
Nr. 66– 2017	Igor Khodachek Budget, Strategy and Accounting. Managing institutional change in Russia's governments
Nr. 67– 2018	Vivi Marie Lademoe Storsletten Quality as flourishing A study of quality based upon leadership in kindergartens with implications for Ecological Economics
Nr. 68– 2018	Olga Iermolenko The human side of accounting: The bonds between human agency and management accounting practices' changes in the transitional economy
Nr. 69– 2018	Karin Wigger Mobilization of Collective Resources for Entrepreneurship: Case Studies in Nordic Peripheries
Nr. 70 – 2018	Andreas Mikkelsen Trading fast and slow: algorithmic trading in the Nordic region
Nr. 71 – 2018	Asbjørn Veidal Strategic entrepreneurship in farm businesses
Nr. 72 – 2018	Are Jensen Early imprints in and on new technology-based firms

Nr. 73 – 2018	Marianne Arntzen-Nordqvist The financing process of new technology-based firms - The entrepreneur’s perspective
Nr. 74 – 2019	Irina Nikolskaja Roddvik Deprivation of control: A driving force to gain influence during the internationalization process of MNC
Nr. 75 – 2019	Petter Gullmark Unraveling the Building Blocks of Local Government Organizations’ Innovativeness: Insights from a Dynamic Capabilities Perspective
Nr. 76 – 2019	Hanne Stokvik Knowledge for Innovation
Nr. 77 – 2019	Anastasiya Henk Between the Devil and the Deep Blue Sea: Managing Business Processes in Turbulent Environments
Nr. 78 – 2019	Tadeu Fernando Nogueira Entrepreneurial Learning: An Exploration of the Learning of New Venture Founders
Nr. 79 – 2020	Veronika Vakulenko Public Sector Reforms in Ukraine: Roles Played by Global and Local Agents in Implementing Converging and Diverging Changes
Nr. 80 – 2020	Lars Hovdan Molden Adapting to Change - On the Mechanisms of Dynamic Capabilities
Nr. 81 – 2020	Sudip Kranti Tiwari Navigating International Entrepreneurship in a Developing Economy Context: Lessons from Nepal
Nr. 82 – 2020	Vu Le Tran Expected Returns: An Empirical Asset Pricing Study
Nr. 83 – 2020	Marit Breivik-Meyer It takes two to tango: The role of incubators in the early development of start-ups
Nr. 84 – 2021	Per Ivar Seljeseth Assessing Outcomes from Business-to-Business Selling
Nr. 85 – 2021	Amsale Kassahun Temesgen Human Wellbeing and Local-level Sustainability

Nr. 86 – 2021	Ensieh Roud The Role of Joint Training in Inter-organizational Collaboration in Emergency Management
Nr. 87 – 2021	Menghan Yuan Climate Change and Economic Growth: An Empirical Study of Economic Impacts of Climate Change

Global warming and the increasing incidence of extreme weather events are disrupting economies and affecting human lives over the world. This thesis intends to constrain the uncertainty of climate sensitivity and to investigate the economic impacts of climate change. This thesis consists of four papers.

The first two papers aim to address the uncertainty of the climate sensitivity. The authors applied an empirical estimation framework which relates temperature to solar radiation and CO_2 in a cointegrating equilibrium relationship. In order to facilitate the empirical estimation, the first paper constructs a global dataset of surface solar radiation with complete global land surface coverage during the period 1961-2019, which provides the input data for the climate sensitivity estimation conducted in the second paper. The second paper empirically estimates Transient Climate Sensitivity (TCS) for 22 global climate models and significantly narrows the confidence interval of TCS compared to previous estimates.

The last two papers use panel data analyses to examine how agriculture and aggregated economies are influenced by climate change, respectively. Based on an extensive dataset covering worldwide countries over more than five decades, the agricultural paper contributes to investigate the heterogeneity effects in various regions and in rich/poor countries. The last paper investigates the possibility of using a novel panel data approach—interactive fixed effects model, to allow for the heterogeneous effects of countries affected by the common global shocks.

NORD
University

ISBN: 978-82-92893-77-7
ISSN 2464-4331
Trykk: Trykkeriet, Nord universitet
www.nord.no